SOLIDIFICATION BEHAVIORS OF PROEUTECTIC AL3SC AND AL-AL3SC EUTECTIC IN HYPEREUTECTIC AL-SC UNDERCOOLED MELT

by

Aoke Jiang

A Dissertation

Submitted to the Faculty of Purdue University

In Partial Fulfillment of the Requirements for the degree of

Doctor of Philosophy

Department of Engineering Technology

West Lafayette, Indiana

May 2021

THE PURDUE UNIVERSITY GRADUATE SCHOOL
STATEMENT OF COMMITTEE APPROVAL

Dr. Xiaoming Wang, Chair

Department of Engineering Technology

Dr. Suranjan Panigrahi

Department of Engineering Technology

Dr. Milan Rakita

Department of Engineering Technology

Dr. Changhua Huang

Ryobi Die Casting

Approved by:

Dr. Kathryne Newton

To my family

ACKNOWLEDGMENTS

I am deeply grateful to my major professor and chair, Dr. Xiaoming Wang, who recruited me in the group, introduced me to my current research direction, customized plans for a research novice (me) to grow, gave me insightful advice, warned me when I was off the right track, and clapped for us students when we made every little progress. With Dr. Wang's guidance and support, I was able to finish the dissertation and go through the doctoral program.

My sincere thanks also go to other committee members, Dr. Suranjan Panigrahi, Dr. Milan Rakita, and Dr. Changhua Huang. Because of their invaluable suggestions, advice, and support, I could go along this path firmly.

I would also like to thank another Dr. Wang's group member, Dr. Siming Ma. It was so fortunate to collaborate with him, and learn a lot from him. To me, he acts as a role model of our generation, constantly reminding me that someone better than you never stops moving.

Furthermore, I would like to thank many prominent scientists, researchers, and authors that I have ever met in the literature, because they had a great impact on my research methodology and writing style, even though I did not have a chance to meet them face-to-face. These respected scholars include Wilfried Kurz, Rohit K. Trivedi, Martin E. Glicksman, Kenneth A. Jackson, Dieter M. Herlach, …

In addition, I owe School of Engineering Technology a debt of gratitude for offering me a TA position over the past four years in support of my doctoral study.

TABLE OF CONTENTS

LIST OF TABLES

LIST OF FIGURES

LISTS OF ABBREVIATIONS AND SYMBOLS

ABBREVIATIONS	TERMS
2-D	Two-dimensional
3-D	Three-dimensional
BSE	Back-scattered electron
CD	Compact dendrites
CS	Compact seaweeds
EDX	Energy dispersive X-ray
FCC	Face-centered cubic
FD	Fractal dendrites
FIB	Focused ion beam
FS	Fractal seaweeds
HAADF	High-angle annular dark field
IMC	Intermetallic compound
MSC	Marginal stability criterion
OM	Optical microscopy
SAD	Selected area diffraction
SE	Secondary electron
SEM	Scanning electron microscopy
S/L	Solid/liquid
TEM	Transmission electron microscopy
TM	Transition metal

SYMBOLS	MEANINGS
A	Area
C	Constant
D	Solute diffusivity
D_{th}	Thermal diffusivity
E_1	Exponential integral function
G_c	Concentration gradient
G_l	Temperature gradient in liquid
G_s	Temperature gradient in solid
K_1	Material property constant
K_2	Material property constant
L	Latent heat
M	Solute mobility
N	Number of boxes in the box counting method
N	Mole number of specimen
P_t	Thermal Peclet number
R	Radius of spherical solid
R	Gas constant
R_c	Critical radius for interface instability
S	Scale down factor
T	Temperature
$\dot{T}$	Cooling rate
T_0	Room temperature
T_m	Melting point
V	Growth rate
V_D	Diffusive velocity
Z	Number of nearest-neighbor bonds
a	Thermal diffusion coefficient
a_0	Interatomic distance
c	Composition

c_∞	Melt composition far away from interface
c_l^*	Liquid composition at the interface
c_l^{eq}	Equilibrium liquid composition
c_p	Specific heat
d	Distance from the dendrite tip
d	Orientation-dependent capillarity length
d'	Rescaled capillarity length
d_0	Isotropic portion of capillarity length
d_f	Fractal dimension
f	Volume fraction
h	Half width of dendrite
h_0	Heat transfer coefficient
j	Number of symmetry
k	Partition coefficient
k_B	Boltzmann constant
l_c	Solute diffusion length
l_{th}	Thermal diffusion length
m	Liquidus slope
m_{eff}	Effective liquidus slope
n	Number of rods
n_1	Number of nearest-neighbor bonds parallel to the growing crystalline plane
p_e	Eutectic Peclet number
q	Heat flux
t	Time
z	Thickness of the wedge casting
α	Jackson alpha factor
β	Orientation-dependent kinetic coefficient
β'	Rescaled kinetic coefficient
ΔC	Composition difference at solid/liquid interface

ΔG	Relative molar free energy of an interface that maintains a certain roughness
$\overline{\Delta T}$	Dimensionless melt undercooling
ΔT_c	Constitutional undercooling
ΔT_k	Kinetic undercooling
ΔT_R	Undercooling caused by the forced alteration of interface's roughness
ΔT_r	Curvature undercooling
ΔT_t	Thermal undercooling
$\overline{\Delta T_k}$	Dimensionless kinetic undercooling
$\overline{\Delta T_r}$	Dimensionless curvature undercooling
$\overline{\Delta T_s}$	Dimensionless constitutional undercooling
$\overline{\Delta T_t}$	Dimensionless thermal undercooling
ΔS_f	Entropy of fusion
Γ	Gibbs-Thomson coefficient
γ	Mean interface tension
$\tilde{\gamma}$	Surface stiffness
ϵ	Strength of anisotropy
θ	Angle between the interface normal and a given direction
θ	Ratio of the number of occupied sites to the maximum number of growth sites for adding new atoms
θ_d	Offset angle for surface tension
θ_β	Offset angle for kinetic coefficient
κ	Interface curvature
κ	Thermal conductivity
λ	Eutectic spacing
λ	Spacing between two neighboring branches
λ_{ex}	Eutectic spacing at extremum condition
μ	Chemical potential
μ	Kinetic coefficient
μ^{eq}	Equilibrium chemical potential

μ_l^*	Chemical potential of the liquid at the interface
ξ_c	Solute stability function
ρ	Radius of dendrite tip
σ^*	Stability constant
ϕ	Correction factor for eutectic spacing in irregular eutectics

ABSTRACT

The lack of a thorough understanding of the solidification behaviors of the proeutectic Al_3Sc and the Al-Al_3Sc eutectic in a hypereutectic Al-Sc alloy stimulates the present dissertation. The major findings for the single-phase growth of the proeutectic Al_3Sc is summarized as follows: At a low cooling rate (~1 ºC·s^{-1}), the proeutectic Al_3Sc phase's formation was governed by the lateral growth, exposing six flat {100} facets. At an intermediate cooling rate (~400 ºC·s^{-1}), the proeutectic Al_3Sc grew in a dendritic manner, with well-defined backbones extending in eight <111> directions and paraboloidal dendrite tips, although the dendrite tips and side-branches turned into faceted steps at a late growth stage, when the lateral growth prevailed. At a high cooling rate (~1000 ºC·s^{-1}), the proeutectic Al_3Sc primarily crystallized into an entirely seaweed-structured particle, which was composed of interior compact seaweeds and exterior fractal seaweeds. In order to verify the proposed dendritic and seaweed growth mechanisms for the proeutectic Al_3Sc, various morphological stability criteria were used, and fair agreement between the observed and the estimated characteristic length scales was reached.

On the Al-Al_3Sc eutectic side, it was found that a rod-typed Al_3Sc eutectic phase prevalently existed in an as-cast hypereutectic Al-Sc alloy that solidified via both slow cooling in air (~1 ºC·s^{-1}) and rapid cooling in a wedge-shaped copper mold (up to ~3000 ºC·s^{-1}). Al-Al_3Sc eutectic dendrites were identified within a narrow region near the edge of the wedge. The eutectic dendrites had an equiaxed dendritic contour and a rod eutectic structure inside. Quantitative assessments revealed that an interface undercooling of 48.2 ºC was required to form the eutectic dendrites, or in other words, to enter the coupled zone of the Al-Al_3Sc phase diagram. Furthermore, a phenomenon of scientific interest was discussed: When crystallizing under a near-equilibrium condition, the eutectic Al_3Sc phase formed a non-faceted morphology, in contradiction to its faceted nature. Based on the competitive growth criterion, it was deduced that the non-faceting of the eutectic Al_3Sc phase essentially reduced the interface undercooling for the resultant regular eutectic, in comparison to an otherwise irregular eutectic that would contain a faceted eutectic Al_3Sc phase.

CHAPTER 1. INTRODUCTION

1.1 Background

Scandium (Sc) may serve as an effective microalloying element strengthener for commercial aluminum (Al) alloys in the future, once the issues, such as scarcity and uncertainty of long-term supply, are addressed (Dorin et al., 2018). So far, on the laboratory scale, the addition of Sc has experimentally been demonstrated to reinforce Al alloys via strengthening mechanisms not restricted to solid solution strengthening, precipitation hardening, inhibiting recrystallization, assisting nucleation of strengthening phases, and grain refinement. (Dorin et al., 2018). In particular, an intermetallic compound phase, Al_3Sc, plays the central role in the grain refinement of Al, if Al_3Sc can be generated prior to Al in the processes involving solidification, e.g., casting, welding, and additive manufacturing. One important research topic in this setting is the solidification behaviors of the proeutectic Al_3Sc phase in the Al-Al_3Sc eutectic system. In addition, a eutectic reaction follows the formation of proeutectic Al_3Sc. The characteristics of the Al-Al_3Sc eutectic should also influence the mechanical properties of the grains, and thus, the as-processed product, necessitating the study of the solidification behaviors of Al-Al_3Sc eutectic. Moreover, the incorporation of the cooling condition as a variable to the study would allow the investigated topics to have a broader application range. Thus, the present dissertation aimed to study the solidification behaviors of both the proeutectic Al_3Sc and the Al-Al_3Sc eutectic under different cooling conditions.

1.2 Problem and purpose

Although Al_3Sc plays a key role in hypereutectic Al-Sc alloys, only a few accessible studies in the literature have looked into the solidification behaviors of proeutectic Al_3Sc. Despite some progress made, there is still a lot remaining unclear. Likewise, the solidification behaviors of Al-Al_3Sc eutectic is also uncertain. To the best knowledge of the author, no accessible studies had investigated the eutectic growth of Al-Al_3Sc in-depth. The purpose of the present study was to clarify the less understood solidification behaviors of the proeutectic Al_3Sc and the Al-Al_3Sc eutectic under different cooling conditions.

1.3 Research questions

The principle research questions to be answered included:

1) How did the proeutectic Al_3Sc phase respond to different cooling rates when crystallizing in a hypereutectic Al-2 wt. % Sc melt?

2) Following question #1, how did each form of the proeutectic Al_3Sc phase develop at a specific cooling rate?

3) How did the Al-Al_3Sc eutectic respond to different cooling rates when crystallizing in a hypereutectic Al-2 wt. % Sc melt?

4) Following question #3, how did each form of the Al-Al_3Sc eutectic develop at a specific cooling rate?

5) Were there any notable phenomena, which were of scientific significance and shed light on a broad context of crystal growth, in the solidification of a hypereutectic Al-2 wt. % Sc alloy?

1.4 Definitions of some key terminologies

Some key concepts and terminologies are listed below in alphabetical order:

Coupled zone – "the growth temperature/composition region where the eutectic grows more rapidly (or at a lower undercooling) than do dendrites … corresponding to an entirely eutectic microstructure" (Kurz & Fisher, 1998, p. 109).

Dendrites – "tree-like crystalline objects, more formally described as fine, ramified, single crystals that grow by diffusion-limited heat and mass transfer. Dendrites typically exhibit morphological features that include constrained directionality, i.e., crystallographically-related, straight primary stems, which periodically branch laterally into secondary 'side arms'" (Glicksman, 2015, p. 670).

Eutectic dendrites – Eutectic dendrites could form in an undercooled eutectic melt, in which the thermal diffusion is solely responsible for generating the dendritic contour of a eutectic colony, whereas the solute diffusion alone governs the eutectic growth on a much finer scale with respect to the scale of the eutectic colony (Li & Zhou, 2005).

Kinetic roughening – "a transition in the diffusiveness, or width, of the solid-liquid zone … induces microscopic changes in the interface that are expected to be atomically smooth at low

speeds and driving force, to ones that act as atomically rough interfaces at high speeds and larger driving force" (Glicksman, 2011, p. 390).

Rapid solidification – a solidification process, wherein either a high cooling rate or a large undercooling is used to "produce high rates of advance of the solidification front (typically V > 1cm/s)" (Kurz & Fisher, 1998, p.133).

Recalescence – a phenomenon, in which during solidification, heating occurs when the rate of heat extraction by environment is lower than the rate of latent heat release (Kurz & Fisher, 1998).

Seaweed structure – "loosely used in the literature to describe a variety of branching morphology with various levels of deviation from regular dendrites" (Assadi et al., 2009, p. 1639).

Undercooled melt – the melt with a temperature below the melting temperature or the liquidus temperature.

Undercooling – "the temperature difference between the equilibrium temperature of a system and its actual temperature" (Kurz & Fisher, 1998, p. 22), also known as *supercooling*.

1.5 Assumptions

The assumptions of the present study were as follows:

1) All preexisting Al_3Sc in the as-received alloy was completely melted during remelting process.

2) Al_3Sc was the only intermetallic compound that could be produced in the Al-Al_3Sc system (up to 35.37 wt. % Sc). No any metastable compound phase is known to date, so no any metastable compound phase was assumed to coexist with Al_3Sc, or even replace Al_3Sc at any investigated cooling condition.

1.6 Delimitations

The delimitations of the present study were as follows:

1) Although the proeutectic Al_3Sc phase is known to be an effective grain refiner for cast Al-based alloys (Norman et al, 1998), the efficiency of grain refinement by Al_3Sc was not investigated.

2) Mechanical properties, such as strength, hardness, and ductility, of different structures in the studied samples were not measured nor analyzed.

3) Although precipitation strengthening is one of major strengthening mechanisms in the Al-Al_3Sc system (Marquis & Seidman, 2001), the precipitation of Al_3Sc in the post-solidification heat treatment was not studied.

4) Only was a binary Al-Sc alloy with a composition of Al-2 wt. % Sc studied in the dissertation. Ternary or higher-order multi-component Al-Sc-X-… alloys were not considered, even though they attracted extensive attention in the literature (Popova et al., 2017; Zhou et al., 2016).

1.7 Limitations

The limitations of the present study were as follows:

1) The solidification methods used in the dissertation allowed for unconstrained growth of crystals. Unlike the constrained growth, e.g., Bridgman growth, the interface undercooling of the growing crystal was practically impossible to be directly measured in the unconstrained growth. Besides, without the aid of in-situ observation techniques, such as high-energy X-ray diffraction (Zhou et al., 2019) and synchrotron X-ray microtomography (Terzi et al., 2010), the advancing velocity of the solid/liquid interface was not directly measurable in the opaque alloy melt.

2) The lack of available data for relevant thermo-physical parameters in the literature led to the inevitable use of rough estimates, such as the Gibbs-Thomson coefficients of α-Al and Al_3Sc in the alloy melt, the diffusion coefficient of Sc in liquid Al, and kinetic coefficients for α-Al and Al_3Sc.

3) The spatial resolution limit of energy dispersive X-ray (EDX) analysis in scanning electron microscope (SEM) was encountered in the present study, which is usually on the order of 1 μm (Neikov & Yefimov, 2019). Namely, the microstructure finer than ~1 μm was not resolvable to SEM-EDX analysis. The situation was even worse when two-dimensional scanning strategy was used.

1.8 References

Assadi, H., Oghabi, M., & Herlach, D. (2009). Influence of ordering kinetics on dendritic growth morphology. *Acta Materialia, 57*(5), 1639-1647. https://doi.org/10.1016/j.actamat.2008.12.004

Dorin, T., Ramajayam, M., Vahid, A., & Langan, T. (2018). Aluminium scandium alloys. In: R. Lumley (Ed.), *Fundamentals of Aluminium Metallurgy: Recent Advances* (pp. 439-494). Woodhead Publishing. https://doi.org/10.1016/B978-0-08-102063-0.00012-6

Glicksman, M. E. (2011). *Principles of solidification: An introduction to modern casting and crystal growth concepts*. Springer, New York. https://doi.org/10.1007/978-1-4419-7344-3

Glicksman, M. E. (2015). 16 – Dendritic growth. In: T. Nishinaga (Ed.), *Handbook of Crystal Growth: Fundamentals* (2nd ed., pp. 669–722). Elsevier Inc. https://doi.org/10.1016/B978-0-444-56369-9.00016-2

Li, J. F., & Zhou, Y. H. (2005). Eutectic growth in bulk undercooled melts. *Acta Materialia, 53*(8), 2351-2359. https://doi.org/10.1016/j.actamat.2005.01.042

Marquis, E. A., & Seidman, D. N. (2001). Nanoscale structural evolution of Al3Sc precipitates in Al(Sc) alloys. *Acta Materialia, 49*(11), 1909-1919. https://doi.org/10.1016/S1359-6454(01)00116-1

Neikov, O. D., & Yefimov, N. A. (2019). Chapter 1 - Powder Characterization and Testing. In O. D. Neikov (Ed.), *Handbook of Non-Ferrous Metal Powders: Technologies and Applications* (2nd ed., pp. 3-62). Elsevier. https://doi.org/10.1016/B978-0-08-100543-9.00001-4

Norman, A. F., Prangnell, P. B., & McEwen, R. S. (1998). The solidification behaviour of dilute aluminium–scandium alloys. *Acta Materialia, 46*(16), 5715-5732. https://doi.org/10.1016/S1359-6454(98)00257-2

Popova, E. A., Kotenkov, P. V., Shubin, A. B., & Pastukhov, E. A. (2017). Structural Features of Al–Hf–Sc Master Alloys. *Russian Journal of Non-ferrous Metals, 58*(6), 639-643. https://doi.org/10.3103/S1067821217060086

Terzi, S., Taylor, J. A., Cho, Y. H., Salvo, L., Suéry, M., Boller, E., & Dahle, A. K. (2010). In situ study of nucleation and growth of the irregular α-Al/β-Al5FeSi eutectic by 3-D synchrotron X-ray microtomography. *Acta Materialia, 58*(16), 5370-5380. https://doi.org/10.1016/j.actamat.2010.06.012

Zhou, L., Meng, F., Zhou, S., Sun, K., Kim, T., Ott, R., Napolitano, R., & Kramer, M. J. (2019). An abnormal meta-stable nanoscale eutectic reaction revealed by in-situ observations. *Acta Materialia*, 164, 697-703. https://doi.org/10.1016/j.actamat.2018.11.027

Zhou, S., Zhang, Z., Li, M., Pan, D., Su, H., Du, X., Li, P., & Wu, Y. (2016). Correlative characterization of primary particles formed in as-cast Al-Mg alloy containing a high level of Sc. *Materials Characterization*, *118*, 85-91. https://doi.org/10.1016/j.matchar.2016.05.011

CHAPTER 2. REVIEW OF LITERATURE

2.1 Background of lightly scandium-alloyed aluminum

As a microalloying element to Al alloys, the addition of Sc in Al alloys seldom exceeds 2.0 weight percent. This practice is due to the limited market availability and the high cost of Sc (Riva et al., 2016), the latter reaching 5100 U.S. dollars per kilogram for 99.99 % pure scandium oxide, according to 2015 data (Czerwinski, 2019). A very recent Al-Sc phase diagram (Dorin et al., 2018) is displayed in figure 5.1a. Up to 35.7 wt. % Sc, Al_3Sc is the only intermetallic compound involved in the Al-Sc alloy system. To date, no metastable intermetallic compounds that could compete with or replace Al_3Sc under non-equilibrium conditions have been reported.

2.2 The role of Al_3Sc in Al-Sc alloys

Al_3Sc is a stoichiometric intermetallic compound, located at 35.7 wt. % Sc. Al_3Sc has the same crystalline structure ($L1_2$ structure) with Cu_3Au, Ni_3Al, and Ni_3Fe, which can be described as an ordered face-centered cubic (FCC) structure, with Al atoms occupying the six face centers and Sc atoms positioning at the eight vertices (Røyset & Ryum, 2005), as shown in figure 2.1. The lattice constant of Al_3Sc is 0.4105 nm, merely ~1.5 % larger than that of α-Al (Blake & Hopkins, 1985). In addition, the similarities in the lattice structure of Al_3Sc and α-Al further favor the coherency between them. Another merit of Al_3Sc is the low density, which is only 3.03 $g \cdot cm^{-3}$ (Røyset & Ryum, 2005). Combined with the excellent thermal stability (Al_3Sc starts to melt peritectically at 1320 ºC; Shubin et al, 2008), Al_3Sc can be a promising lightweight high-temperature material candidate.

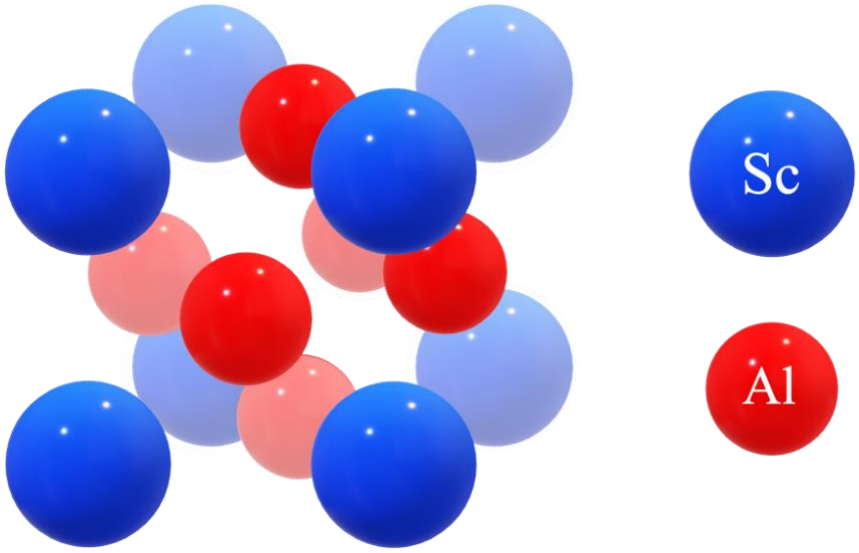

Figure 2.1 The lattice structure of $L1_2$-Al_3Sc.

The Sc-containing Al alloys benefit from the presence of Al_3Sc in several aspects. One of extensively studied area is the precipitation strengthening. The precipitation strengthening efficiency of Sc is higher than any other alloying element of the same amount of addition (Czerwinski, 2019; Marquis & Seidman, 2001). Roughly speaking, every 0.1 wt. % Sc addition can increase the yield strength of Al alloys by 50 MPa (Dorin et al., 2018). The improved strength is achieved by the precipitation of elastically hard and coherent nano-scaled Al_3Sc dispersoids, which can maintain the coherent relationship with α-Al matrix up to 20-30 nm in size (Marquis & Seidman, 2001). Furthermore, an attendant benefit of these Al_3Sc dispersoids is that they are capable of exerting a strong Zener drag on moving dislocations and grain boundaries, therefore, delaying recovery and recrystallization (Czerwinski, 2019; Dorin et al., 2018; Marquis & Seidman, 2001).

Another active field in which Al_3Sc plays a huge role is the grain refinement for as-cast or as-weld Al alloys. A prerequisite for Al_3Sc being an effective grain refiner for Al alloys is the alloy composition being hypereutectic, so that Al_3Sc could crystallize first from the melt as a proeutectic phase, and afterwards, act as a nuclei to effectively facilitates the heterogeneous nucleation of α-Al, thanks to the similarities in their lattice structures and lattice constants. This point has broadly been confirmed by experiments, not only for binary Al-Sc alloys (Costa et al., 2012; Hyde et al., 2001; Norman et al., 1998; Zhang et al., 2013), but also for higher-order multi-component Al-Sc-X-… alloys (Norman et al., 1998, 2003; Novikov & Grushko, 1995; Zhou et

al., 2016). In fact, when acting as a grain refiner, Al_3Sc has some advantages over other candidates. For instance, Hyde et al. (2001) suggested that the size of Al_3Sc is generally finer when generated in as-cast Al alloys compared to Ti/Ti_2B, and also, the former disperses into the matrix more homogeneously than does the latter. Additionally, in comparison to Ti/Ti_2B, Al_3Sc does not suffer from fading away, and has a higher grain refinement potency (Hyde et al., 2001). Furthermore, some other transition metal trialuminides can also serve as effective grain refiners, such as Al_3Ti (Chu, 1994), Al_3Zr (Nes & Billdal, 1977), and Al_3Hf (Norman & Tsakiropoulos, 1991b), once they form a metastable phase with an $L1_2$ structure. However, their stable phases with a $D0_{22}$ or $D0_{23}$ structure have a small effect on grain refinement, probably due to the fact that only a portion of crystalline planes in $D0_{22}$ and $D0_{23}$ structures resemble {100} planes of α-Al (Popova et al., 2020). This is to say, unlike Al_3Ti, Al_3Zr, and Al_3Hf, which require a careful control of solidification condition to form metastable phases, the effective grain refiner Al_3Sc can be generated under a wide range of conditions, since Al_3Sc is the only intermetallic compound in the Al-Al_3Sc system.

2.3 Previous investigations into the solidification behavior of the proeutectic Al_3Sc

Only have a few accessible studies looked into the solidification behavior of proeutectic Al_3Sc. In general, when cooled very slowly, the proeutectic Al_3Sc could form a cluster of cubes enclosed by {100} facets, which radiate from a center (Blake & Hopkins, 1985), see figure 2.2a and 2.2b. At a slow cooling rate of ~1 $^{o}C \cdot s^{-1}$, Al_3Sc cubes could disperse separately (Hyde et al., 2001). Figure 2.2c shows such an individual cubic Al_3Sc particle extracted by deep etching. At a high cooling of ~1000 $^{o}C \cdot s^{-1}$, the proeutectic Al_3Sc has a distinct morphology. Hyde et al. (2001) reported that a duplex structure was produced under this condition, in which a solid cubic core resided in the center, whereas fine cellular-dendritic structures decorated the outside, see figure 2.2d.

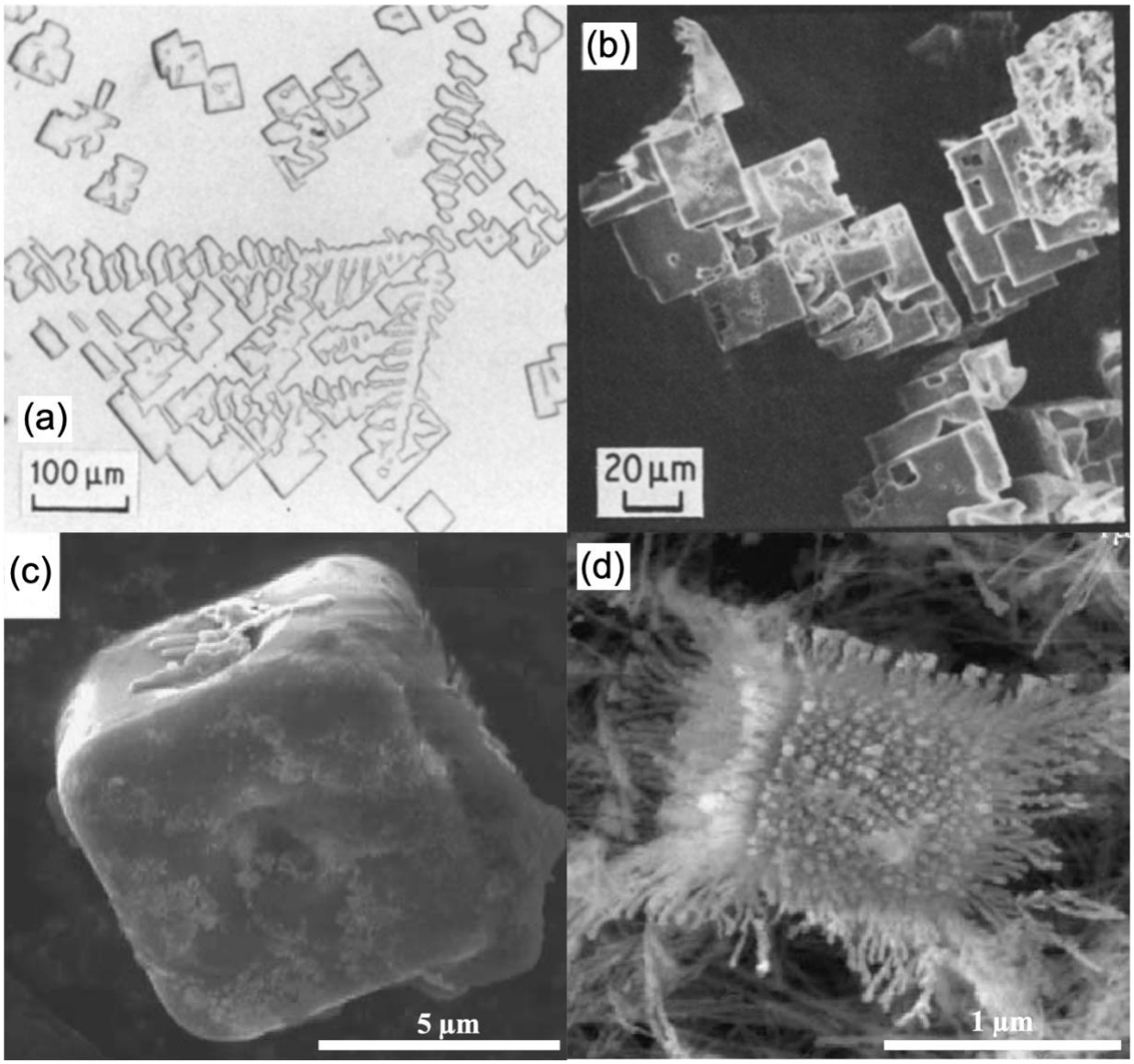

Figure 2.2 The morphology of the proeutectic Al_3Sc under different cooling conditions. The cluster of Al_3Sc cubes radiating from a center, which was produced at a very slow cooling rate, is revealed by (a) a cross-sectional view, and the three-dimensional (3-D) structure is disclosed by (b). (a,b) reproduced from "Constitution and age hardening of Al-Sc alloys," by N. Blake and M. A. Hopkins, 1985, *Journal of Materials Science*, *20*(8), p. 2862 (https://doi.org/10.1007/BF00553049). Copyright 1985 by Springer Nature Switzerland AG. Reprinted with permission. (c) Crystallized at ~1 $^{o}C \cdot s^{-1}$, the proeutectic Al_3Sc could form a separate cubic form. (d) Under ~1000 $^{o}C \cdot s^{-1}$, the proeutectic Al_3Sc could form a duplex structure. (c,d) reproduced from "The effect of cooling rate on the morphology of primary Al3Sc intermetallic particles in Al-Sc alloys" by K. B. Hyde, A. F. Norman, and P. B. Prangnell, 2001, *Acta Materialia*, *49*(8), pp. 1331 & 1333 (https://doi.org/10.1016/S1359-6454(01)00050-7). Copyright 2001 by Acta Materialia Inc. Reprinted with permission.

The {100} facets exposed in the slowly cooled proeutectic Al_3Sc were believed to indicate a highly faceted growth manner for Al_3Sc, and also, {100} facets being the slowest growing crystalline planes (Blake & Hopkins, 1985; Hyde et al., 2001). On the other hand, Hyde et al. (2001) explained the formation of the duplex-structured Al_3Sc particle as follows: At the beginning, an inner cubic core formed. Later on, the interfacial instabilities caused by the fast cooling condition was first initiated at the cube corners. The protrusions at the corners kept advancing along <111> direction, and eventually formed the primary dendrite trunks, which were followed by <110> secondary and <100> tertiary dendrite side branches.

Figure 2.3 Two examples of the duplex structure in metastable $L1_2$-structured (a) Al_3Hf and (b) Al_3Zr. (a) reproduced from "The microstructure and properties of rapidly solidified Al-Hf alloys," by A. F. Norman & P. Tsakiropoulos, 1991, *Materials Science & Engineering A*, *134*, p. 1235 (https://doi.org/10.1016/0921-5093(91)90963-N). Copyright 1991 by Elsevier B.V. Reprinted with permission. (b) reproduced from "Non-equilibrium solidification of hyperperitetic Al-Zr alloys," by E. Nes & H. Billdal, 1977, *Acta Metallurgica*, *25*(9), p. 1033 (https://doi.org/10.1016/0001-6160(77)90132-8). Copyright 1977 by Elsevier Ltd. Reprinted with permission.

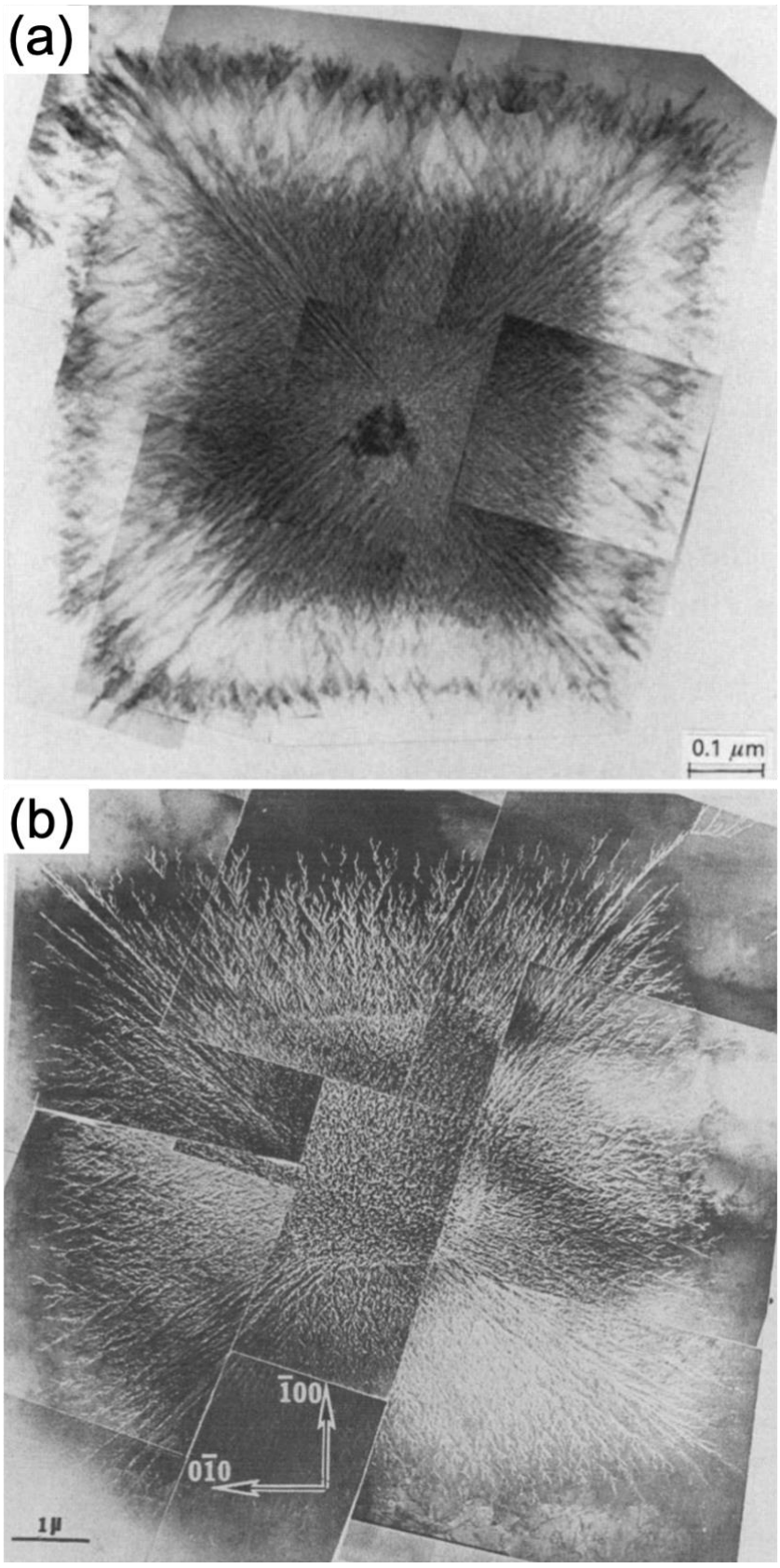
(a)
0.1 μm
(b)
$\bar{1}00$
$0\bar{1}0$
1μ

The aforementioned duplex structure is not unique for Al_3Sc. In fact, it has frequently been seen in rapidly solidified metastable $L1_2$-structured Al_3TM (TM=Hf, Ti, and Zr), and been termed "sponge particles" (Haugan et al., 1983), "petal-like crystals" (Norman & Tsakiropoulos, 1991b), and "flower crystals" (Khvan et al., 2018) in the literature. It is natural to postulate that the duplex-structured Al_3Sc shares a similar formation mechanism with "sponge particles", "petal-like crystals", or "flower crystals", given the their resemblances in appearance and lattice structure. Two examples of such crystals are given by figure 2.3.

2.4 Previous investigations into the solidification behavior of the Al-Al_3Sc eutectic

The existing perspectives regarding the Al-Al_3Sc eutectic formation diverge. Tomus et al. (2010) reported a lamellar structure for the Al-Al_3Sc eutectic produced by both steel mold casting and electron beam processing, as shown in figure 2.4a, but their study was not focused on the eutectic formation, and did not provide further information about it. Brodova et al. (1998) suggested that the morphology of the Al-Al_3Sc eutectic is a function of both the melt overheat (with respect to the liquidus temperature) and the cooling rate. At a given mildly high overheat (< 400 ºC), they suggested that a needle-typed eutectic structure would transition to a globular type if a critical cooling rate is passed (ranging from ~100 to ~2000 $ºC \cdot s^{-1}$ as the overheat decreases). However, these two structures are not shown in the original work. Besides, with a higher overheat (> 400 ºC) and a faster cooling rate (> 10^4 $ºC \cdot s^{-1}$) concurrently, they described that the eutectic Al_3Sc phase has a "degenerated divided" form, and is indistinguishable from the proeutectic Al_3Sc phase in the same casting. Norman et al. (1998) and Hyde et al. (2001) proposed a divorced eutectic growth for the Al-Al_3Sc system. They believed that the difficulty in a coupled growth is a result of combined effects of the negligible volume fraction of the eutectic Al_3Sc, a sluggish growth kinetics of the intermetallic compound (Al_3Sc), and an excellent heterogeneous nucleation efficiency of α-Al on the proeutectic Al_3Sc phase (the last one only applicable to hypereutectic alloys). Consequently, following the completion of proeutectic Al_3Sc phase formation, a single-phase growth of the decoupled eutectic α-Al phase prevailed in the grain, while the decoupled eutectic Al_3Sc phase formed at the final stage, eventually siting in the grain boundaries, see figure 2.4b.

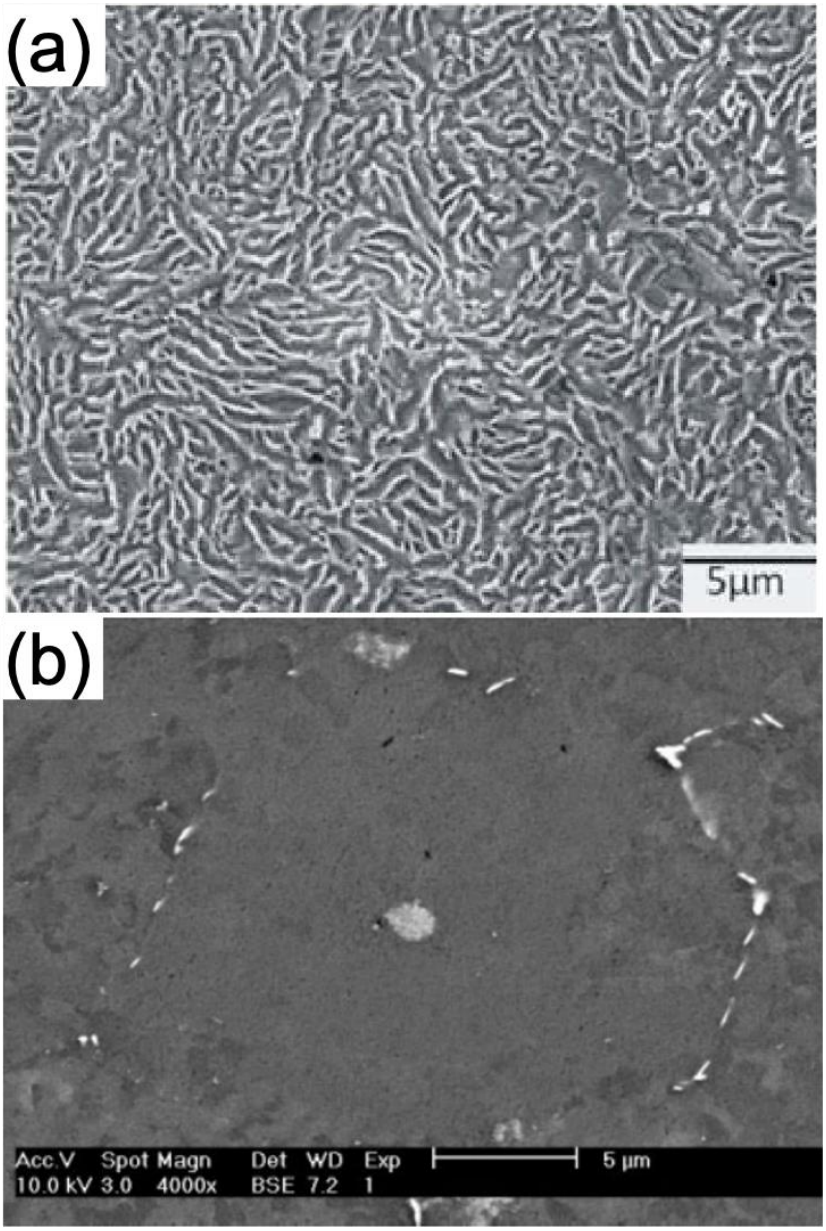

Figure 2.4 Two contrary perspectives about the structure of Al-Al_3Sc eutectic existing in the literature. (a) Lamellar structure. Reproduced from "Electron beam processing of Al–2Sc alloy for enhanced precipitation hardening," by D. Tomus, M. Qian, C. A. Brice, and B. C. Muddle, 2010, *Scripta Materialia*, *63*(2), p. 152 (https://doi.org/10.1016/j.scriptamat.2010.03.039). Copyright 2010 by Acta Materialia Inc. Reprinted with permission. (b) Decoupled structure. Reproduced from "Scandium in aluminium alloys," by J. Røyset and N. Ryum, 2005, *International Materials Reviews*, *50*(1), p. 26 (https://doi.org/10.1179/174328005X14311). Copyright 2005 by Institute of Materials, Minerals and Mining and ASM International. Reprinted with permission.

2.5 References

Blake, N., & Hopkins, M. A. (1985). Constitution and age hardening of Al-Sc alloys. *Journal of Materials Science, 20*(8), 2861-2867. https://doi.org/10.1007/BF00553049

Brodova, I. G., Bashlikov, D. V., & Polents, I. V. (1998). Influence of Heat Time Melt Treatment on the Structure and the Properties of Rapidly Solidified Aluminum Alloys with Transition Metals. *Materials Science Forum, 269-272*, 589-594. https://doi.org/10.4028/www.scientific.net/msf.269-272.589

Chu, M. G. (1994). Microstructure and solidification analysis of melt-spun Al-Ti and Al-Ti-B alloys. *Materials Science & Engineering A, 179-180*, 669-675. https://doi.org/10.1016/0921-5093(94)90290-9

Costa, S., Puga, H., Barbosa, J., & Pinto, A. M. P. (2012). The effect of Sc additions on the microstructure and age hardening behaviour of as cast Al–Sc alloys. *Materials and Design, 42*, 347-352. https://doi.org/10.1016/j.matdes.2012.06.019

Czerwinski, F. (2019). Critical assessment 36: assessing differences between the use of cerium and scandium in aluminium alloying. *Materials Science & Technology, 36*(3), 1-9. https://doi.org/10.1080/02670836.2019.1702775

Dorin, T., Ramajayam, M., Vahid, A., & Langan, T. (2018). Aluminium scandium alloys. In: R. Lumley (Ed.), *Fundamentals of Aluminium Metallurgy: Recent Advances* (pp. 439-494). Woodhead Publishing. https://doi.org/10.1016/B978-0-08-102063-0.00012-6

Haugan, T, Nes, E., & Ryum, N. (1983). Precipitation reactions in Al-Zr-alloys. *MRS Online Proceedings Library Archive, 21*, 495-499. https://doi.org/10.1557/PROC-21-495

Hyde, K. B., Norman, A. F., & Prangnell, P. B. (2001). The effect of cooling rate on the morphology of primary Al3Sc intermetallic particles in Al-Sc alloys. *Acta Materialia, 49*(8), 1327-1337. https://doi.org/10.1016/S1359-6454(01)00050-7

Khvan, A. V., Eskin, D. G., Starodub, K. F., Dinsdale, A. T., Wang, F., Fang, C., Cheverikin, V. V., & Gorshenkov, M. V. (2018). New insights into solidification and phase equilibria in the Al-Al3Zr system: Theoretical and experimental investigations. *Journal of Alloys and Compounds, 743*, 626-638. https://doi.org/10.1016/j.jallcom.2018.02.023

Marquis, E. A., & Seidman, D. N. (2001). Nanoscale structural evolution of Al3Sc precipitates in Al(Sc) alloys. *Acta Materialia, 49*(11), 1909-1919. https://doi.org/10.1016/S1359-6454(01)00116-1

Nes, E., & Billdal, H. (1977). Non-equilibrium solidification of hyperperitetic Al-Zr alloys. *Acta Metallurgica, 25*(9), 1031-1037. https://doi.org/10.1016/0001-6160(77)90132-8

Norman, A. F., Hyde, K., Costello, F., Thompson, S., Birley, S., & Prangnell, P. B. (2003). Examination of the effect of Sc on 2000 and 7000 series aluminium alloy castings: For improvements in fusion welding. *Materials Science & Engineering A, 354*(1), 188-198. https://doi.org/10.1016/S0921-5093(02)00942-5

Norman, A. F., Prangnell, P. B., & McEwen, R. S. (1998). The solidification behaviour of dilute aluminium–scandium alloys. *Acta Materialia, 46*(16), 5715-5732. https://doi.org/10.1016/S1359-6454(98)00257-2

Norman, A. F., & Tsakiropoulos, P. (1991a). The microstructure and properties of rapidly solidified Al-Hf alloys. *Materials Science & Engineering A, 134*, 1234-1237. https://doi.org/10.1016/0921-5093(91)90963-N

Norman, A. F., & Tsakiropoulos, P. (1991b). Rapid solidification of Al-Hf alloys - solidification microstructures and decomposition of solid-solutions, *International Journal of Rapid Solidification, 6*(3-4), 185-213.

Novikov, I. I., & Grushko, O. E. (1995). Hot cracking susceptibility of Al-Cu-Li and Al-Cu-Li-Mn alloys. *Materials Science and Technology, 11*(9), 926-932. https://doi.org/10.1179/mst.1995.11.9.926

Popova, E., Kotenkov, P., Shubin, A., & Gilev, I. (2020). Formation of Metastable Aluminides in Al–Sc–Ti (Zr, Hf) Cast Alloys. *Metals and Materials International, 26*(10), 1515-1523. https://doi.org/10.1007/s12540-019-00397-x

Riva, S., Yusenko, K. V, Lavery, N. P., Jarvis, D. J., & Brown, S. G. R. (2016). The scandium effect in multicomponent alloys. *International Materials Reviews, 61*(3), 203-228. https://doi.org/10.1080/09506608.2015.1137692

Røyset, J., & Ryum, N. (2005). Scandium in aluminium alloys. *International Materials Reviews, 50*(1), 19-44. https://doi.org/10.1179/174328005X14311

Shubin, A. B., Shunyaev, K. Y., & Kulikova, T. V. (2008). Problem of the thermodynamic properties of liquid aluminum alloys with scandium. *Russian Metallurgy Metally, 2008*(5), 364-369. https://doi.org/10.1134/S0036029508050029

Tomus, D., Qian, M., Brice, C. A., & Muddle, B. C. (2010). Electron beam processing of Al–2Sc alloy for enhanced precipitation hardening. *Scripta Materialia, 63*(2), 151-154. https://doi.org/10.1016/j.scriptamat.2010.03.039

Zhang, W. G., Ye, Y. C., He, L. J., Li, P. J., Feng, X., & Novikov, L. S. (2013). Dynamic response and microstructure control of Al–Sc binary alloy under high-speed impact. *Materials Science & Engineering A, 578*, 35-45. https://doi.org/10.1016/j.msea.2013.04.067

Zhou, S., Zhang, Z., Li, M., Pan, D., Su, H., Du, X., Li, P., & Wu, Y. (2016). Correlative characterization of primary particles formed in as-cast Al-Mg alloy containing a high level of Sc. *Materials Characterization*, *118*, 85-91. https://doi.org/10.1016/j.matchar.2016.05.011

CHAPTER 3. METHODOLOGY

The post-mortem strategy (or ex-situ observation) was adopted to investigate the solidification behaviors of the proeutectic Al_3Sc phase and the Al-Al_3Sc eutectic. This necessitated the remelting and solidification processes for the as-received Al-2 wt. % Sc master alloy, the preparation of metallographic specimens, the microscopic study with the aid of optical microscope (OM), scanning electron microscope (SEM), transmission electron microscope (TEM), and the microanalysis, such as energy dispersive X-ray spectrometer (EDX).

3.1 Melting and solidification processes

All the studied specimens were prepared from as-received hypereutectic Al-2 wt. % Sc master alloy. The specimens were melted in an electric resistance furnace, shown in figure 3.1, and afterwards, held at 1010 ºC for two hours to ensure the thorough dissolution of preexisting intermetallic compound prior to cooling.

To explore the influence of different cooling rates on the microstructural evolution of the proeutectic Al_3Sc phase and the Al-Al_3Sc eutectic, three different solidification conditions were exploited, designated as slow-, intermediate-, and fast-cooling in the text. The slow-cooling was to air-cool the molten alloy in a high alumina crucible to the room temperature. The estimated cooling for the slow-cooling method is 1 $ºC \cdot s^{-1}$ (Khvan et al., 2018). The intermediate-cooling was to pour 10 g of the molten alloy on a large copper plate. In fact, soon after the contact with the copper plate, the alloy melt ended up solidifying into a roundish film with a diameter of ~4 cm. The cooling rate can be estimated for this approach by solving a Newtonian heat transfer problem across the interface between solidifying metal and copper plate, see Appendix. Thus, the cooling rate for the intermediate-cooling is estimated to be on the order of 400 $ºC \cdot s^{-1}$. The fast-cooling method was to cast the molten alloy melt into an air-cooled wedge-shape copper mold with a wedge angle of 15°. A sketch of standard wedge ingot is displayed in figure 3.2. Norman and Tsakiropoulos (1991) gave an equation for the estimating cooling rate for the mid-plane (parallel to the *yz*-plane defined in figure 3.2) of the wedge casting:

$$\dot{T} = 2h_0(T - T_0)/zc_p \tag{3.1}$$

in which h_0 is the heat transfer coefficient, T the melt temperature, T_0 the mold temperature (or the room temperature), z the thickness of the wedge casting, and c_p the specific heat. Roughly, the cooling rate for the tip region of wedge casting is on the order of 1000 ºC·s^{-1}.

Figure 3.1 Electric resistance furnace

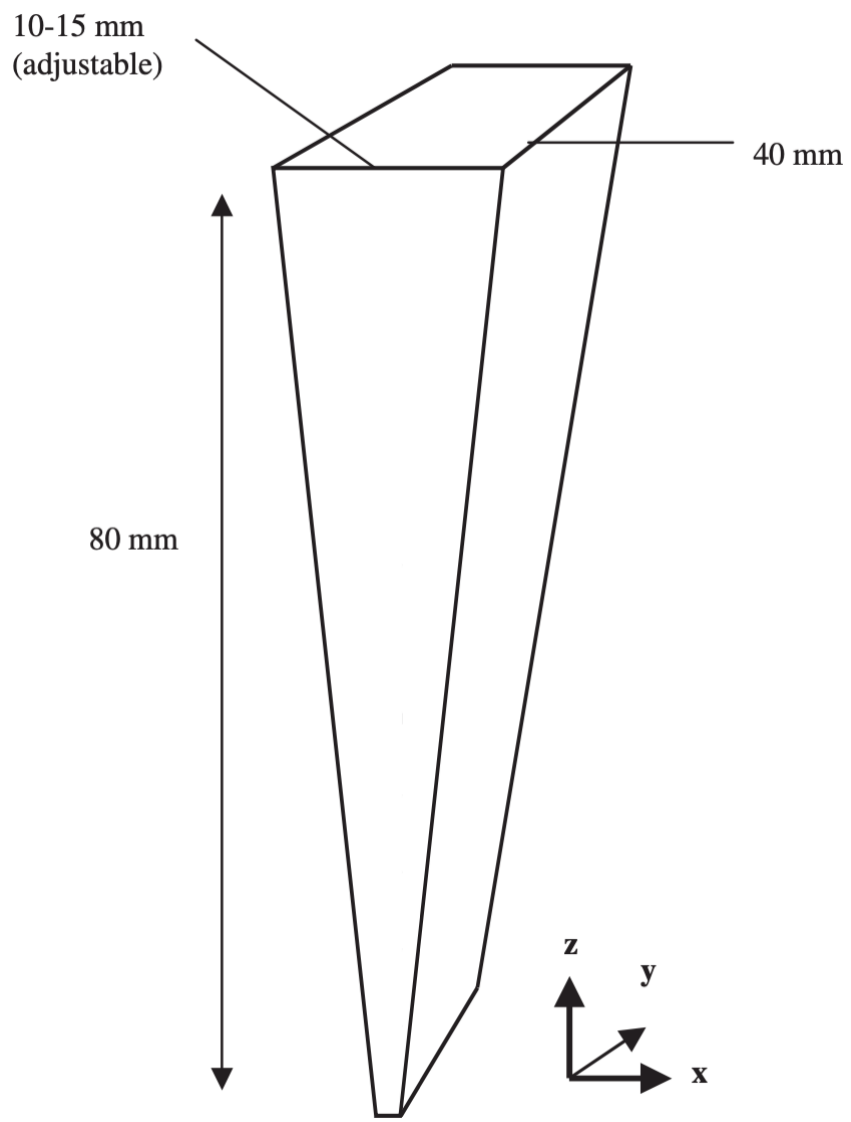

Figure 3.2 A schematic representation of standard wedge ingot. Reproduced from "Analysis of solidification microstructures during wedge-casting," by J. H. Perepezko and K. Hildal, 2006, *Philosophical Magazine*, *86*(24), p. 3683 (https://doi.org/10.1080/14786430500404116). Copyright 2006 by Taylor & Francis. Reprinted with permission.

3.2 OM and SEM specimen preparation

The OM and SEM metallographic specimens were acquired by sectioning in half for the slow-cooled ingot, or sectioning along a diameter for intermediated-cooled films, or sectioning along the mid-plane (parallel to the *xz*-plane defined in figure 3.2) for the fast-cooled wedge casting. All the metallographic specimens were subjected to the conventional treatments for grinding, polishing, and etching. Furthermore, to reveal three-dimensional (3-D) morphology of Al_3Sc

phase, an additional deep etching process to properly erode α-Al matrix was conducted. To this end, one half of the slow-cooled specimen and one half of the intermediate-cooled specimen were etched with a solution of 250 ml methanol containing 10 g iodine and 25 g tartaric acid for one hour.

3.3 TEM specimen preparation

A TEM foil with dimensions of 20 μm × 10 μm × 0.1 μm was cut by focused ion beam (FIB) at an interface between an α-Al matrix and a proeutectic Al_3Sc particle in the half of the slow-cooled specimen that did not undergo deep etching.

3.4 Microstructural examination

Microstructural examination was performed on Zeiss Axioscope 7 optical microscope, see figure 3.3, FEI 3D Quanta dual beam SEM, FEI Nova NanoSEM, and FEI Titan 80-300 TEM. EDX analyses were conducted on FEI Nova NanoSEM at 10 kV and FEI Titan 80-300 TEM at 200 kV. Both secondary electron (SE) and back-scattered electron (BSE) modes were utilized on SEM.

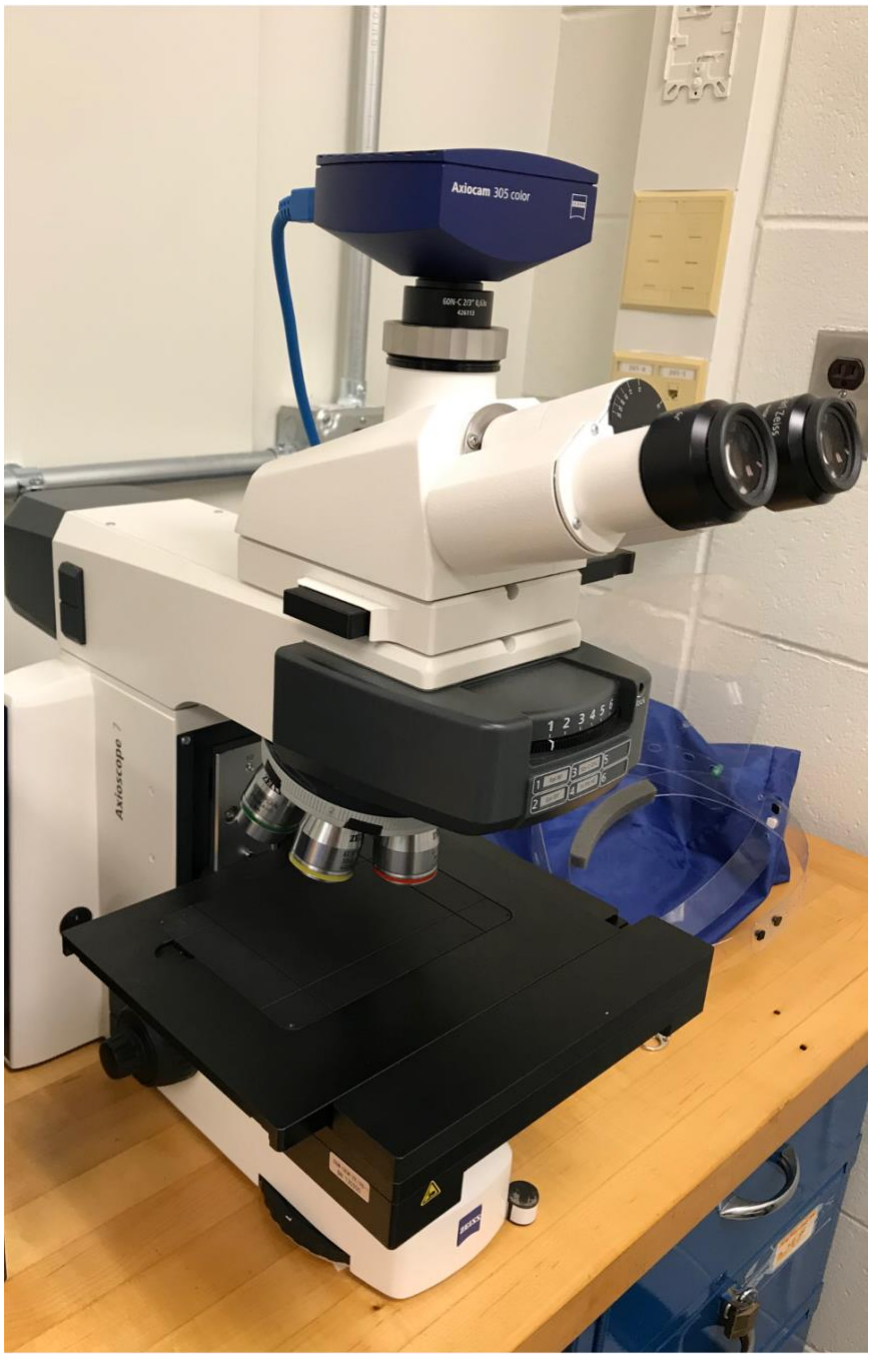

Figure 3.3 Zeiss Axioscope 7 optical microscope

3.5 Derivation of some specific parameters in the microstructure

3.5.1 The fractal dimension

The fractal dimension, d_f, is a measure to characterize fractal structures, defined as (Wu et al., 2021):

$$d_f = \lim_{S \to \infty} \frac{\log N(S)}{\log S}$$

where $N(S)$ is the number of boxes required to cover the analyzed fractal structure, which is a function of the scale down factor, S. However, since it is not practical to use an infinite S, d_f was estimated via a linear relationship, $\log N(S) = d_f \log S + C$, C being a constant. A rough plot of $\log N(S)$ versus $\log S$ was obtained by using several pairs of $N(S)$ and S. Next, a linear fitting to the plot gave the slope, i.e., d_f. This approximation approach is also known as the box counting method.

3.5.2 The radius of dendrite tip

The radius of dendrite tip, ρ, is a significant and measurable variable for the dendritic growth. A simple relationship was used to measure ρ (Hürlimann et al., 1992):

$$\rho = h^2/2d$$

where h is the half width of dendrite at a distance of d behind the tip.

3.5.3 The eutectic interphase spacing and the volume fraction of eutectic phase

The eutectic interphase spacing, λ, is a significant and measurable variable for the eutectic growth. However, the intrinsic difficulty in identifying the eutectic spacing is unavoidably encountered in the study. This is because both exploited cooling methods offer the unconstrained growth (Kurz & Fisher, 1998) in undercooled melts, and the solidification condition is expected to vary constantly, even though the variation can be mild in the slow-cooled melt. Therefore, the eutectic spacing can be inhomogeneous from spot to spot. To overcome this inhomogeneity, the eutectic spacing was estimated across a region with an area of 25 to 100 μm^2. When possible, this practice was repeated in multiple regions, and afterwards, the average was taken. Besides, for the rod eutectic present in this work, despite irregularities, a hexagonal packing pattern was

assumed, which is a typical form (Jackson & Hunt, 1966; Teng et al., 2008; Trivedi & Wang, 2012). With the hexagonal packing pattern, each rod nominally occupied an area of $0.867\lambda^2$. Hence, for a region of an area A, in which n eutectic rods grew normal to the cross-section, the eutectic spacing was estimated as $\lambda = \sqrt{A/0.867n}$.

Moreover, assuming each rod with a unified diameter d, the volume fraction of rods, f, was given by $f = \pi n d^2/4A$.

3.6 References

Hürlimann, E., Trittibach, R., Bisang, U., & Bilgram, J. H. (1992). Integral parameters of xenon dendrites. *Physical Review A, 46*(10), 6579-6595. https://doi.org/10.1103/PhysRevA.46.6579

Jackson, K. A., & Hunt, J. D. (1966). Lamellar and rod eutectic growth. *Transactions of the Metallurgical Society of AIME, 236*(6), 1129-1142.

Khvan, A. V., Eskin, D. G., Starodub, K. F., Dinsdale, A. T., Wang, F., Fang, C., Cheverikin, V. V., & Gorshenkov, M. V. (2018). New insights into solidification and phase equilibria in the Al-Al3Zr system: Theoretical and experimental investigations. *Journal of Alloys and Compounds, 743*, 626-638. https://doi.org/10.1016/j.jallcom.2018.02.023

Kurz, W., & Fisher, D. (1998). *Fundamentals of Solidification* (4th rev. ed.). Trans Tech Publications, Uetikon-Zuerich.

Norman, A. F., & Tsakiropoulos, P. (1991). Rapid solidification of Al-Hf alloys - solidification microstructures and decomposition of solid-solutions, *International Journal of Rapid Solidification, 6*(3-4), 185-213.

Perepezko, J. H., & Hildal, K. (2006). Analysis of solidification microstructures during wedge-casting. *Philosophical Magazine, 86*(24), 3681-3701. https://doi.org/10.1080/14786430500404116

Teng, J., Liu, S., & Trivedi, R. (2008). Growth and morphology of rod eutectics. *Acta Materialia, 56*(12), 2819-2833. https://doi.org/10.1016/j.actamat.2008.02.011

Trivedi, R., & Wang, N. (2012). Theory of rod eutectic growth under far-from-equilibrium conditions: Nanoscale spacing and transition to glass. *Acta Materialia, 60*(6-7), 3140-3152. https://doi.org/10.1016/j.actamat.2012.02.020

Wu, M., Wang, W., Shi, D., Song, Z., Li, M., & Luo, T. (2021). Improved box-counting methods to directly estimate the fractal dimension of a rough surface. *Measurement*, 109303. https://doi.org/10.1016/j.measurement.2021.109303

CHAPTER 4. DENDRITIC AND SEAWEED GROWTH OF PROEUTECTIC SCANDIUM TRI-ALUMINIDE IN HYPEREUTECTIC AL-SC UNDERCOOLED MELT

The following chapter was reprinted, with journal permission, from Jiang, A., & Wang, X. (2020). Dendritic and seaweed growth of proeutectic scandium tri-aluminide in hypereutectic Al-Sc undercooled melt. *Acta Materialia, 200*, 56-65. https://doi.org/10.1016/j.actamat.2020.08.078

4.1 Introduction

The formation of proeutectic Al_3Sc in a hypereutectic Al-Sc alloy was proven to remarkably refine Al-based alloys (Norman et al., 1998). However, the study of the morphology of proeutectic Al_3Sc (with an $L1_2$ structure), especially produced under rapid solidification conditions, is still scarce and incomplete. In general, a slow cooling rate leads to the formation of separated or cluster of polyhedral Al_3Sc particles (Blake & Hopkins, 1985; Brodova et al., 1998; Hyde et al., 2001). On the other hand, a duplex structure, with a cubic core at the center and a layer of fine-scale cellular-dendritic structures decorating the periphery of the particle, has been found to form at a fast cooling rate (Hyde et al., 2001). In fact, the duplex structure has also been reported for some other similar systems, i.e., $L1_2$-structured metastable β'-Al_3Zr (Haugan et al., 1983; Nes & Billdal, 1977; Ohashi & Ichikawa, 1972; Srinivasan & Chattopadhyay, 2005), β'-Al_3Hf (Norman & Tsakiropoulos, 1991a, 1991b), β'-Al_3Ti (Chu, 1994; Hori et al., 1985), and their ternary Al-based alloys, such as $Al_3(Sc,Zr)$ (Singh et al., 2002), $Al_3(Ti,Zr)$ (Popova et al., 2012), and $Al_3(Sc,Hf)$ (Popova et al., 2017). Such a duplex structure was termed "sponge particles" (Haugan et al., 1983), "petal-like crystals" (Hori et al., 1985; Norman & Tsakiropoulos, 1991b), and "flower crystals" (Khvan et al., 2018) in the literature, hereafter referred to as sponge particle. Different investigators have attempted to elucidate the formation mechanism of sponge particle, with emphasis on the fine-scale cellular-dendritic structures. Haugan et al. (1983) suggested a solid-solid reaction, in which, according to the metastable phase diagram, β'-Al_3Zr contained decreasing Zr content as temperature dropped. Thus, α-Al had an increasing tendency to precipitate inside the β' particle via β'_{ss} to β' + α, β'_{ss} denoting supersaturated β' phase, and was produced to a larger amount on the periphery of the β' particle than at the center, justifying that β' dendrites had a higher density at the center than the periphery. Nes and Billdal (1977), like many other researchers, considered that the fine internal

structure for β'-Al_3Zr formed directly in the melt, but they ascribed the formation of the sponge particle to that the cubic core first formed due to sufficient supply of solute atoms, while the subsequent formation of dendrite was favored by the decreased concentration of Zr. Srinivasan and Chattopadhyay (2005) suggested that the interfacial instability that finally developed into fine cellular structures was caused by the diffusion of the third element in a ternary alloy. Chu (1994) proposed that the cellular-dendritic structures should be due to the breakdown of a plane interface, since the growth rate of crystals can change significantly during solidification. Similarly, Hyde et al. (2001) suggested that the formation of dendrites arose from the kinetic roughening, i.e., faceting-to-non-faceting transition upon increasing undercooling, and further proposed a growth model, in which the formation of a solid core was immediately followed by the growth of primary <111> stems, secondary <110>, and tertiary <100> branches.

Despite the above outstanding investigations into the formation mechanism of sponge particle, numerous questions still remain unanswered. For instance, why a typical depiction of such a sponge particle is a faceted cubic core surrounded by cellular-dendritic structures? This structure implies that an abrupt increase in the driving force (undercooling) occurred to the particle during growth, as opposed to the usual situation in that the undercooling keeps decreasing as the latent heat is constantly released and piled up at the solid/liquid (S/L) interface. In this case, a kinetic roughening phenomenon that occurs at a late stage of growth does not seem very likely. Then, what is the alternative model? Furthermore, why the scale for the cellular-dendritic structures is so fine, as Nes and Billdal (1977) reported in their study, the width of dendritic structure can be as thin as ~10 nm, and the radius of dendrite tip ~2-4 nm. Besides, are there any other types of morphologies that have never been analyzed for proeutectic Al_3Sc? Bearing these questions in mind, the present chapter aimed to investigate the formation mechanism of proeutectic Al_3Sc in Al-2 wt. % Sc undercooled melts with different cooling rates in detail.

4.2 Experimental

All investigated specimens were prepared from as-received Al-2 wt. % Sc master alloy, melted by an electric resistance furnace, and held at 1283 K for two hours to ensure full dissolution of intermetallic compound (IMC) prior to cooling. Slow, intermediate, and fast cooling rates were achieved by different cooling techniques. The slow cooling method was to air-cool 10 g of

molten Al-2 wt. % Sc master alloy in a high alumina crucible, with a rough estimated cooling rate of ~1 $K \cdot s^{-1}$ (Khvan et al., 2018). The intermediate cooling method was to pour 10 g of the alloy melt on a large copper plate. Soon after the contact with the copper plate, the alloy melt ended up solidifying into a roundish film with a diameter of ~4 cm. To roughly estimate the cooling rate for this approach, a Newtonian heat transfer problem across the interface between solidifying metal and copper plate needs to be addressed, see Appendix. The cooling rate was estimated to be on the order of 400 $K \cdot s^{-1}$. The fast cooling method was to quench the alloy melt by the tip portion of an air-cooled wedge-shape copper mold with a wedge angle of 15°. Specifically, the examined area was at the wedge thickness of ~2 mm, where the cooling rate was estimated to be ~1×10^3 $K \cdot s^{-1}$ (Norman & Tsakiropoulos, 1991b).

The metallographically polished scanning electron microscopy (SEM) specimens were obtained by sectioning in half for the air-cooled casting, or along a diameter for the copper-cooled film, or along the midline and parallel to *xz*-plane (Perepezko & Hildal, 2006) for the wedge-shape casting. In order to disclose three-dimensional (3-D) morphology for Al_3Sc particle, polished specimens were subjected to deep etching by a solution of 250 ml methanol containing 10 g iodine and 25 g tartaric acid (Liu et al., 2017).The transmission electron microscopy (TEM) specimen was secured by focused ion beam (FIB) cutting a foil with dimensions of 20 µm×10 µm×0.1 µm at an interface between proeutectic Al_3Sc and α-Al matrix in a slow-cooled specimen.

Microstructural examination was performed under FEI 3D Quanta dual beam SEM equipped with an energy dispersive X-ray (EDX) system, operating at 10 kV, and FEI Titan 80-300 TEM, operating at 200 kV. All regular polished specimens were imaged by SEM back-scattered electron (BSE) mode, whereas all deeply etched specimens were imaged by SEM secondary electron (SE) mode. Besides, the grain size is estimated by means of a linear intercept method, and the fractal dimension is estimated by the box counting method, see section 3.5.1.

4.3 Results

4.3.1 The scale of refined grains

The Al-2 wt. % Sc master alloy has a hypereutectic composition, and thus, Al_3Sc particles formed as the proeutectic phase. Figure 4.1a-c disclose the typical scale of refined grain in the

slow-, intermediate-, and fast-cooled specimens, respectively. Apparently, the grain size is reduced with the rate of heat extraction, in good agreement with the work by Hyde et al. (2001). Specifically, the mean grain size is ~120 μm for slow-cooled specimens, ~60 μm for intermediate-cooled specimens, and ~30 μm for fast-cooled specimens, respectively. The grain refinement was achieved by efficient heterogeneous nucleation of α-Al on Al_3Sc. Figure 4.2 shows a bright-field TEM image of the interface between α-Al matrix (left-hand side) and proeutectic Al_3Sc (right-hand side) in a FIB-cut, slow-cooled specimen. The parallel orientation relationship between α-Al and the nucleant Al_3Sc, i.e., $(100)_{Al}||(100)_{Al3Sc}$ and $[010]_{Al}||[010]_{Al3Sc}$, has been confirmed by electron diffraction, the inset of figure 4.2. The fibrous structures at the interface will be discussed in a separate paper.

In the next three sections, the main characteristics in the morphology of Al_3Sc will be described under different solidification conditions, despite some variations in each specimen.

Figure 4.1 Refined α-Al grains and various forms of cross-sections for proeutectic Al_3Sc in different specimens. (a) Polygonal cross-sections in the slow-cooled specimen; (b) split, angular, and hierarchical cross-sections in the intermediate-cooled specimen; (c) irregular cross-sections in the fast-cooled specimen.

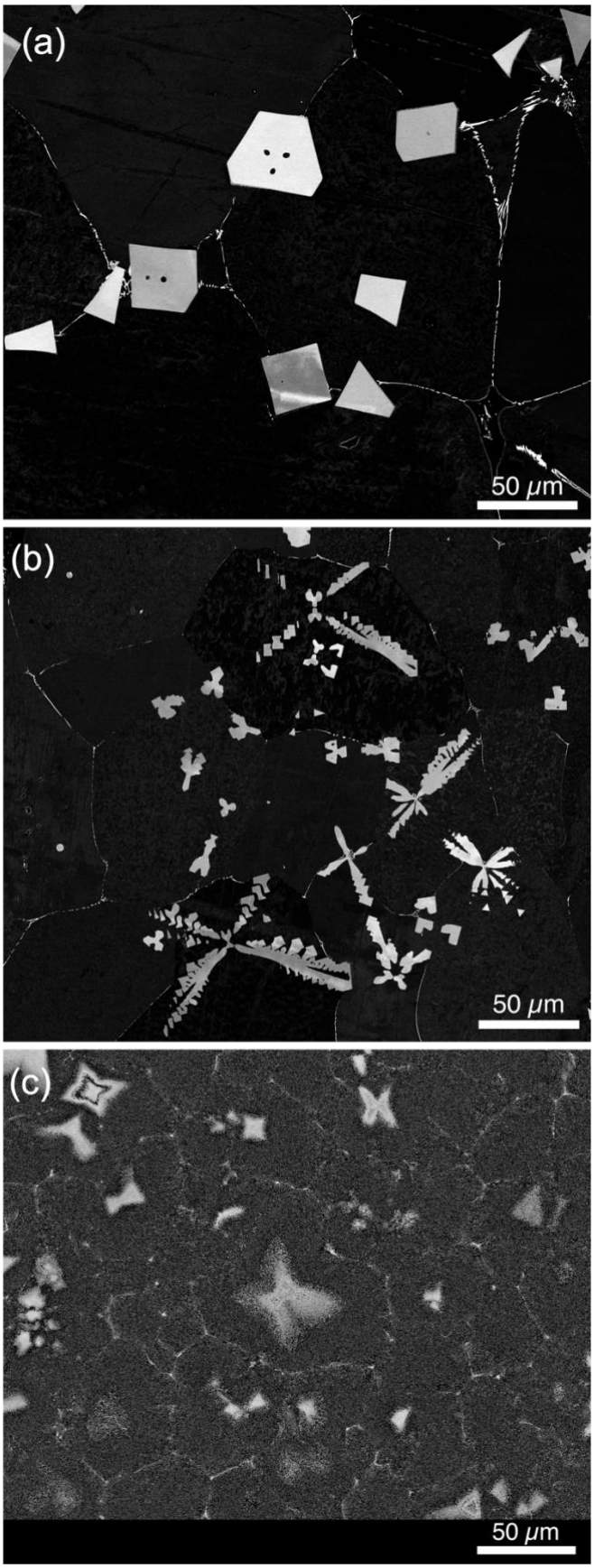
(a)
50 μm
(b)
50 μm
(c)
50 μm

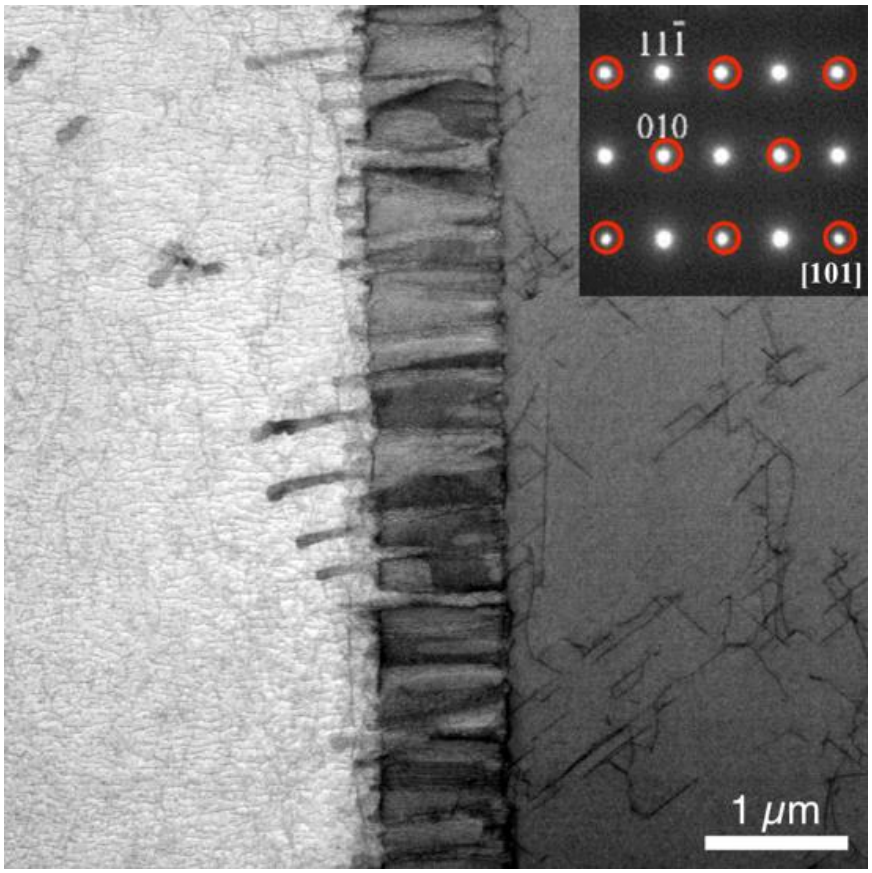

Figure 4.2 A bright-field TEM image of the interface of α-Al matrix (left-hand side) and proeutectic Al_3Sc (right-hand side). The inset confirms the parallel orientation relationship between them, i.e., $(100)_{Al}||(100)_{Al3Sc}$ and $[010]_{Al}||[010]_{Al3Sc}$. The red circles in the inset indicate the diffraction pattern from Al_3Sc, while the uncircled pattern corresponds to both phases.

4.3.2 Slow-cooled specimen

The polygons with flat interfaces are the predominant pattern for proeutectic Al_3Sc's cross-section in slow-cooled specimens, figure 4.1a. The etching process eroded α-Al matrix, and extracted Al_3Sc, further revealing that the slow-cooled proeutectic Al_3Sc is of a cubic form with a size of ~30 µm, figure 4.3. Similar finding of such Al_3Sc cubes has also been reported in (Hyde et al., 2001; Norman et al., 1998).

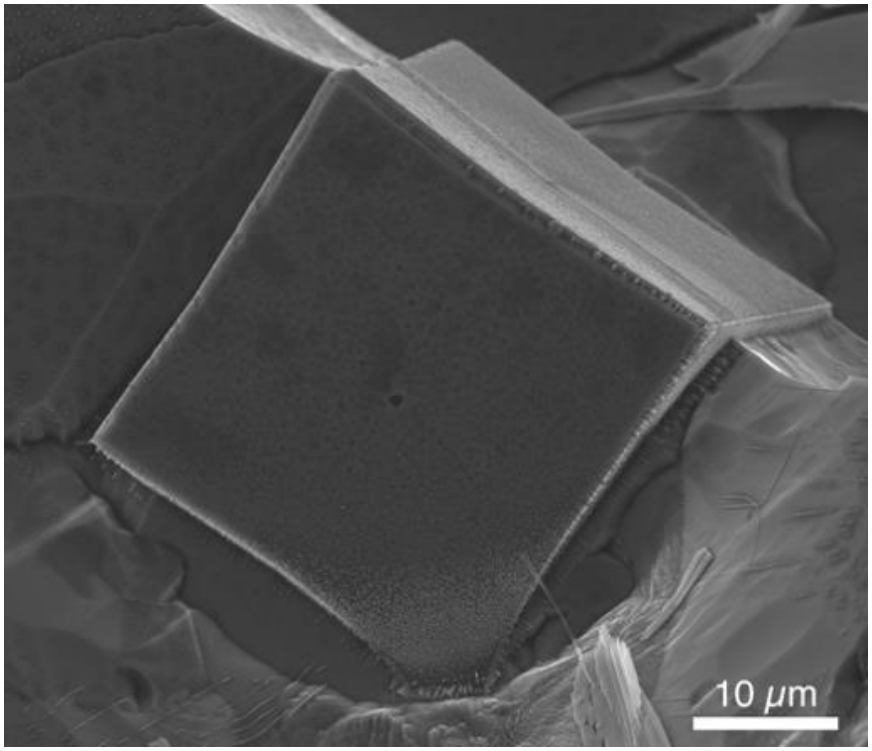

Figure 4.3 An SEM image of an extracted cubic Al_3Sc particle bounded by flat {100} facets

4.3.3 Intermediate-cooled specimen

When solidifying on a copper plate, split, angular, and hierarchical cross-sections appeared, figure 4.1b. An additional high-magnification micrograph for angular cross-section is exhibited in figure 4.4a. The extracted Al_3Sc particles, which are responsible for the split and angular cross-sections, turn out to be "hopper-like", figure 4.4b, whereas the hierarchical cross-section is linked to a complex dendritic structure shown in figure 4.4c. To the best knowledge of the author, these two types of structures have seldom been discussed for Al_3Sc, nor even for β'-Al_3TM (TM=Ti, Zr, and Hf), although some micrographs of sectioned specimens from earlier studies, e.g., figure 1 in (Blake & Hopkins, 1985), figure 2a in (Norman & Tsakiropoulos, 1991b), and figure 8 in (Norman et al., 1998), may suggest their occurrence. Furthermore, the complex dendritic structure in this case should be distinguished with the cluster of cubes obtained by slow cooling (Blake & Hopkins, 1985), despite some similarities, see section 4.4.2.

Figure 4.4 SEM images of proeutectic Al_3Sc in the intermediate-cooled specimens. (a) Angular cross-section and (b) the 3-D morphology of a hopper-like Al_3Sc particle; (c) the 3-D morphology of a hierarchical Al_3Sc particle.

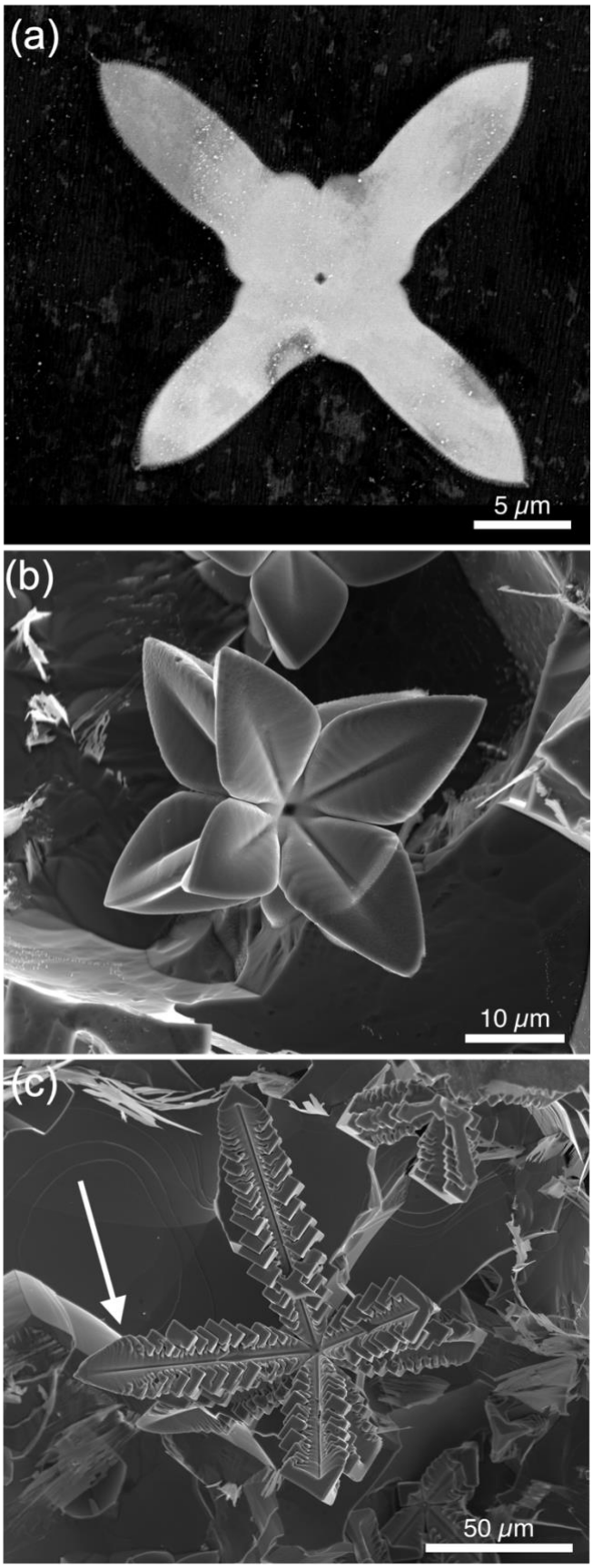
(a)
5 μm
(b)
10 μm
(c)
50 μm

4.3.4 Fast-cooled specimen

The Al_3Sc sponge particle, with irregular cross-sections, was produced at the fast cooling rate, figure 4.1c. As suggested by other investigators (Haugan et al., 1983; Hyde et al., 2001; Nes & Billdal, 1977), the sponge particles seem to have an inner core surrounded by fine-scale, highly branched structures. The corresponding cross-section takes a cusped-square, figure 4.5a, or a more distorted form, figure 4.5d. It is assumed that the particles in figure 4.5a and 4.5d were sectioned through their centers. A striking observation is shown in a close-up, figure 4.5b, for the particle in figure 4.5a: The inner core is of fine-scale, highly branched structures too, instead of a simple solid core as previously considered. Furthermore, the external branches seem to seamlessly grow on the internal ones, with the only difference that the inside structure is more compact than the outside. The cusped-square cross-section suggests two types of contours for the sponge particle in 3-D – a distorted octahedron with six extended vertices along <100> directions, on the left in figure 4.5c, and a distorted cube with eight extended vertices along <111> directions, on the right in figure 4.5c. If the sponge particle is sectioned through its center and normal to a principal axis, e.g., *c* axis, the cross-section will show such a cusped-square pattern, see the dark regions in figure 4.5c. However, the scattered triangular cross-sections in figure 4.1c only support the presence of distorted cubic sponge particles. This is because if the particle is sectioned through an individual “petal”, only the petal in a distorted cube can show a three-fold symmetry. The distorted cubic configuration also explains the presence of the irregular pattern in figure 4.5d, that is, the sponge particle was sectioned with a tilted angle with respect to principle axes.

Figure 4.5 SEM images of proeutectic Al_3Sc in the fast-cooled specimens. (a) Cusped-square cross-section of an Al_3Sc sponge particle shows two distinctive densities of the center and the periphery. (b) A close-up of (a) shows the details of highly branched structures. Inset: bifurcation of a branch, the spacing between two neighboring branches, λ. (c) Two potential 3-D contours, distorted tetrahedron (left) and distorted cube (right), for the sponge particles are sketched by simplified geometries, when considering the cross-sectional pattern in (a). (d) Distorted cross-section of an Al_3Sc sponge particle shows porous structures at the center. (e) Al_3Sc tiny particles are present. The magnified images of them suggest a 3-D cusped-cubic morphology, whose simplified model is to the right.

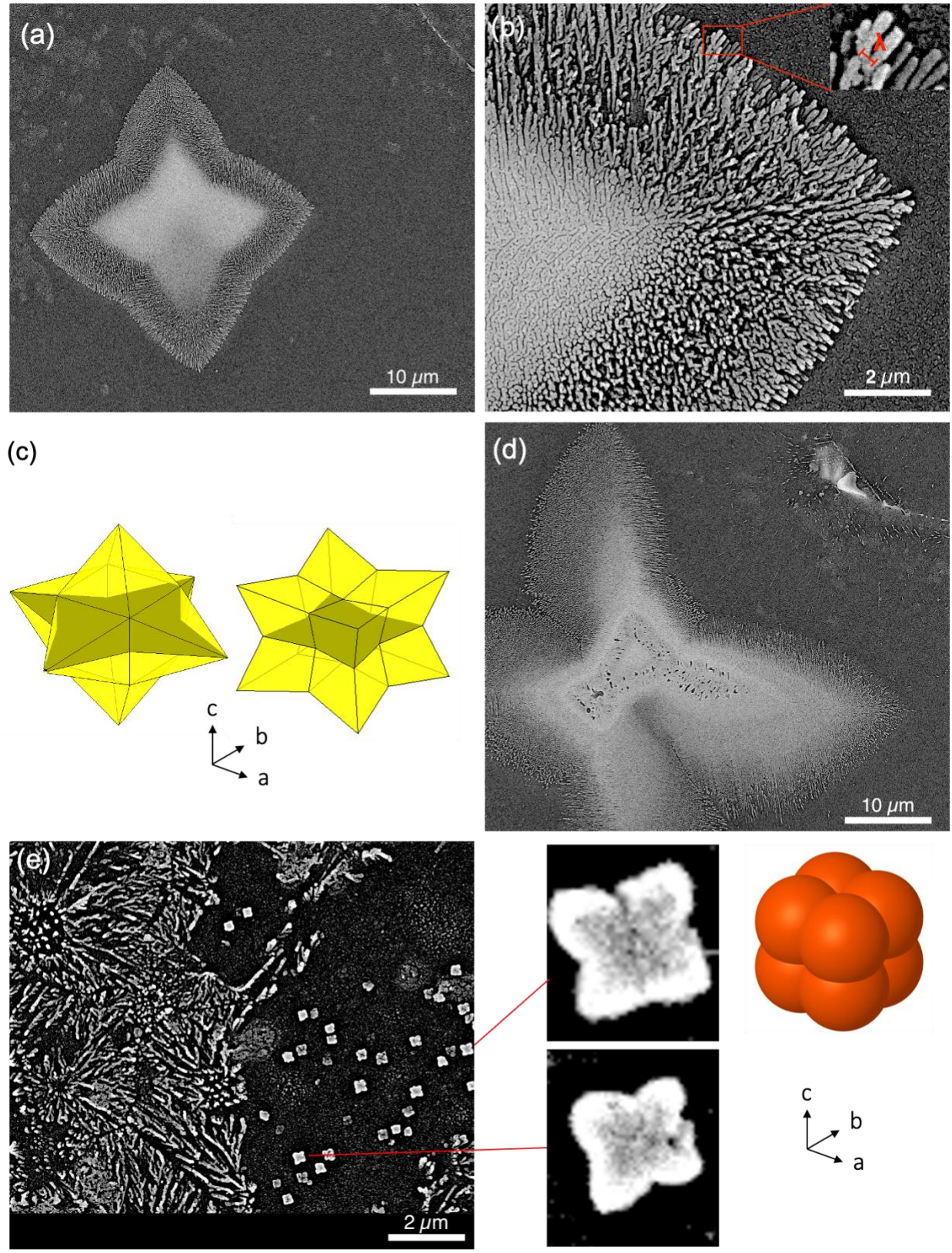
(a)
10 μm
(b)
λ
2 μm
(c)
c
b
a
(d)
10 μm
(e)
2 μm
c
b
a

Besides, a well-defined "backbone" and a self-preserving tip that are characteristic of dendrites are absent in sponge particles. Instead, an individual branch is weakly anisotropic in growth direction selection, and experienced a cascade of tip splitting, reminiscent of dense branch morphology. Further details of tip splitting are revealed in the inset of figure 4.5b, where an old branch (left lower corner) became morphologically unstable during advance, and bifurcated into two new branches. The spacing between these two adjacent tips, λ, at the moment of bifurcation can be viewed as a characteristic length scale, see the inset of figure 4.5b, and λ ~0.2 μm. In addition, some porous structures occasionally appear at the center of a sponge particle, figure 4.5d. A flock of tiny particles were found next to a sponge particle, figure 4.5e. Two of them are magnified in comparison to a postulated 3-D model, which is of a cuboidal form, with eight corners protruding outwards. The comparison suggests that the tiny particles have the same 3-D configuration as in the model. Moreover, the protrusion's scale is on the same order of the width of a branch.

4.4 Discussion

4.4.1 Fundamental considerations about growth anisotropy

From the above results, the growth anisotropy is evident, which is contributed by different aspects. In general, four undercooling components need to be considered for a growing IMC in an undercooled alloy melt: Namely, the melt undercooling, $\overline{\Delta T}$, is the sum of the constitutional undercooling, $\overline{\Delta T_s}$, the thermal undercooling, $\overline{\Delta T_t}$, the curvature undercooling, $\overline{\Delta T_r}$, and the kinetic undercooling, $\overline{\Delta T_k}$, as expressed in a dimensionless version as $\overline{\Delta T} = \overline{\Delta T_s} + \overline{\Delta T_t} + \overline{\Delta T_r} + \overline{\Delta T_k}$, where $\overline{\Delta T_r} = d(\theta - \theta_d)\kappa$, $\overline{\Delta T_k} = \beta(\theta - \theta_\beta)V$, $d(\theta - \theta_d)$ the orientation-dependent capillarity length, θ the angle between the interface normal and a given direction, θ_d the offset angle for surface tension, κ the interface curvature, $\beta(\theta - \theta_\beta)$ the orientation-dependent kinetic coefficient, θ_β the offset angle for kinetic coefficient, and V the growth rate. In fact, the last two undercooling terms are curvature and velocity corrections, respectively, according to Gibbs-Thomson condition. It should be noted that only one orientation parameter, i.e., θ, is involved for mathematical simplicity, and the above equations only hold for two dimensions (2-D). The anisotropy in growth would decisively be determined by these two inherent microscale factors,

i.e., surface tension and atomic attachment kinetics (Ben-Jacob, 1993; Liu et al., 2011), if external macroscale factors did not play an important role, e.g., without an external thermal field. Usually, at a slow or intermediate cooling rate, when the dimensional kinetic undercooling may be no more than 1 K, the effect of attachment kinetics can be ignored. At a higher cooling rate, a joint effect of surface tension and kinetics anisotropies on the morphology selection may prevail, and at a sufficiently fast cooling rate, the effect of kinetics anisotropy becomes dominant (Ben-Jacob et al., 1988).

In the following three sections, 4.4.2 to 4.4.4, the formation mechanisms for proeutectic Al_3Sc particles produced by different cooling rates will be given. However, the experimental results only provide a few discrete moments during solidification. To construct the whole picture of growth process, some 2-D schematics in figure 4.7 and figure 4.8 will be used to connect these discrete moments. For simplicity, the 2-D schematics use the diagonal to represent <111> directions, and use vertical and horizontal directions to represent <100> directions, despite somehow mathematically problematic. In section 4.4.5, some observed characteristic length scales in structure are to be compared with the estimated valued derived from morphological stability analyses, to verify the proposed growth models.

4.4.2 Slow-cooled specimen

A convenient interface roughness parameter proposed by Hunt and Jackson (1966) for Al_3Sc is estimated to be ~5, see table 4.1, which is larger than the critical value two, suggesting that the melting point is below the thermal roughening temperature (Saito, 1996). Meanwhile, the operating slow cooling rate did not provide a driving force large enough to exceed the kinetic roughening threshold, and thus, the slow-cooled Al_3Sc grew in a faceted manner. The kinetic roughening threshold, here, refers to a critical undercooling beyond which the growth mechanism transitions from the lateral growth (growth needs lateral step motion) to the continuous growth (growth does not need steps) (Cahn et al., 1964). Note, in solidification, it is more convenient to correlate the driving force with the undercooling. Lacking pertinent experimental data, the author arbitrarily locates the kinetic roughening threshold for Al_3Sc in an Al-2 wt. % Sc melt, indicated by the dotted line on the right panel of figure 4.6, somehow lower than the liquidus temperature. For comparison, the hypothetical cooling curve for slow cooling is schematically represented by the green curve. After the formation of an initially spherical

nucleus at or near the largest undercooling, multiple competing crystalline planes were growing simultaneously. The planes that grew fast disappeared eventually, while the slowest growing planes remained and became the exposed facets. Roughly speaking, the exposed facets are dictated by Wulff's plot (Wulff, 1901) that follows Gibbs' concept of a minimum of the total interface energy times interface area (Gibbs, 1878). The present experimental results, i.e., the cubic form of proeutectic Al_3Sc, and the cubic-on-cubic orientation relationship between proeutectic Al_3Sc and α-Al matrix, confirm that{100} planes are the slowest growing planes for proeutectic Al_3Sc, in good agreement with previous studies (Blake & Hopkins, 1985; Hyde et al., 2001).

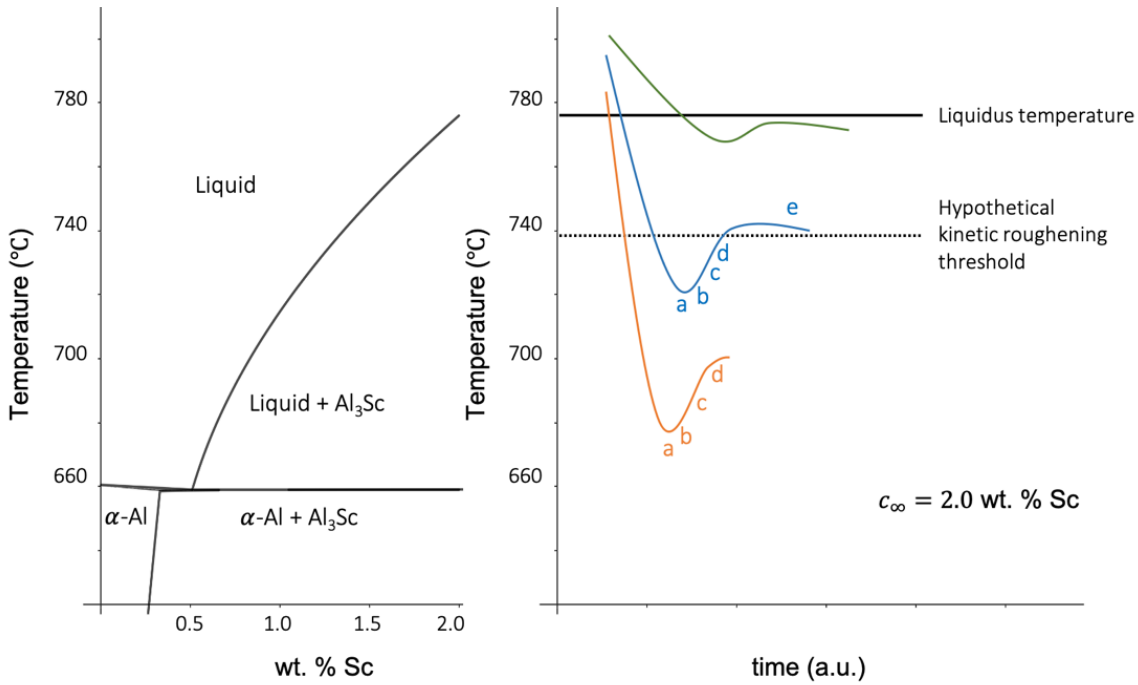

Figure 4.6 Al-rich side of Al-Sc phase diagram, on the left panel, adapted from (Dorin et al., 2018), and the hypothetical cooling curves for the slow- (green), intermediate- (blue), and fast-cooling (orange) methods, on the right panel. The dotted line represents a hypothetical kinetic roughening threshold for the melt composition of 2 wt. % Sc.

4.4.3 Intermediate-cooled specimen

At an intermediate cooling rate, the hopper-like structure (also known as skeletal structure), with depressed facets and needle-like protrusions stretching in eight <111> directions, figure 4.4b, may trigger more than one interpretations. A natural conjecture is to ascribe the formation of

protruding corners to favorable growth conditions at corners and edges of a polyhedron, i.e., the Berg effect (Saito, 1996). When the driving force at the corners enters the transitional regime that separates classical lateral growth and continuous growth (Cahn et al., 1964), the step free energy decreases and even vanishes, resulting in the generation of multitude of diffuse steps at corners (Peteves & Abbaschian, 1991). If the time required for a step spreading over the whole facet is much longer than the time interval between step deposition events, the corners and edges grow faster than facet's center, forming a skeletal structure. Besides, the rejected impurities, if any, tend to accumulate at the center of facet, further lowering the local growth rate, or even ceasing the growth at the center, and enhancing the skeletal morphology (Chernov, 1974).

However, given that the hopper-like particle has regular paraboloidal tips, and both the hopper-like particle and the complex structure have the identical well-defined growth directions, it is proposed that these two structures are at different stages of the growth of equiaxed dendrites. The growth model is elucidated as follows. Dendritic growth is diffusion-limited. Thus, the initial operating undercooling went beyond the kinetic roughening threshold, represented by the blue hypothetical cooling curve in figure 4.6. After nucleation, the S/L interface became unstable, when the radius of spherical solid, R, exceeded the critical radius, R_c, illustrated by schematics in figure 4.7a and 4.7b, corresponding to the steps ***a*** and ***b*** on the blue curve. The R_c is estimated to be ~4.1 µm, according to the morphological stability analysis for a growing spherical solid in a binary alloy melt proposed by Trivedi (1980), see section 4.4.5.3. This estimated value is close enough to the observed R_c, which is disclosed by figure 4.4a, roughly 4 µm. Afterwards, eight protrusions, developing from infinitesimal perturbations on the spherical front, projected in <111> directions, see figure 4.7b and step ***b*** in figure 4.6. With the presence of anisotropy in surface tension, Al_3Sc took the equiaxed dendritic form with a paraboloidal tip, free of side branches, and kept growing along <111> growth directions, figure 4.4b, figure 4.7c, and step ***c*** in figure 4.6. The further growth of equiaxed dendrites did not change the shape of dendrite tip, but stimulated wave-like side branches on the dendrite stems, figure 4.7d and step ***d*** in figure 4.6, although the physical origin of side branches is still uncertain yet (Glicksman, 2015). However, most of the wave-like side branches were covered by the faceted macrosteps, figure 4.4c. Only few of them can still be seen by the vestigial structure indicated by the arrow in figure 4.4c. At a late stage of growth, the recalescence effect reduced the undercooling above the kinetic roughening threshold. The lateral growth prevailed again, and modified dendrite tips and

side branches with faceted macrosteps, which are of {100} planes, figure 4.4c, figure 4.7e, and step ***e*** in figure 4.6. The deceiving appearance of macrosteps may easily lead one to think that the presented complex structure has the same roots as what was observed by Blake and Hopkins (1985), which solidified very slowly. Even though not specified in their text, the latter can be inferred to purely rely on the lateral growth, and take advantage of favorable growth condition at corners, to generate a series of new cubes along the body diagonal. However, that did not originate from equiaxed dendritic growth.

The dendrite tip radius, ρ, is a significant length scale in the context of dendritic growth. A simple relationship, $\rho = h^2/2d$, where h is the half width of dendrite at a distance of d behind the tip, can be used to measure ρ (Hürlimann et al., 1992). By plugging three different points on the contour of the left dendrite tip in figure 4.4c into the above relationship, the measured ρ is 2.62 µm, with a standard deviation of 0.04 µm. On the theoretical side, the marginal stability criterion can be used to estimate ρ. The estimated radius is 3.1 µm, slightly larger than the measured one, see section 4.4.5.2. Besides, according to the microscopic solvability theory, the dendrite tip's growth is oriented towards the directions where a surface stiffness minimum is obtained (Ben-Jacob, 1993; Saito, 1996). This requires that the curvature undercooling term, which can be rewritten as $\overline{\Delta T_r} = d(\theta - \theta_d)\kappa = d_0\{1 - \epsilon\cos[j(\theta - \theta_d)]\}\kappa$, where $d(\theta - \theta_d) = \tilde{\gamma}(\theta - \theta_d)T_m c_p/L^2$, $\tilde{\gamma}(\theta - \theta_d)$ the surface stiffness, T_m the melting point, c_p the specific heat, L the latent heat, d_0 the isotropic portion of $d(\theta - \theta_d)$, ϵ the strength of anisotropy, and j the number of symmetry, achieve its minima, i.e., θ is aligned with either θ_d or other equivalent values. Based on the preceding, the 2-D notation θ_d, in fact, represents <111> directions for dendritic proeutectic Al_3Sc in the 3-D space.

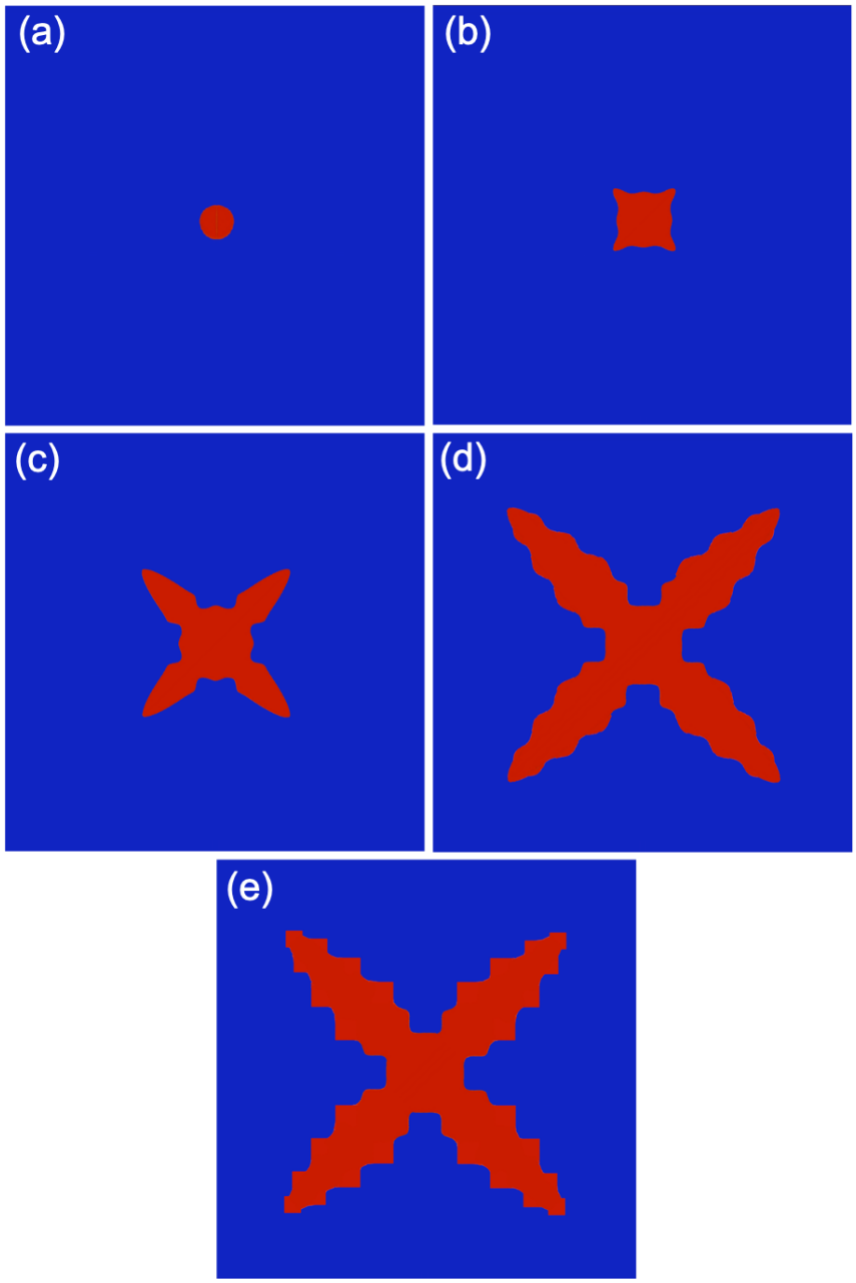

Figure 4.7 Schematics of a growing equiaxed dendritic Al_3Sc particle at the intermediate cooling rate. (a) The formation of the first spherical solid was followed by (b) the generation of infinitesimal perturbations, pointing to <111> directions, on the S/L front. Afterwards, (c) dendritic stems with a stable, paraboloidal tip evolved. With further growth, (d) eight dendrite stems with a stable, paraboloidal tip grew longer, and wave-like side branches decorated the sides of stems. When the driving force reduced to the lateral growth regime at a late stage of growth, (e) the dendrite tips and side branches ended up growing in a faceted manner, the steps on the dendrite stems are of {100} facets. Note, the above 2-D schematics use diagonal to represent <111> directions, and use vertical and horizontal directions to represent <100> directions.

4.4.4 Fast-cooled specimen

The proeutectic Al_3Sc exhibits irregular cross-sections in the fast-cooled specimen, figure 4.1c. A closer look shows that proeutectic Al_3Sc has a dual-density cross-sectional structure, figure 4.5a-c, as the central region has a stronger BSE signal than the outside. The outside branches were previously treated as dendrites by Norman and Tsakiropoulos (1991b), and Hyde et al. (2000). However, as mentioned in section 4.3.4, the highly branched structures lack dendrite's characteristics, but feature tip splitting and meandering growth. It is proposed that the outside highly branched structure should be seaweeds, rather than dendrites. The tendency of tip splitting of solutal seaweeds (the microstructural evolution mainly controlled by solute diffusion, as demonstrated in section 4.4.5.1) can be explained below, following the idea suggested by Ben-Jacob (1993) to explain the case of thermal seaweeds (purely controlled by thermal diffusion):

When advancing into the melt, the tip region transfers solute via the S/L interface. The liquid composition at the interface, c_l^*, analogues to the undercooling, is also mediated by the Gibbs-Thomson condition, by a relationship of $c_l^*/c_l^{eq} = 1 - d'(\theta - \theta_d)\kappa - \beta'(\theta - \theta_\beta)V$, where c_l^{eq} is the equilibrium liquid composition, and $d'(\theta - \theta_d)$ and $\beta'(\theta - \theta_\beta)$ are the rescaled capillarity length and kinetic coefficient, respectively, see (Provatas & Elder, 2010). The chemical potential of the liquid at the interface can be expressed as $\mu_l^* = \mu^{eq} + k_B T \ln(c_l^*/c_l^{eq})$ (Saito, 1996), and the uneven distribution of chemical potential, μ, drives the solute flux as $\partial c/\partial t = M\nabla^2\mu$, where μ^{eq} equilibrium chemical potential, k_B Boltzmann constant, T temperature, c composition, t time, and M solute mobility. The effect of anisotropy is to shift μ's extrema from the tip to its sides, e.g., somewhere the maximum product of $d'(\theta - \theta_d)\kappa$ can be achieved. The larger the anisotropy, the farther the extrema are away from the tip. If the anisotropy is not large enough (ϵ being small), the solute flux to μ's extrema can smooth out the uneven μ field in the vicinity of the tip, and eventually flatten and widen the tip to cause morphological instability. Namely, the tip will be vulnerable to splitting. A quantitative numerical study of solidification implies that ϵ for an IMC may take a value of 0.15 to 0.45, such that the dendrite-to-seaweed morphological transition at a large undercooling can be reproduced (Assadi et al., 2009). In addition, the fractal dimension, d_f, for the outside seaweeds is ~1.9 for the 2-D cross-section, which are thus identified as fractal seaweeds.

On the other side, the central region turns out to be more complex than what it was previously thought to be. It can clearly be seen from figure 4.5a, 4.5b, and 4.5d that the internal structure is of seaweed-typed textures rather than a simply solid core. Besides, the central area has a higher density than the outside, and nearly fills the entire space. It is proposed that the internal structure is also seaweed-typed, and to be more precise, it falls in the group of compact seaweed that has a d_f of two for the 2-D cross-section. Based on the above discussion, the growth model for the sponge particle is illustrated by the hypothetical cooling curve (orange) in figure 4.6, combined with schematic representations in figure 4.8. A large undercooling resulted from the high cooling rate, step ***a*** in figure 4.6. The earliest spherical solid formed, figure 4.8a, and soon became unstable once $R > R_c$. R_c, in this case, is estimated to be ~0.35 μm by the morphological stability analysis, see section 4.4.5.3. The tiny particles in figure 4.5e are treated as an early stage of seaweed growth. Although a sectioned tiny particle is barely seen in the present result, its size (~0.4 μm) should be just slightly larger than the actual R_c. Therefore, the estimated R_c agrees well with the actual R_c. Seen from the overall cuboidal shape, the tiny particle appears to have eight protrusions near each cubic vertex, figure 4.5e. This suggests that the destabilized spherical front bumped into eight <111> directions, figure 4.8b and step ***b*** in figure 4.6. Brener et al. (1992, 1996) have concluded that seaweed structures can exist in the presence of surface tension anisotropy, provided the undercooling is appropriately large. Their morphology diagram is reproduced in figure 4.9, where CS, FS, CD, and FD stand for compact seaweeds, fractal seaweeds, compact dendrites, and fractal dendrites, respectively. At the onset of crystal growth, the undercooling was large enough to generate compact seaweeds that constituted the internal structure of a sponge particle, figure 4.8c and step ***c*** in figure 4.6. As the growth proceeds, the released latent heat lowered the undercooling. When the undercooling crossed the border of CS and FS, as indicated by the arrow in figure 4.9, fractal seaweeds resulted, figure 4.8d and step ***d*** in figure 4.6. As a result, seaweed Al_3Sc particles with a dual-density cross-section were formed. In fact, the evidence of seaweed structures can be dated back to some earlier studies for Al_3TM (TM=Ti, Zr, Hf, and Sc). Just to name a few, figure 6a in (Norman & Tsakiropoulos, 1991b), figure 2 in (Nes & Billdal, 1977), and figure 3 in (Haugan et al., 1983). However, at the time of these studies, the seaweed-typed growth was not fully recognized. Moreover, porous structures can occasionally be seen in the central region, figure 4.5d, similar to recent findings for β'-Al_3Zr (Khvan et al., 2018) and Al_3(Sc,Hf) (Popova et al.,

2019). The EDX analysis in (Popova et al., 2019) showed that the pores are enriched in Al, suggesting that they were formed during solidification, not arising from etching away. The porous structures may further support the proposed seaweed growth model, since Tegze et al. (2011) using phase field crystal modelling demonstrated that the succession of branching can lead to the formation of pores, and the porosity phenomena occurs more frequently at a high growth rate.

It should be noted that the overall contour for a sponge particle is concave, previously thought to be an indication of equiaxed dendritic growth (Ben-Jacob, 1993). This seems contradictory to the presented seaweed growth. Nonetheless, the convex contour for seaweed particle can be understandable, when additionally taking into account the anisotropy in the interfacial attachment kinetics. As aforementioned, the kinetic undercooling, $\overline{\Delta T_k} = \beta(\theta - \theta_\beta)V$, comes into play when V becomes considerable. Similar to $d(\theta - \theta_d)\kappa$, $\beta(\theta - \theta_\beta)V$ encourages Al_3Sc to grow in a direction with a minimum barrier for atomic attachment, i.e., $\theta = \theta_\beta$, or other equivalent values. Based on the observation, the author tentatively believes that θ_β represents <111> directions, coincident with θ_d, although both accurate $d(\theta - \theta_d)$ and $\beta(\theta - \theta_\beta)$ values for Al_3Sc is not yet available in the literature.

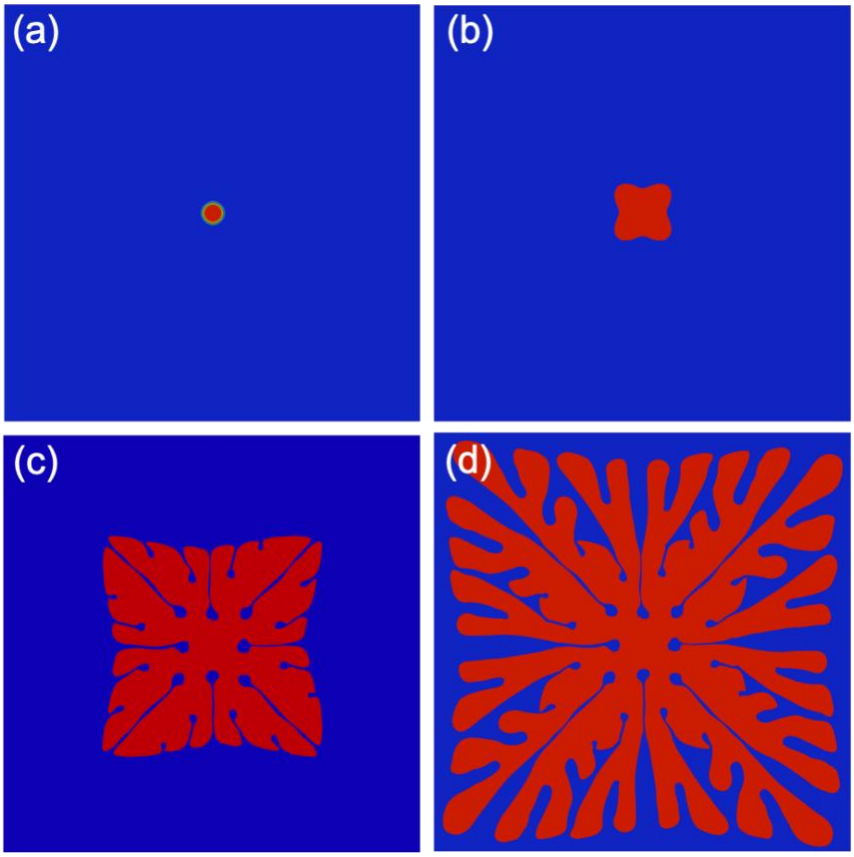

Figure 4.8 Schematics of a seaweed Al_3Sc particle at the fast cooling rate. (a) The formation of the first spherical solid was followed by (b) the generation of eight protrusions, pointing to near <111> directions, on the S/L front. Afterwards, (c) compact seaweeds with the fractal dimension, d_f, of two (on cross-section) filled up the space. When the undercooling reduced to cause a morphological transition from compact seaweed to fractal seaweed, (d) the fractal seaweeds with d_f of ~1.9 continued to grow outside of the compact seaweeds. Note, the above 2-D schematics use diagonal to represent <111> directions, as in figure 4.7.

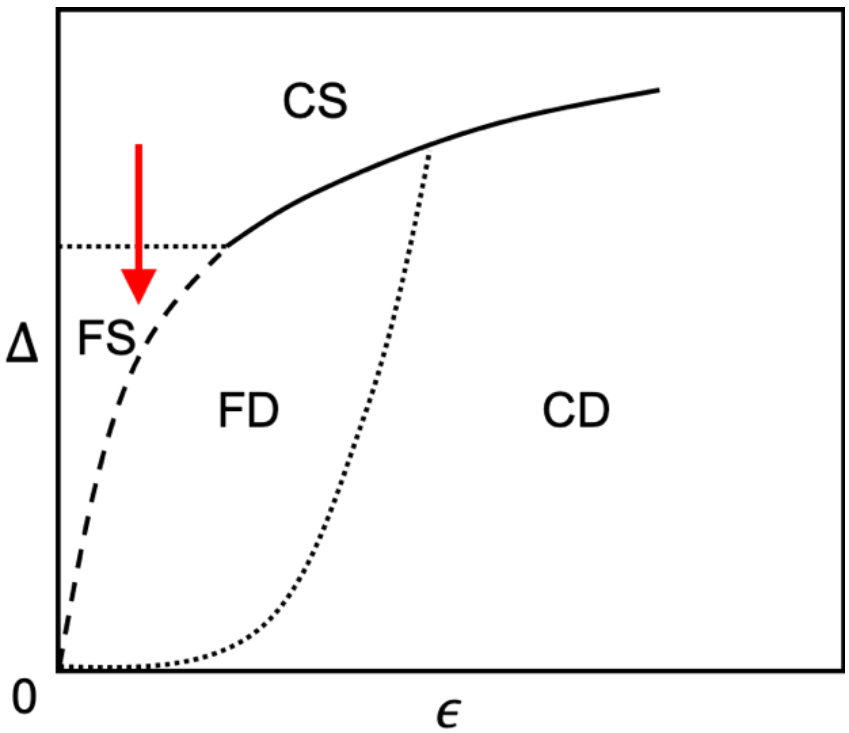

Figure 4.9 Morphology diagram. CS, FS, CD, and FD represent compact seaweeds, fractal seaweeds, compact dendrites, and fractal dendrites, respectively. The arrow indicates a possible pathway when the undercooling drops. Adapted from (Brener et al., 1996).

4.4.5 Characteristic length scales

In the preceding, the branched structures (dendritic or seaweed) formed, due to the need of more efficient transfer of solute and heat at the freezing front, at the expense of the increase in interfacial energy. The transfer behaviors are mainly limited within a diffusion boundary layer, characterized by the diffusion length (Glicksman, 2015). Thus, some characteristic length scales, such as the seaweed branch's interspacing, the dendrite tip radius, and the critical radius at the breakdown of a spherical front, are determined by the diffusion length to a large extent. The diffusion length is expressed as $l_{th} = D_{th}/V$ for the thermal diffusion, and $l_c = D/V$ for the solute diffusion, where D_{th} is the thermal diffusivity, and D is the solute diffusivity in liquid. Since D_{th} is usually three to four orders of magnitude larger than D, a natural hypothesis is that l_c predominantly modulates the characteristic length scales in the structure. The following is to use various morphological stability criteria to estimate relevant characteristic length scales to compare with their observed counterparts to verify the proposed growth models.

Table 4.1 Relevant thermo-physical parameters of Al_3Sc

Parameters	Values or derivation or comments	Refs.
Melting point, T_m	1593 K	(Shubin et al, 2008)
Latent heat, L_{Al3Sc}	67158 J·mol^{-1}	(Shubin et al, 2008)
Entropy of fusion, $\Delta S_{f,Al3Sc}$	$\Delta S_{f,Al3Sc} = L_{Al3Sc}/T_m = 42.2$ J·K^{-1}·mol^{-1}	
Roughness parameter, α	~5, since $\alpha = (\Delta S_{f,Al3Sc}/R_g)\, n_1/\nu$, where R_g is the gas constant, and n_1/ν can be regarded as an orientation factor, less than but close to unity.	(Hunt & Jackson, 1966)
Specific heat, $c_{p,Al3Sc}$	146.7 J·mol^{-1}·K^{-1}	(Shubin et al, 2008)
Estimated diffusivity in melt, D	Of the order of 10^{-9} m^2·s^{-1}, presumably comparable to other transition metals, such as Fe, Co, Ni, and Cu, in liquid Al.	(Chen et al., 2014; Du et al., 2003; Isono et al., 1996)
Estimated growth rate, V	~10^{-4} and 10^{-2} m·s^{-1} for the dendritic and seaweed growth, respectively. The lower growth rate is estimated by the fact that some other IMCs show a kinetic roughening transition at ~10^{-4} m·s^{-1}, whereas the higher one is suggested by the maximum growth rate (< 8 cm·s^{-1}) for β'-Al_3Zr. The choice of latter is justified in section 4.4.5.4.	(Kang et al., 2014; Srinivasan & Chattopadhyay, 2005; Xian et al., 2017)
Solute diffusion length, l_c	$l_c = D/V$, ~10^{-5} and ~10^{-7} m for the dendritic and seaweed growth, respectively.	
Gibbs-Thomson coefficient, Γ	~3 × 10^{-7} K·m, a typical estimate for IMCs in alloy melts.	(Li & Kuribayashi, 2003)
Constitutional undercooling, $m(c_\infty - c_l^*)$	16 K is for the dendritic growth, estimated by Eq. (A9.18) in (Kurz & Fisher, 1998). 20 K is for the seaweed growth, given 16 K being the lower limit, and freezing range being the upper limit, despite likely underestimated.	(Kurz & Fisher, 1998)

4.4.5.1 Estimation of the spacing between seaweeds

One of the significant characteristic length scales for seaweeds is the spacing between two neighboring branches, λ, see the inset in figure 4.5b. At the moment right before the tip splitting, the seaweed tip becomes widened and flattened (Utter et al., 2001). Thus, the tip splitting should

have the root in Mullins-Sekerka instability (Mullins & Sekerka, 1964) for a plane S/L interface, and λ is estimated to be the wavelength of perturbations (Chen et al., 2014; Utter et al., 2001):

$$\lambda \approx \sqrt{\frac{\Gamma/(1/2\pi)^2}{-\frac{G_l + G_s}{2} + mG_c\xi_c}} \tag{4.1}$$

where Γ is the Gibbs-Thomson coefficient, having the form of $\Gamma = \gamma/\Delta S_f$, γ the mean interface tension, ΔS_f the entropy of fusion, G_l the temperature gradient in liquid, written as $G_l = -(L/c_p)V/D_{th}$, G_s the temperature gradient in solid, usually considered to be zero in an undercooled melt (Trivedi & Kurz, 1994), m the liquidus slope, G_c the concentration gradient at the S/L interface on the liquid side, written as $G_c = (c_\infty - c_l^*)V/D$, c_∞ the melt composition, ξ_c known as solute stability function (Koseki & Flemings, 1995), expressed as $\xi_c = [V/2D + \sqrt{\left(\frac{V}{2D}\right)^2 + (2\pi/\lambda)^2} - V/D] \Big/ [V/2D + \sqrt{\left(\frac{V}{2D}\right)^2 + (2\pi/\lambda)^2} - (1-k)V/D]$, k the equilibrium partition coefficient. Al_3Sc is conventionally considered a stoichiometric IMC, although Norman et al. (1998) suggested that it has a limited solubility range of Sc content. Nonetheless, either case leads k to approach zero, and thus, ξ_c approaches unity. Consequently, the second term in the denominator in Eq. (4.1) is, now, written as $mG_c\xi_c \approx mG_c = m\,(c_\infty - c_l^*)V/D$, where $m(c_\infty - c_l^*)$ defines the constitutional undercooling. In the case of dendritic Al_3Sc, $m(c_\infty - c_l^*)$ is estimated to be 16 K, using Eq. (A9.18) in the (Kurz & Fisher, 1998) and parameters in the text. The 16 K, here, serves as the lower limit of the constitutional undercooling for seaweed Al_3Sc, assuming the seaweed growth needs a larger constitutional undercooling than dendritic growth. On the other side, the freezing range for Al-2 wt. % Sc melt, slightly over 100 K, acts as the upper limit. Tentatively, $m(c_\infty - c_l^*)$, in the seaweed growth case, is considered of the order of 20 K. Thus, when compared to the magnitude of the temperature gradient, i.e., $-G_l \approx (L_{Al3Sc}/c_{p,Al3Sc})V/D_{th}$, the term mG_c dominates the denominator at any V, and the temperature gradient term can be dropped for simplicity:

$$\lambda \approx \sqrt{\frac{\Gamma/(1/2\pi)^2}{mG_c}} = \sqrt{\frac{\Gamma/(1/2\pi)^2}{m(c_\infty - c_l^*)}\,l_c} \tag{4.2}$$

As expected, λ is primarily mediated by the solute diffusion length, l_c, by scaling with $l_c^{0.5}$. Plugging the relevant thermo-physical properties for Al_3Sc in table 4.1 into Eq. (4.2), λ is

estimated to be ~0.24 μm, slightly higher than the observed spacing of ~0.2 μm. The tip splitting mechanism due to the morphological instability also justifies the fine-scale structures in the seaweeds: Once a seaweed branch coarsens to a width slightly above λ, which allows two emerging protrusions a distance of λ away from one another, the flattened tip becomes unstable, and the tip splitting happens. After that, two newly-formed seaweed branches of a width of ~0.5λ advance into the melt while coarsening until the next tip splitting event, when the morphological instability criterion is satisfied again. As a consequence, the width of an individual seaweed branch is confined around λ at all times.

4.4.5.2 Estimation of the dendrite tip radius

The marginal stability criterion (MSC) can be applied to estimate the radius of steady-state dendrite tip, ρ, although little justification has been given (Trivedi & Kurz, 1994). In the spirit of MSC, the constant, $(1/2\pi)^2$, in Eqs. (4.1) and (4.2) is seen as a stability constant, σ^*, which can separately determine ρ and V for a moving dendrite tip (Kurz et al., 2019). However, experimentally measured stability constants for various materials are usually slightly smaller than $(1/2\pi)^2$ (Glicksman, 2015). The use of MSC desires a more practical value for σ^*. Given that the stability constant for Al_3Sc is not available in the literature, σ^* is tentatively taken to be 0.0195, which coincides with a famous dendritic solidification experiment (Huang & Glicksman, 1981), and yield Eq. (4.3). Plus, plugging V=10^{-4} m·s^{-1} into $l_c = D/V$, since some other IMCs exhibit kinetic roughening and develop into dendrites at a growth rate of ~10^{-4} m·s^{-1} (Kang et al., 2014; Li et al., 2020; Xian et al., 2017), while all other parameters kept unchanged, one obtains an estimated ρ of 3.1 μm, slightly larger than the observed radius of ~2.6 μm.

$$\rho \approx \sqrt{\frac{\Gamma/\sigma^*}{m(c_\infty - c_l^*)} l_c} \tag{4.3}$$

4.4.5.3 Estimation of the radius of destabilized sphere

Trivedi (1980) proposed a morphological stability criterion for a growing spherical solid in a binary alloy melt, which takes a form similar to Eq. (4.1), except for the corrections, $1/L(l)$ and $\zeta(l)$, as functions of the degree, l:

$$R_c \approx \sqrt{\frac{\Gamma/[1/L(l)]}{-G_l + mG_c\zeta(l)}} \tag{4.4}$$

where R_c is the critical radius at the onset of destabilization, and $L(l) \approx (2l+1)(l+2)$, $\zeta(l) = (2l+1)/[(l+1) + VR(k-1)/D]$. Al_3Sc equiaxed dendrites have eight primary stems, figure 4.4b and 4.4c, and an early-stage sponge particle seems to have eight protrusions, figure 4.5e. l=8 is plugged into $L(l)$ expression for both cases, yielding L=170. On the other hand, for the dendritic growth, VR is of the order of 10^{-10} $m^2 \cdot s^{-1}$, based on the above discussion, leading to $VR(k-1)/D$ ~-0.1, so ζ is 1.89. For the seaweed growth, VR is of the order of 10^{-9} $m^2 \cdot s^{-1}$, leading to $VR(k-1)/D$ ~-1, so ζ is 2.13. Again, $-G_l$ in Eq. (4.4) is ignored by the same token as discussed in section 4.4.5.1. Eventually, the radius, R_c, is estimated to be ~4.1 and ~0.35 μm for dendritic and seaweed growth, respectively, both estimates close to observations.

4.4.5.4 Remarks on results of morphological stability analyses

The above estimated characteristic length scales by morphological stability analyses are consistent with the experimental results, suggesting the rationality of dendritic and seaweed growth models for proeutectic Al_3Sc at intermediate and fast cooling rates, despite all overestimated somewhat. The overestimation should be due to the rough estimation for some parameters, e.g., the growth rates and the constitutional undercoolings may have been underestimated, whereas Gibbs-Thomson coefficient may have been overestimated. This calls for future precise measurement of Al_3Sc's thermo-physical parameters. Also, other types of discrepancies may arise from the applicability limitation of morphological stability criteria, such as the requirements of steady-state of growth, and small amplitude(linear regime) of perturbation.

Another main concern is the choice of growth velocities for dendrites and seaweeds, since the growth velocity was not either precisely controlled, or directly measured. The estimation of growth velocity for Al_3Sc dendrites should be reasonable, as stated in table 4.1, some other IMCs showing kinetic roughening at a comparable rate (Kang et al., 2014; Li et al., 2020; Xian et al., 2017). However, the choice of growth velocity for seaweed Al_3Sc appears disputable, since only one study that reported the maximum growth rate for Al_3Zr was cited in here (Srinivasan & Chattopadhyay, 2005). In fact, the critical radius for destabilized sphere, R_c, in section 4.4.5.3,

serves as a reference that reveals the relative difference in the order of magnitude in respective growth velocities. Using Eq. (4.4), the ratio of the critical radii for two types of growth can be estimated to be a prefactor times the square root of the inversed ratio of growth velocities, i.e., $R_{c,D}/R_{c,S} = prefactor \cdot \sqrt{V_S/V_D}$, where $R_{c,D}$ and $R_{c,S}$ are critical radii for dendritic and seaweed growth, respectively, the prefactor being ~1.2, which is a function of the constitutional undercooling and ζ, V_D and V_S the growth velocities for dendritic and seaweed growth, respectively. Since the observed $R_{c,D}$ is roughly an order of magnitude larger than the observed $R_{c,S}$, V_S is expected to be two orders of magnitude larger than V_D, justifying the current choice of V_S.

4.5 Conclusions

In summary, the present chapter mainly deals with the formation mechanism of proeutectic Al_3Sc formed in a slightly hypereutectic Al-2 wt. % Sc melt at three different cooling rates. At a slow cooling rate, cubic particles bounded by flat {100} facets are formed, whereby the minimum of total interfacial energy is achieved. At an intermediate cooling rate, an equiaxed dendritic growth prevails, featuring a well-defined backbone and a paraboloidal tip. The dendrite stems grow along eight <111> directions, governed by the minimum surface stiffness criterion. During a late stage of growth, the undercooling reduces to a low level, in which the lateral growth is favored, leading to faceting of side branches and the dendrite tip. At a high cooling rate, the surface tension anisotropy is not large enough to stabilize the tip of a solidifying front. As a result, the tip experiences a cascade of splitting, and the branches become serpentine. A striking finding is that the interior of an Al_3Sc particle consists mainly of compact seaweed structure that nearly fills the space. A low-magnification image for this may be deceptive, for it can easily be confused with a solid core, due to a high and constant density. A reduced undercooling subsequently leads to a transition from compact seaweed to fractal seaweed, giving rise to the presence of outside fractal seaweed structure. Despite the weakened effects of surface tension anisotropy, seaweed Al_3Sc particles exhibit preferential growth directions that are selected by the anisotropic attachment kinetics. Besides, the present chapter evaluates, on the basis of Mullins-Sekerka instability (Mullins & Sekerka, 1964), some characteristic length scales in the structure. Through the morphological stability criterion for an plane interface, the seaweed

branch's interspacing, as well as its width, can roughly be estimated, demonstrating that the fine scales for the structures on a sponge particle is attributed to the limited solute diffusivity of Sc in Al melt. Also, the morphological stability criteria for dendritic growth and spherical growth characterize the observed morphologies to a satisfactory degree. The success of applying these morphological stability criteria implies the correctness of the proposed dendritic and seaweed growth models for proeutectic Al_3Sc in an undercooled hypereutetic Al-Sc melt. As similar to some $L1_2$-structured Al_3TM (TM=Ti, Zr, and Hf) intermetallics, and even their ternary counterparts, the present chapter may also provide insights into growth mechanisms in these systems.

4.6 References

Assadi, H., Oghabi, M., & Herlach, D. M. (2009). Influence of ordering kinetics on dendritic growth morphology. *Acta Materialia, 57*(5), 1639-1647. https://doi.org/10.1016/j.actamat.2008.12.004

Ben-Jacob, E. (1993). From snowflake formation to growth of bacterial colonies. *Contemporary Physics, 34*(5), 247-273. https://doi.org/10.1080/00107519308222085

Ben-Jacob, E., Garik, P., Mueller, T., & Grier, D. (1988). Characterization of morphology transitions in diffusion-controlled systems. *Physical Review A, 38*(3), 1370-1380. https://doi.org/10.1103/PhysRevA.38.1370

Blake, N., & Hopkins, M. A. (1985). Constitution and age hardening of Al-Sc alloys. *Journal of Materials Science, 20*(8), 2861-2867. https://doi.org/10.1007/BF00553049

Brener, E., Müller-Krumbhaar, H., & Temkin, D. (1992). Kinetic Phase Diagram and Scaling Relations for Stationary Diffusional Growth. *Europhysics Letters, 17*(6), 535-540. https://doi.org/10.1209/0295-5075/17/6/010

Brener, E., Müller-Krumbhaar, H., & Temkin, D. (1996). Structure formation and the morphology diagram of possible structures in two-dimensional diffusional growth. *Physical Review E, 54*(3), 2714-2722. https://doi.org/10.1103/PhysRevE.54.2714

Brodova, I. G., Bashlikov, D. V., & Polents, I. V. (1998). Influence of Heat Time Melt Treatment on the Structure and the Properties of Rapidly Solidified Aluminum Alloys with Transition Metals. *Materials Science Forum, 269-272*, 589-594. https://doi.org/10.4028/www.scientific.net/msf.269-272.589

Cahn, J. W., Hillig, W. B., & Sears, G. W. (1964). The molecular mechanism of solidification. *Acta Metallurgica, 12*(12), 1421-1439. https://doi.org/10.1016/0001-6160(64)90130-0

Chen, Y., Billia, B., Li, D. Z., Nguyen-Thi, H., Xiao, N. M., & Bogno, A.-A.. (2014). Tip-splitting instability and transition to seaweed growth during alloy solidification in anisotropically preferred growth direction. *Acta Materialia, 66*, 219-231. https://doi.org/10.1016/j.actamat.2013.11.069

Chernov, A. A. (1974). Stability of faceted shapes. *Journal of Crystal Growth, 24-25*, 11-31. https://doi.org/10.1016/0022-0248(74)90277-2

Chu, M. G. (1994). Microstructure and solidification analysis of melt-spun Al-Ti and Al-Ti-B alloys. *Materials Science & Engineering A, 179-180*, 669-675. https://doi.org/10.1016/0921-5093(94)90290-9

Dorin, T., Ramajayam, M., Vahid, A., & Langan, T. (2018). Aluminium scandium alloys. In: R. Lumley (Ed.), *Fundamentals of Aluminium Metallurgy: Recent Advances* (pp. 439-494). Woodhead Publishing. https://doi.org/10.1016/B978-0-08-102063-0.00012-6

Du, Y., Chang, Y. A, Huang, B., Gong, W., Jin, Z., Xu, H., Yuan, Z., Liu, Y., He, Y., & Xie, F.-Y. (2003). Diffusion coefficients of some solutes in fcc and liquid Al: Critical evaluation and correlation. *Materials Science & Engineering A, 363*(1-2), 140-151. https://doi.org/10.1016/S0921-5093(03)00624-5

Gibbs, J. W. (1878). On the equilibrium of heterogeneous substances. *American Journal of Science, 16*(96), 441-458. https://doi.org/10.11588/heidok.00013220

Glicksman, M. E. (2015). 16 – Dendritic growth. In: T. Nishinaga (Ed.), *Handbook of Crystal Growth: Fundamentals* (2nd ed., pp. 669–722). Elsevier Inc. https://doi.org/10.1016/B978-0-444-56369-9.00016-2

Haugan, T, Nes, E., & Ryum, N. (1983). Precipitation reactions in Al-Zr-alloys. *MRS Online Proceedings Library Archive, 21*, 495-499. https://doi.org/10.1557/PROC-21-495

Hori, S., Tai, H., & Narita, Y. (1985). MICROSTRUCTURES OF RAPIDLY SOLIDIFIED Al-Ti ALLOYS CONTAINING TITANIUM UP TO 40% AND ITS THERMAL STABILITY. In S. Steeb & H. Warlimont (Eds.), *Rapidly Quenched Metals* (pp. 911-914). North Holland. https://doi.org/10.1016/B978-0-444-86939-5.50217-7

Huang, S.-C, & Glicksman, M. E. (1981). Overview 12: Fundamentals of dendritic solidification—I. Steady-state tip growth. *Acta Metallurgica, 29*(5), 701-715. https://doi.org/10.1016/0001-6160(81)90115-2

Hunt, J. D., & Jackson, K. A. (1966). Binary eutectic solidification, *Transactions of the Metallurgical Society of AIME, 236*(6), 843-852.

Hürlimann, E., Trittibach, R., Bisang, U., & Bilgram, J. H. (1992). Integral parameters of xenon dendrites. *Physical Review A, 46*(10), 6579-6595. https://doi.org/10.1103/PhysRevA.46.6579

Hyde, K. B., Norman, A. F., & Prangnell, P. B. (2000). The growth morphology and nucleation mechanism of primary L12Al3Sc particles in Al-Sc alloys. *Materials Science Forum, 331-337*, 1013-1018. https://doi.org/10.4028/www.scientific.net/MSF.331-337.1013

Hyde, K. B., Norman, A. F., & Prangnell, P. B. (2001). The effect of cooling rate on the morphology of primary Al3Sc intermetallic particles in Al-Sc alloys. *Acta Materialia, 49*(8), 1327-1337. https://doi.org/10.1016/S1359-6454(01)00050-7

Isono, N., Smith, P. M., Turnbull, D., & Aziz, M. J. (1996). Anomalous diffusion of Fe in Liquid AI Measured by the pulsed laser technique. *Metallurgical and Materials Transactions A, 27*(3), 725-730. https://doi.org/10.1007/BF02648959

Kang, H., Wang, T., Li, X., Su, Y., Guo, J., & Fu, H. (2014). Faceted–nonfaceted growth transition and 3-D morphological evolution of primary Al6Mn microcrystals in directionally solidified Al–3 at.% Mn alloy. *Journal of Materials Research, 29*(11), 1256-1263. https://doi.org/10.1557/jmr.2014.111

Khvan, A. V., Eskin, D. G., Starodub, K. F., Dinsdale, A. T., Wang, F., Fang, C., Cheverikin, V. V., & Gorshenkov, M. V. (2018). New insights into solidification and phase equilibria in the Al-Al3Zr system: Theoretical and experimental investigations. *Journal of Alloys and Compounds, 743*, 626-638. https://doi.org/10.1016/j.jallcom.2018.02.023

Koseki, T., & Flemings, M. C. (1995). Effect of External Heat Extraction on Dendritic Growth into Undercooled Melts. *ISIJ International, 35*(6), 611-617. https://doi.org/10.2355/isijinternational.35.611

Kurz, W., & Fisher, D. (1998). *Fundamentals of Solidification* (4th rev. ed.). Trans Tech Publications, Uetikon-Zuerich.

Kurz, W., Fisher, D. J., & Trivedi, R. (2019). Progress in modelling solidification microstructures in metals and alloys: Dendrites and cells from 1700 to 2000. *International Materials Reviews, 64*(6), 311-354. https://doi.org/10.1080/09506608.2018.1537090

Li, M., & Kuribayashi, K. (2003). Nucleation-controlled microstructures and anomalous eutectic formation in undercooled Co-Sn and Ni-Si eutectic melts. *Metallurgical and Materials Transactions A, 34*(12), 2999-3008. https://doi.org/10.1007/s11661-003-0199-5

Li, X., Wang, J., Hou, L., Gagnoud, A., & Fautrelle, Y. (2020). Studying on the morphology of primary phase by 3D-CT technology and controlling eutectic growth by tailoring the primary phase. *Journal of Alloys and Compounds, 821*, 153457. https://doi.org/10.1016/j.jallcom.2019.153457

Liu, L., Li, J. F., & Zhou, Y. H. (2011). Solidification interface morphology pattern in the undercooled Co–24.0 at.% Sn eutectic melt. *Acta Materialia, 59*(14), 5558-5567. https://doi.org/10.1016/j.actamat.2011.05.028

Liu, X., Liu, Y., Huang, D., Han, Q., & Wang, X. (2017). Tailoring in-situ TiB2 particulates in aluminum matrix composites. *Materials Science & Engineering A, 705*, 55-61. https://doi.org/10.1016/j.msea.2017.08.047

Mullins, W. W, & Sekerka, R. F. (1964). Stability of a Planar Interface During Solidification of a Dilute Binary Alloy. *Journal of Applied Physics, 35*(2), 444-451. https://doi.org/10.1063/1.1713333

Nes, E., & Billdal, H. (1977). Non-equilibrium solidification of hyperperitetic Al-Zr alloys. *Acta Metallurgica, 25*(9), 1031-1037. https://doi.org/10.1016/0001-6160(77)90132-8

Norman, A. F., Prangnell, P. B., & McEwen, R. S. (1998). The solidification behaviour of dilute aluminium–scandium alloys. *Acta Materialia, 46*(16), 5715-5732. https://doi.org/10.1016/S1359-6454(98)00257-2

Norman, A. F., & Tsakiropoulos, P. (1991a). The microstructure and properties of rapidly solidified Al-Hf alloys. *Materials Science & Engineering A, 134*, 1234-1237. https://doi.org/10.1016/0921-5093(91)90963-N

Norman, A. F., & Tsakiropoulos, P. (1991b). Rapid solidification of Al-Hf alloys - solidification microstructures and decomposition of solid-solutions, *International Journal of Rapid Solidification, 6*(3-4), 185-213.

Ohashi, T., & Ichikawa, R. (1972). A new metastable phase in rapidly solidified Al-Zr alloys. *Metallurgical Transactions, 3*(8), 2300-2302. https://doi.org/10.1007/BF02643251

Perepezko, J. H., & Hildal, K. (2006). Analysis of solidification microstructures during wedge-casting. *Philosophical Magazine, 86*(24), 3681-3701. https://doi.org/10.1080/14786430500404116

Peteves, S. D., & Abbaschian, R. (1991). Growth kinetics of solid-liquid Ga interfaces: part II. Theoretical. *Metallurgical Transactions A, 22*(6), 1271-1286. https://doi.org/10.1007/BF02660659

Popova, E., Kotenkov, P., Shubin, A., & Gilev, I. (2020). Formation of Metastable Aluminides in Al–Sc–Ti (Zr, Hf) Cast Alloys. *Metals and Materials International, 26*(10), 1515-1523. https://doi.org/10.1007/s12540-019-00397-x

Popova, E. A., Kotenkov, P. V., Shubin, A. B., & Pastukhov, E. A. (2017). Structural Features of Al–Hf–Sc Master Alloys. *Russian Journal of Non-ferrous Metals, 58*(6), 639-643. https://doi.org/10.3103/S1067821217060086

Popova, E. A., Shubin, A. B., Kotenkov, P. V., Pastukhov, E. A., Bodrova, L. E., & Fedorova, O. M. (2012). Al-Ti-Zr master alloys: Structure formation. *Russian Metallurgy Metally, 2012*(5), 357-361. https://doi.org/10.1134/S0036029512050126

Provatas, N., & Elder, K. (2010). *Phase-Field Methods in Materials Science and Engineering*. Wiley-VCH. https://doi.org/10.1002/9783527631520

Saito, Y. (1996). *Statistical Physics of Crystal Growth*. World Scientific. https://doi.org/10.1142/3261

Shubin, A. B., Shunyaev, K. Y., & Kulikova, T. V. (2008). Problem of the thermodynamic properties of liquid aluminum alloys with scandium. *Russian Metallurgy Metally, 2008*(5), 364-369. https://doi.org/10.1134/S0036029508050029

Singh, V., Prasad, K. S., & Gokhale, A. A. (2002). Solidification structure of aluminium with trace additions of Sc and Zr. *International Journal of Cast Metals Research, 14*(5), 287-291. https://doi.org/10.1080/13640461.2002.11819446

Srinivasan, D., & Chattopadhyay, K. (2005). Non-equilibrium transformations involving L12-Al3Zr in ternary Al-X-Zr alloys. *Metallurgical and Materials Transactions A, 36*(2), 311-320. https://doi.org/10.1007/s11661-005-0304-z

Tegze, G., Tóth, G. I, & Gránásy, L. (2011). Faceting and branching in 2D crystal growth. *Physical Review Letters, 106*(19), 195502. https://doi.org/10.1103/PhysRevLett.106.195502

Trivedi, R. (1980). Morphological stability of a solid particle growing from a binary alloy melt. *Journal of Crystal Growth, 48*(1), 93-99. https://doi.org/10.1016/0022-0248(80)90197-9

Trivedi, R., & Kurz, W. (1994). Dendritic growth. *International Materials Reviews, 39*(2), 49-74. https://doi.org/10.1179/imr.1994.39.2.49

Utter, B., Ragnarsson, R., & Bodenschatz, E. (2001). Alternating tip splitting in directional solidification. *Physical Review Letters, 86*(20), 4604-4607. https://doi.org/10.1103/PhysRevLett.86.4604

Wulff, G. (1901). XXV. Zur Frage Der Geschwindigkeit Des Wachsthums Und Der Auflösung Der Krystallflächen. *Zeitschrift Für Kristallographie - Crystalline Materials, 34*(1-6), 449–530. https://doi.org/10.1524/zkri.1901.34.1.449

Xian, J. W., Belyakov, S. A., Ollivier, M., Nogita, K., Yasuda, H., & Gourlay, C. M. (2017). Cu6Sn5 crystal growth mechanisms during solidification of electronic interconnections. *Acta Materialia, 126*, 540-551. https://doi.org/10.1016/j.actamat.2016.12.043

CHAPTER 5. THE ROD EUTECTIC GROWTH OF AL-AL_3SC IN A HYPEREUTECTIC AL-2 WT. % SC UNDERCOOLED MELT

5.1 Introduction

The solidification of eutectic alloys is of great scientific and engineering importance, thanks to their peculiar features, such as lower melting points compared to the individual eutectic components, the possibility of assembling in-situ composite materials, and potentially controllable fine scale (sub-micro scale or even nano scale) microstructure (Glicksman, 2011; Kurz & Fisher, 1979). In many contexts, e.g., the fields of casting and welding, the microstructure in eutectics and the formation mechanism thereof attract enormous attention, because the microstructure greatly influences the mechanical properties. Nonetheless, among numerous microstructural investigations into a variety of eutectics, the Al-Al_3Sc eutectic system seems to have been overlooked for decades. To the author's best knowledge, the eutectic solidification behavior in this system has scarcely been studied in detail according to the open literature (at least in those written in English), and the relevant metallographic information is extremely lacking.

Initially, Al_3Sc was thought to be in equilibrium with the solid solution α-Al peritectically at 665 ºC (Naumkin et al., 1965). However, it is acknowledged widely that the involved reaction is of a eutectic type in the Al-Al_3Sc system, later on (Dorin et al., 2018; Eskin, 2018; Røyset & Ryum, 2005; Toropova, 1998). A very recent Al-Sc phase diagram (Dorin et al., 2018) is shown in figure 5.1a. The Al-rich corner is enlarged in figure 5.1b, in which the invariant eutectic point is at ~659 ºC and ~0.5 wt. % Sc, and the maximum solid solubility of Sc in α-Al is 0.33 wt. % Sc at the eutectic temperature (Dorin et al., 2018). Clearly, the phase diagram of Al-Al_3Sc eutectic system owns an extremely asymmetric form. In addition, the Sc content in a hypereutectic Al-Sc alloy seldom exceeds 2 wt. %. The latter leads to a four-fold feature in the volume fraction for different constituents in a final product, according to the lever rule: (1) the proeutectic Al_3Sc phase constitutes merely a few per cent of volume, whereas (2) the Al-Al_3Sc eutectic composes the remaining majority; in the eutectic, (3) the eutectic α-Al phase dominates (> 99 vol. %), while (4) the eutectic Al_3Sc phase only makes up less than 1 vol. %.

In addition to the earlier misinterpretation of phase diagram type, existing viewpoints regarding the Al-Al_3Sc eutectic formation diverge. Tomus et al. (2010) reported a lamellar

structure for the Al-Al_3Sc eutectic produced by both steel mold casting and electron beam processing, but their study was not focused on the eutectic formation, and did not provide further information about it. Brodova et al. (1998) suggested that the morphology of the Al-Al_3Sc eutectic is a function of both the melt overheat (with respect to the liquidus temperature) and the cooling rate. At a given mildly high overheat (< 400 ºC), they suggested that a needle-typed eutectic structure would transition to a globular type if a critical cooling rate is passed (ranging from ~100 to ~2000 $ºC \cdot s^{-1}$ as the overheat decreases). However, these two structures are not shown in the original work. Besides, with a higher overheat (> 400 ºC) and a faster cooling rate (> 10^4 $ºC \cdot s^{-1}$) concurrently, they described that the eutectic Al_3Sc phase has a "degenerated divided" form, and is indistinguishable from the proeutectic Al_3Sc phase in the same casting. Norman et al. (1998) proposed a divorced eutectic growth for the Al-Al_3Sc system. They believed that the difficulty in a coupled growth results from a combined effect of the negligible volume fraction of the eutectic Al_3Sc, a sluggish growth kinetics of the intermetallic compound (Al_3Sc), and an excellent heterogeneous nucleation efficiency of α-Al on the proeutectic Al_3Sc phase (the last one only applicable to hypereutectic alloys). Consequently, following the completion of proeutectic Al_3Sc phase formation, a single-phase growth of the decoupled eutectic α-Al phase prevails in the grain, while the decoupled eutectic Al_3Sc phase forms at the final stage, eventually siting in the grain boundaries.

In an attempt to uncover the "mysterious" eutectic growth in the Al-Al_3Sc system, the present chapter first utilized optical and electron microscopy to examine how did the Al-Al_3Sc eutectic respond to various solidification conditions, and subsequently, quantitatively analyzed some key problems, including the eutectic growth kinetics, the interface undercooling required to form an entire eutectic structure, and the morphological selection for the eutectic Al_3Sc phase.

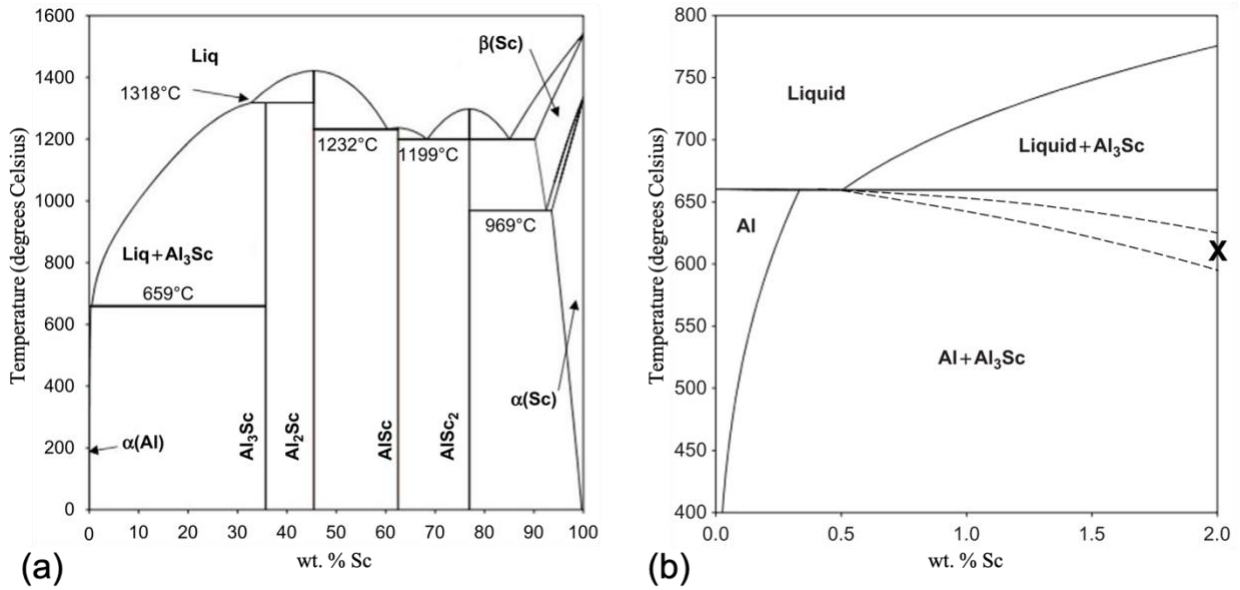

Figure 5.1 (a) The Al-Sc phase diagram. (b) The Al-rich corner in (a). The cross symbol in (b) represents a condition at which the entire eutectic growth can be achieved, see section 5.4.1, and the two dashed curves encompass a hypothetical coupled zone. Adapted from "Aluminium scandium alloys," by T. Dorin, M. Ramajayam, A. Vahid, and T. Langan, *2018*, in: R. Lumley (Ed.), *Fundamentals of Aluminium Metallurgy: Recent Advances*, p. 446, Woodhead Publishing, (https://doi.org/10.1016/B978-0-08-102063-0.00012-6). Copyright 2018 by Elsevier Ltd. Reprinted with permission.

5.2 Experimental

All the studied specimens were prepared from as-received hypereutectic Al-2 wt. % Sc master alloy, melted in an electric resistance furnace, and held at 1010 ºC for two hours to guarantee the thorough dissolution of preexisting intermetallic compound prior to cooling.

To explore how the Al-Al_3Sc eutectic responds to different cooling rates, two cooling strategies were exploited, designated as slow cooling and fast cooling in the text. As to the slow cooling, after removal from the furnace, the molten alloy was air-cooled to the room temperature while staying in a high alumina crucible. The estimated cooling rate is on the order of 1 $ºC \cdot s^{-1}$. As to the fasting cooling, the molten alloy was cast into an air-cooled wedge-shaped copper mold. In fact, the wedge casting provides a spectrum of fast cooling rates, and the cooling rate depends on the distance between the measured spot and the mold wall (Norman & Tsakiropoulos, 1991). Considering that in the present chapter, the area of interest is off the midline of wedge ingot, the author modifies the cooling rate approximation equation, Eq. (4) in

the reference (Norman & Tsakiropoulos, 1991), or see Eq. (3.1) in the Chapter three, by replacing the half thickness in the original equation with the distance between the area of interest and the ingot edge, l. Thus, the estimated cooling rate, $\dot{T}$, is expressed as $\dot{T} \approx h_0(T - T_0)/lc_p$, in which h_0 is the heat transfer coefficient, roughly 4×10^3 W·m^{-2}·K^{-1} (Norman & Tsakiropoulos, 1991), T the melt temperature, for simplicity, taken as the pouring temperature of 1010 ºC, T_0 the room temperature 25 ºC, and c_p the volumetric specific heat, see Table 5.1.

The metallographic specimens were acquired by sectioning in half for the slow-cooled ingot, and sectioning along the mid-plane (parallel to the *xz*-plane defined in the reference; Perepezko & Hildal, 2006) for the fast-cooled wedge casting. All the metallographic specimens were subjected to the conventional treatments for grinding, polishing, and etching. Furthermore, one half of the slow-cooled specimen was additionally deeply etched with a solution of 250 ml methanol containing 10 g iodine and 25 g tartaric acid for one hour to properly erode α-Al matrix. Meanwhile, a transmission electron microscopy (TEM) foil with dimensions of 20 μm × 10 μm × 0.1 μm was cut by focused ion beam at an interface between an α-Al matrix and a proeutectic Al_3Sc particle in the other half of the slow-cooled specimen that did not undergo deep etching. Microstructural examination was performed on Zeiss Axioscope 7 optical microscope, FEI 3D Quanta dual beam scanning electron microscope (SEM), FEI Nova NanoSEM, and FEI Titan 80-300 TEM. The energy dispersive X-ray (EDX) analyses were conducted on FEI Nova NanoSEM at 10 kV and FEI Titan 80-300 TEM at 200 kV. Both secondary electron (SE) and back-scattered electron (BSE) modes were utilized on SEM.

The eutectic interphase spacing, λ, is a significant and measurable variable for the eutectic growth. However, the intrinsic difficulty in identifying the eutectic spacing is unavoidably encountered in the present chapter. This is because both exploited cooling methods offer the unconstrained growth (Kurz & Fisher, 1998) in undercooled melts, and the solidification condition is expected to vary constantly, even though the variation can be mild in the slow-cooled melt. Therefore, the eutectic spacing can be inhomogeneous from spot to spot. To overcome this inhomogeneity, the eutectic spacing will be estimated across a region with an area of 25 to 100 μm^2. When possible, this practice is repeated in multiple regions, and afterwards, the average is taken. Besides, for the rod eutectic present in this chapter, despite irregularities, a hexagonal packing pattern is assumed, which is a typical form (Jackson & Hunt, 1966; Teng et al., 2008; Trivedi & Wang, 2012). With the hexagonal packing pattern, each rod nominally

occupies an area of $0.867\lambda^2$. Hence, for a region of an area A, in which n eutectic rods roughly grow normal to the region, the eutectic spacing is estimated as $\lambda = \sqrt{A/0.867n}$. Moreover, assuming each rod with a unified diameter d, the volume fraction of rods, f, is given by $f = \pi n d^2/4A$.

5.3 Results

5.3.1 Al-Al_3Sc eutectic growth under the rapid cooling condition

5.3.1.1 Overview of an area near the edge of wedge ingot

Figure 5.2 shows an optical microscopic image of an area near the tip of the wedge ingot, as indicated by the schematic drawing. The field of view covers the midline (top) to an edge (bottom) of the wedge casting. Evidently, three different regions in this area are distinguishable by their distinct microstructures, with their rough borderlines pointed out by the bold dashed lines on the right-hand side. The upper region (designated as Region A), near the midline of the wedge casting, is consisted of equiaxed refined grains, and a second phase is clearly present in the center of most of the grains. The middle region (Region B) is composed of much larger grains, and these grains seem to have a form of early-stage equiaxed dendrites. The lower region (Region C) appears featureless in structure, similar to "zone A" (Jones, 1969) or segregation-free zone (Cantor et al., 1991) in the literature, which is less responsive to etching. To disclose a sense of the effect of fast cooling rates, $\dot{T}$ is estimated for the two borderlines. The distances from the upper and the lower borderline to the edge are $l = 1500$ and 450 μm, respectively. Plugging these two l's into the approximation equation introduced in Experimental section, $\dot{T} \approx$ 900 and 3000 $^{o}C \cdot s^{-1}$ for the two demarcations.

The distinct microstructures suggest different solidification pathways, which are discussed in the following sections.

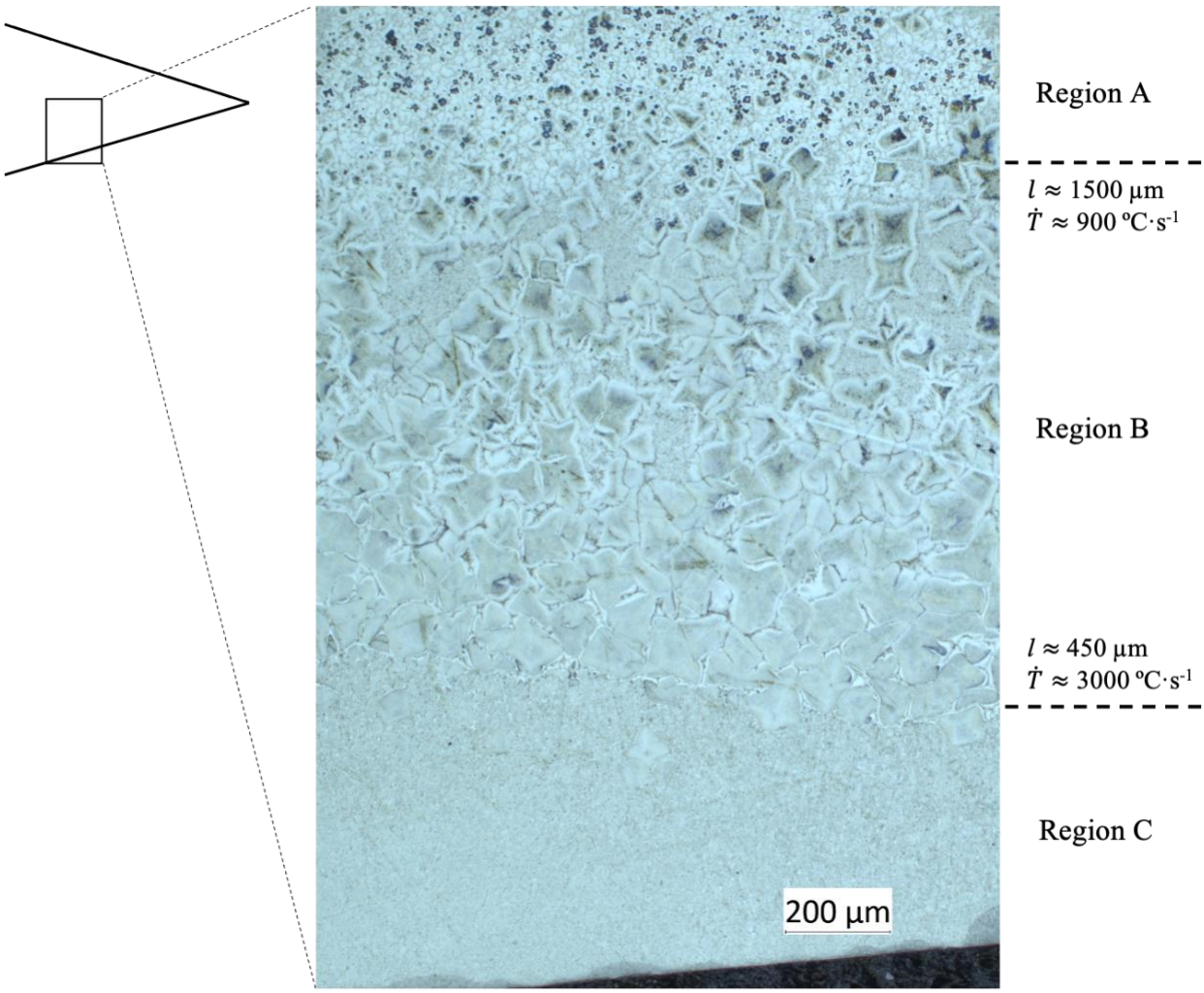

Figure 5.2 An optical micrograph showing an overview of an area near the tip and an edge of the fast-cooled wedge ingot, indicated by the schematic drawing. Three different regions can be distinguished by their distinct microstructures.

5.3.1.2 Region A: the region for proeutectic Al_3Sc phase plus Al-Al_3Sc rod eutectic

SEM images in figure 5.3 reveal further details in Region A. In a representative area, figure 5.3a, several proeutectic Al_3Sc particles are present, and the identity is confirmed by the accompanying EDX elemental mappings. In brief, the high cooling rate in this region imposed a large driving force for the growth of proeutectic Al_3Sc phase, which was able to destabilize an otherwise paraboloidal solid/liquid (S/L) interface. Consequently, constant tip splitting of the S/L interface resulted, and seaweed-structured Al_3Sc was generated. This point has been detailed in the last chapter, and will not be elaborated here.

It is worth noting that the rest of the space is occupied by numerous fine-scale Al_3Sc fibers. figure 5.3b shows an enlarged view of these fibers. Unlike the seaweed-structured proeutectic Al_3Sc, these Al_3Sc fibers did not experience overwhelming tip splitting. In addition, the fibers are dispersed in the α-Al matrix homogeneously enough, such that outside the area taken by the proeutectic Al_3Sc, no obvious solute micro-segregation is resolvable by the EDX analysis. Furthermore, the low ratio of the fiber's diameter to the interfibrous spacing suggests a small volume fraction of the Al_3Sc fibers. Thus, the author is convinced that the formation of these fibers arose from a eutectic growth of α-Al and Al_3Sc. With a limited volume fraction, the minor eutectic phase is prone to a rod-like morphology (Liu et al., 2011). Additionally, the eutectic Al_3Sc fibers display a non-faceted characteristic, forming a regular eutectic with the eutectic α-Al phase (the α-Al matrix).

Figure 5.3 The main microstructural features in Region A. (a) An SEM-SE image and the corresponding EDX elemental mappings showing that Region A is comprised of the seaweed-structured proeutectic Al_3Sc and the Al-Al_3Sc rod eutectic. (b) A close-up SEM-BSE image of non-faceted fibrous eutectic Al_3Sc phase.

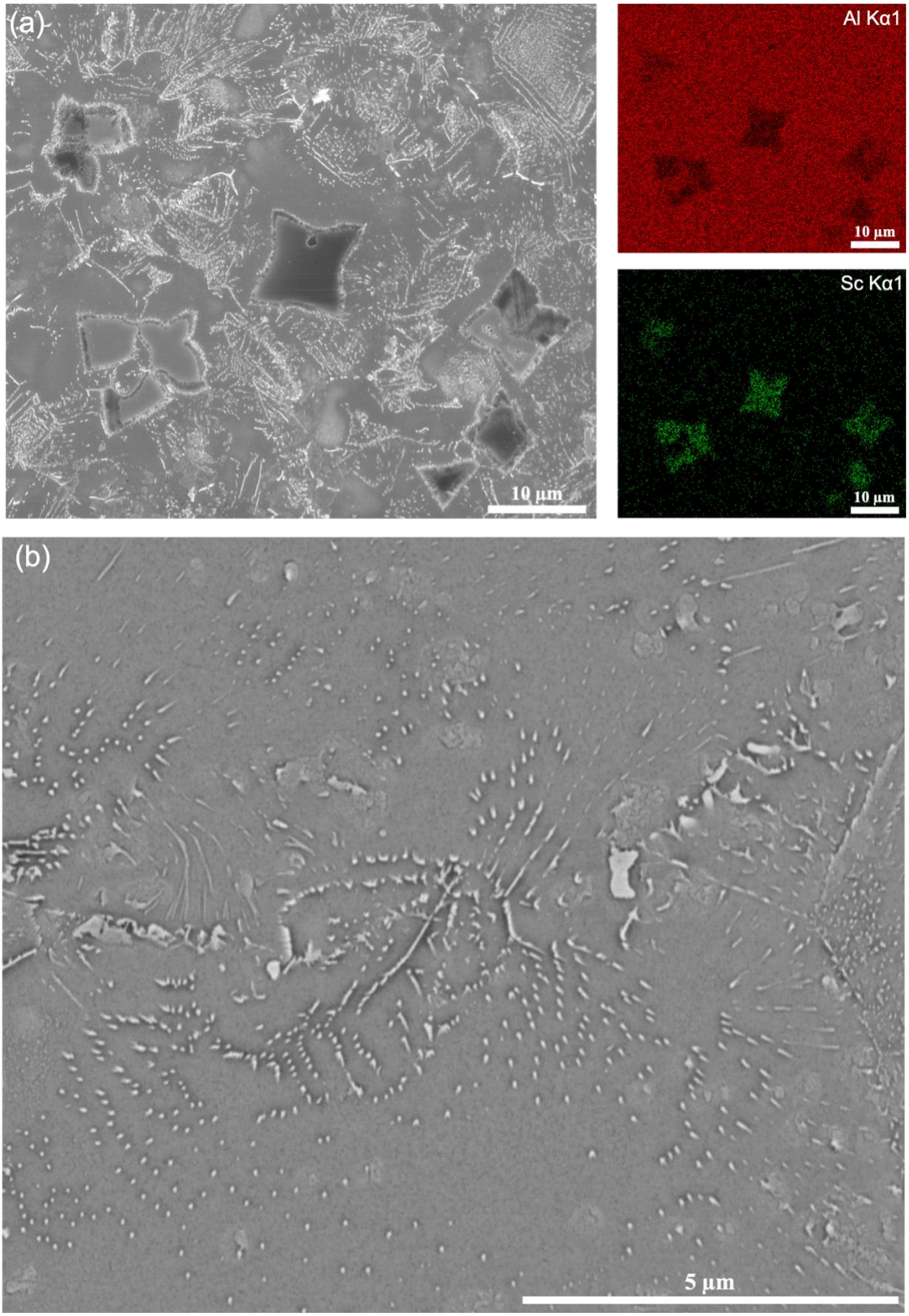
(a)
10 µm
Al Kα1
10 µm
Sc Kα1
10 µm
(b)
5 µm

5.3.1.3 Region B: the region for entire Al-Al_3Sc rod eutectic

In Region B, faster cooling region, two principal characteristics are discernible: (1) a large grain size (~100 µm) compared to that in Region A, and (2) an early-stage equiaxed dendritic form for most of the grains. Figure 5.4a shows an SEM-SE image and its corresponding EDX elemental mappings for a representative area. According to EDX analysis, Sc constitutes 2.06 mass per cent, close to the nominal composition. Similarly, no apparent micro-segregation of Sc is found throughout Region B. This observation leads to an interpretation that Region B is entirely composed of eutectic structure, and each grain is composed of so-called 'eutectic dendrites' (Goetzinger et al., 1998; Li & Zhou, 2005). In fact, the large grain size, itself, supports these grains originating from a eutectic solidification, rather than a single-phase formation. If in Region B, the solidification started with the formation of proeutectic Al_3Sc, as in Region A, aided with a faster cooling rate, or in other words, a larger undercooling prior to nucleation, Region B should have had more Al_3Sc nuclei than Region A, due to an enhanced nucleation rate. Then, Region B should have had a greater number of grains than those in Region A, or at least, a comparable number if the grain refining effect of Al_3Sc was already saturated, but not the reverse. Nonetheless, the situation becomes consistent if a eutectic solidification was proceeding in Region B. As suggested by the classical nucleation theory, the nucleation of eutectic is an interacting process, in which one eutectic phase nucleates first from the melt, followed by the other heterogeneously nucleating on the former (Elliott, 1983). These two conjugate events would prolong the completion time of nucleation, thus, remarkably reducing the nucleation rate and the number of grains.

The formation of entire eutectic structure requires that the solidification condition be within the 'coupled zone' (Kurz & Fisher, 1979). This is probable, although the alloy composition (2.0 wt. % Sc) largely exceeds the equilibrium eutectic composition (~0.5 wt. % Sc), because in a eutectic system consisted of a metallic phase (α-Al) and an intermetallic compound (Al_3Sc), the coupled zone is likely to skew towards the intermetallic compound side (Kurz & Fisher, 1979). Such a hypothetical coupled zone is plotted by the dashed curves in figure 5.1b, which encloses the current growth condition for the eutectic dendrites (labelled 'x'), derived by the quantitative assessment in section 5.4.1.

A high-magnification image of a paraboloidal eutectic dendrite tip is shown in figure 5.4b, which advances from the bottom right to the top left corner. This close look, in conjunction with figure 5.4a, compares two length scales in the eutectic dendrites. On one hand, the overall contour of a grain is predominantly controlled by thermal diffusion, due to the need of dissipating the released latent heat from the crystallized solid to the undercooled liquid (Goetzinger et al., 1998; Li & Zhou, 2005). On the other hand, the grain's internal structure is governed by eutectic growth, relying on the localized counter-diffusion mass fluxes along the S/L interface (Goetzinger et al., 1998; Li & Zhou, 2005). As a result, the dimension of the eutectic dendrite tip covers a number of interfibrous spacings, as the thermal diffusivity is much larger than the solute diffusivity (Glicksman, 2011).

In fact, the eutectic Al_3Sc fibers presented in figure 5.4b share some similarities with the seaweed branches in the single-phase growth of proeutectic Al_3Sc, see figure 5.4a or figure 4.5b, such as the fine-scale fibrous morphology and the branching behavior. Therefore, it is essential to point out some fundamental differences between them, in order to avoid confusions. Firstly, the extensive branching behavior is an intrinsic characteristic in seaweed-typed growth, as the forefront S/L interface is unsteady during progressing in an undercooled melt, and subject to tip splitting. Nevertheless, branching does not necessarily occur to a regular eutectic. Branching may occur when a changing environment necessitates the adjustment of eutectic spacing (Teng et al., 2008). However, since the eutectic dendrite tip with a form of a paraboloid of revolution, figure 5.4b, can be viewed as a relatively stable growth state (Glicksman, 2011), the change in kinetics of the tip of eutectic dendrites is presumably less intense. Thus, the eutectic Al_3Sc fibers behind the tip should be less frequently interfered with the branching. Secondly, the seaweed branches in the single-phase growth of proeutectic Al_3Sc is more compact than the eutectic Al_3Sc fibers. This is understandable, since the latter is the minor eutectic phase, with an expected wide interfibrous spacing relative to the fiber's width. In fact, the actual packing density of the eutectic Al_3Sc fibers is not as dense as they appear in figure 5.4b. The deceptive impression is because of the inclination of the fibers with respect to the cross-section. Figure 5.4c shows a portion of eutectic dendrites, where the central fibers grow roughly normal to the cross-section, and reflect the real packing density. According to the approximation method introduced in the Experimental section, the eutectic spacing and the Al_3Sc fiber's volume fraction are estimated from the central part in figure 5.4c to be 0.3 μm and 9 vol. %, respectively.

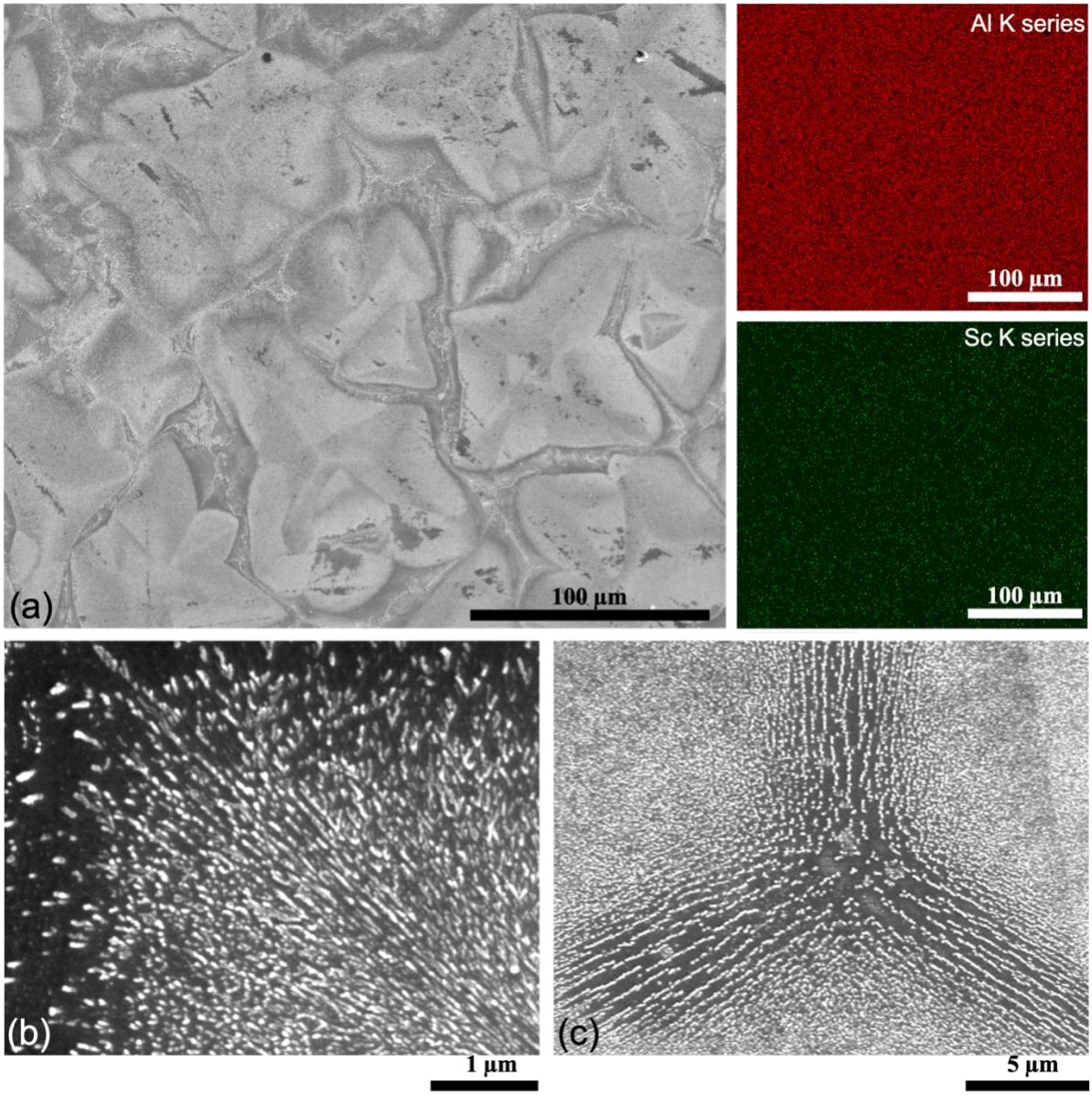

Figure 5.4 The main microstructural features in Region B. (a) An SEM-SE image showing grains of eutectic dendrites, and the corresponding elemental mappings revealing a quite homogeneous distribution of both elements. (b) A paraboloidal tip of eutectic dendrites running from the bottom right to the top left corner. (c) Perpendicularly growing eutectic Al_3Sc fibers (center) disclosing the actual packing density of themselves.

Additionally, in figure 5.4a, some gaps between the grain boundaries and the contour of eutectic dendrites are discernible. These gaps are postulated to be related to a divorced eutectic growth of α-Al and Al_5FeSi starting at a lower temperature of 584 ºC (Terzi et al., 2010) in the

last residual melt. As a result, α-Al composes the gaps, while Al_5FeSi remains in the grain boundaries. Figure 5.5 shows an SEM-BSE image of Al_5FeSi, and the corresponding elemental mappings.

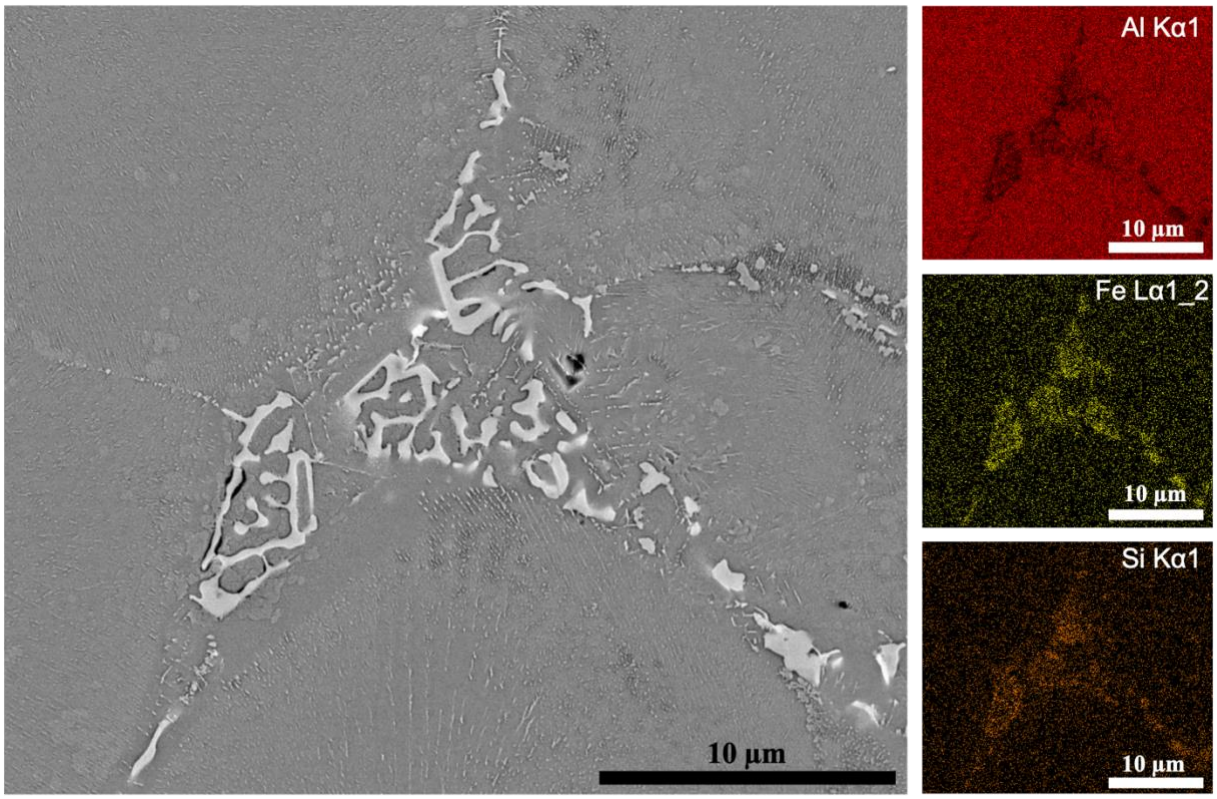

Figure 5.5 An SEM-BSE image and elemental mappings of Al_5FeSi, which resides in the grain boundaries of eutectic dendrites, and probably results from a divorced eutectic growth with α-Al in the last stage of casting.

5.3.1.4 Region C: the region for proeutectic α-Al phase plus Al-Al_3Sc rod eutectic

Figure 5.6a shows an area in Region C adjacent to Region B. A small number of eutectic dendrites are dispersed accidently in Region C. Analogous to Region B, Region C has an overall Sc content of ~2.0 wt. % and homogeneous distributions of both Al and Sc. A closer look, Figure 5.6b and 5.6c, reveals that contrary to the first impression of a featureless structure, Region C is composed of tiny globular grains (~5 µm) with fine structures. But this should not be surprising, since the cooling rate, somehow faster than 3000 $^{o}C \cdot s^{-1}$, may not be high enough to achieve a true segregation-free solidification, which is realized usually by splatting (Jones, 1969), melt spinning (Cantor, 1991), or other techniques with further higher cooling rates ($\dot{T} > 10^4$ $^{o}C \cdot s^{-1}$).

The tiny grains, in general, exhibit a hollow in the center, whereas the outer part is comprised of fibrous structures radiating from the periphery of the hollow. These fibrous structures resemble those in the eutectic dendrites. Given these observations, it is suggested that the rapid cooling rate achieved in Region C brought the condition below the coupled zone, and the solidification commenced with the formation of proeutectic α-Al phase. Before the globular S/L interface of the α-Al phase started to destabilize, the changes in composition and temperature moved the condition into the coupled zone, and the proeutectic α-Al phase somehow facilitated the nucleation of eutectic. Thus, the Al-Al_3Sc eutectic grew on the proeutectic α-Al core in a radial manner. In this sense, the number of resultant duplex-structured grains was largely determined by the number of proeutectic α-Al nuclei. The copious nucleation events of proeutectic α-Al led to the impingement of the grains earlier than they had a chance to become morphologically unstable. Unlike the paraboloidal tip of eutectic dendrites, the spherical interface of the duplex-structured grain was continuously expanding. This would have caused a continued widening of eutectic spacing, if no new eutectic branches were generated (Wang et al., 2011). Thus, the eutectic Al_3Sc fibers in the duplex-structured grains experienced a more frequent branching activity, as shown in figure 5.6b and 5.6c, compared to those behind the tip of eutectic dendrites.

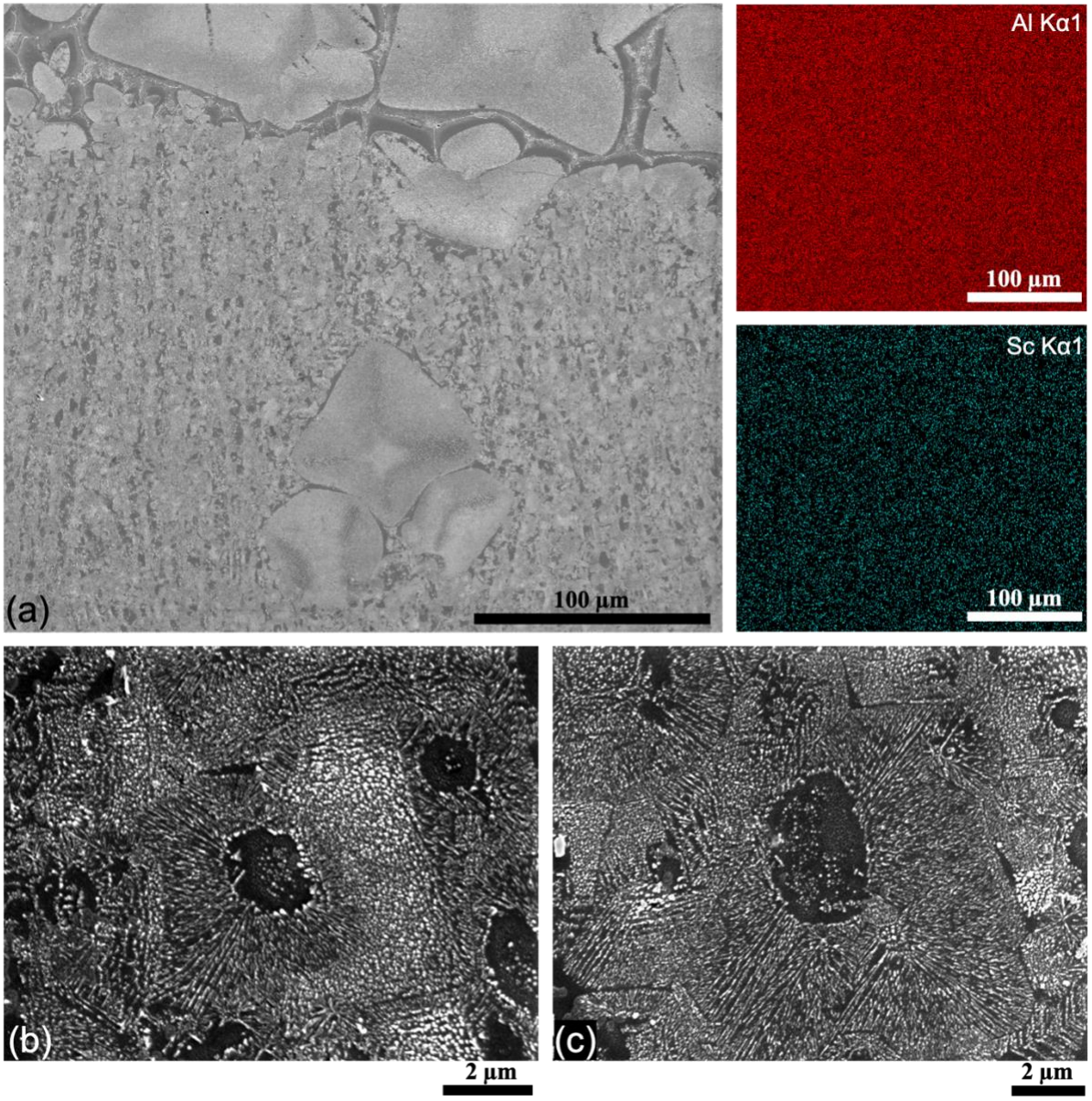

Figure 5.6 The main microstructural features in Region C. (a) An SEM-SE image and the corresponding elemental mappings of an area in Region C next to Region B (top). (b,c) The fine-scale grains in Region C composed of an inner α-Al core and an outer Al-Al_3Sc eutectic ring

5.3.2 Al-Al_3Sc eutectic growth under slow cooling

A transient state of the Al-Al_3Sc eutectic growth was reported without an interpretation in the last chapter. This section presents the interpretations. Figure 5.7a shows a high-angle annular dark field (HAADF) image of the interface between a proeutectic Al_3Sc particle (right) and the surrounding α-Al matrix (left). A dense array of Al_3Sc fibers grew epitaxially on the surface of a

proeutectic Al_3Sc particle, with a parallel orientation relationship with the α-Al phase, which is confirmed by an elemental mapping, figure 5.7b, and the selected area diffraction (SAD) patterns, figure 5.7c. Figure 5.7d and 5.7e further disclose that the array of eutectic Al_3Sc fibers grew perpendicular to the {100} facets of the proeutectic Al_3Sc cube, and the fibers have a non-faceted characteristic. It needs to be pointed out that a eutectic growth should be the only reasonable interpretation for the origin of these Al_3Sc fibers. Any alternative interpretation would be an abrupt kinetic roughening phenomenon occurring to a flat interface of proeutectic Al_3Sc. However, the kinetic roughening is known to require a high undercooling for a highly anisotropic intermetallic compound. Thus, this prerequisite can hardly be met in a slow-cooled melt, especially in a late growth stage, when recalescence effect inevitably plays a role.

The proeutectic Al_3Sc with {100} facets acted as an excellent substrate for the epitaxial growth of eutectic Al_3Sc fibers. The latter was initiated independently and excessively on the substrate in such a way that the volume fraction of the eutectic Al_3Sc fibers within the layer where they exist reaches 30-40 vol. %, noticeably exceeding the equilibrium amount (~1 vol. %). As a result, this transient state of Al-Al_3Sc eutectic growth could only persist for a short distance range of ~1 μm, i.e., the length of Al_3Sc fibers, due to the exhaustion of Sc in the growth front. Afterwards, a single-phase growth of α-Al followed until the melt recovered from the solute depletion, and then, the diffusion coupled eutectic growth of Al-Al_3Sc resumed. The arrows in figure 5.7a, 5.7b, and 5.7d indicate examples of newly nucleated eutectic Al_3Sc fibers. Unlike the kinetically favorable transient state, the regenerated Al-Al_3Sc eutectic grew in a more thermodynamically favorable manner. Figure 5.7f displays such regenerated rod eutectic, which grew freely appearing almost everywhere in the grain. Besides, the inspection of several areas (not shown), where the eutectic Al_3Sc fibers grew roughly perpendicular to the cross-section, suggests that the eutectic Al_3Sc fibers have a volume fraction of ~1 vol. %, and a eutectic spacing of ~1.1 μm.

Figure 5.7 The Al-Al_3Sc eutectic growth in the slow-cooled specimen. (a) An HAADF image, (b) the corresponding elemental mapping, (c) the SAD patterns, (d) a low- and (e) a high-magnification SEM-SE images of a transient eutectic growth that is confined to the proeutectic Al_3Sc particle's {100} facets. (f) An SEM-SE image of the freely grown eutectic. The arrows in (a,b,d) indicate the regeneration of the rod eutectic at some distance away from the proeutectic Al_3Sc interface.

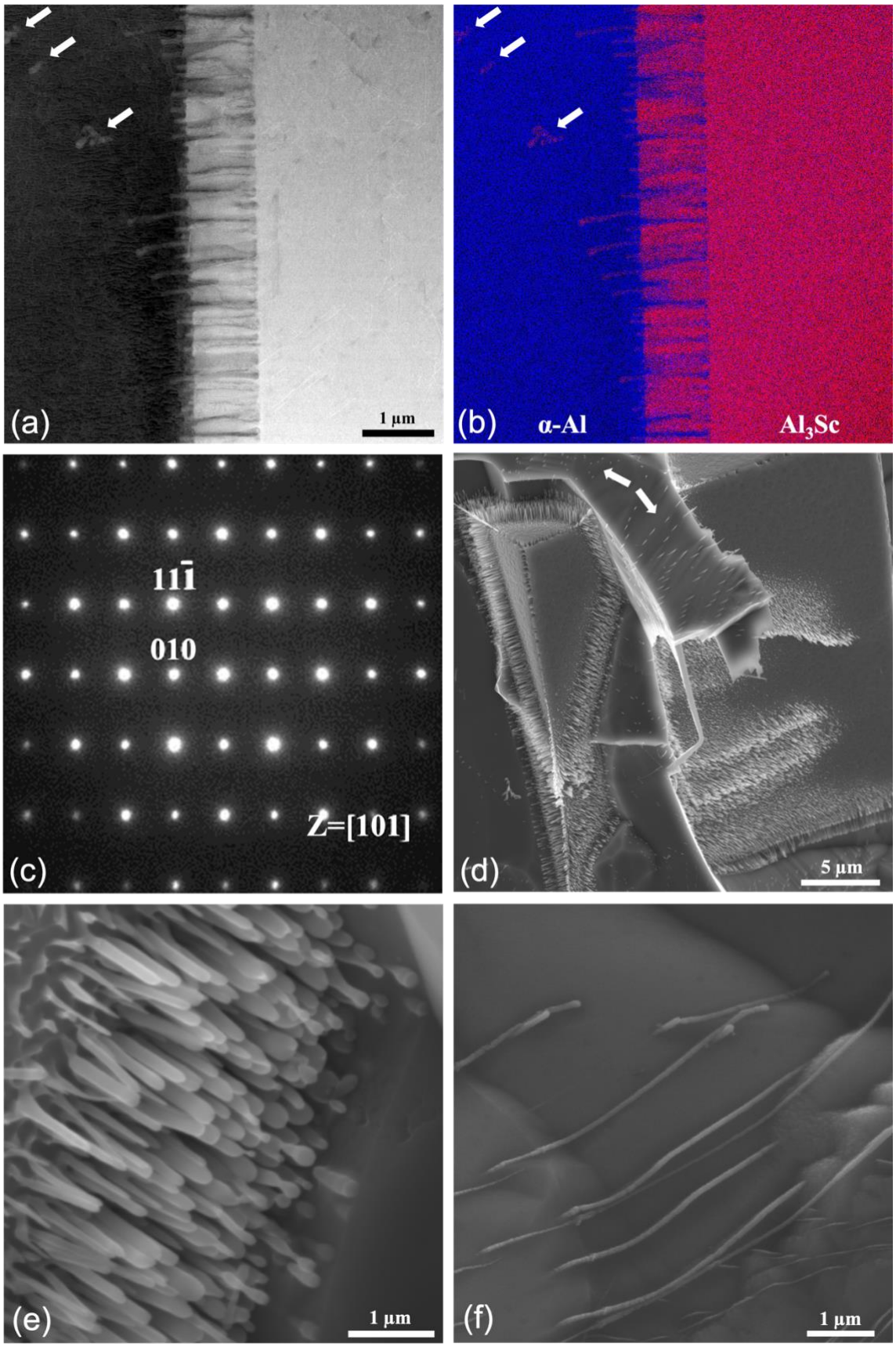
(a)
1 µm
(b)
α-Al
Al_3Sc
$11\bar{1}$
010
Z=[101]
(c)
(d)
5 µm
(e)
1 µm
(f)
1 µm

5.4 Discussion

5.4.1 Assessment of growth condition for the eutectic dendrites

A basic assumption in analytical solutions to eutectic growth is the establishment of a steady-state (Jackson & Hunt, 1966; Kurz & Trivedi, 1991; Li & Zhou, 2005; Trivedi et al., 1987; Trivedi & Wang, 2012). This makes the following quantitative assessment restricted to the steady-state eutectic growth. As can be seen in the previous sections, it is assumed that the eutectic growth in Region A and C proceeds with an expanding spherical S/L interface, since the grain structure in these two regions is totally nucleation-controlled, and the grains are in a roughly globular form. There is no solid ground to assume that the eutectic growing in Region A or C was at a steady-state. In comparison, the paraboloidal tip of the eutectic dendrites in Region B has the possibility of growing at a steady-state (Kurz et al., 2019). Therefore, among the three different growth situations in the wedge ingot, the eutectic dendrites should be the most appropriate to be assessed.

Similar to the reference (Li & Zhou, 2005), the present chapter treats the overall contour of eutectic dendrites as being thermally controlled, while treating the internal structure as a rapidly solidified rod eutectic with a planar front, where the theory by Trivedi and Wang (2012) is applicable. Assuming that the operating condition of the contour of eutectic dendrites is governed by the marginal stability, the correlation between the growth rate, V, and the dendrite tip's radius, ρ, can be expressed as the following equation (Li & Zhou, 2005):

$$\rho = \frac{\Gamma/\sigma^*}{\frac{L}{c_p} P_t [1 - \frac{1}{\sqrt{1 + 1/(\sigma^* P_t^2)}}]} \tag{5.1}$$

where Γ is the effective Gibbs-Thomson coefficient, which is the weighted average of the two eutectic phases, σ^* the stability constant, L the latent heat, c_p the specific heat, P_t the thermal Peclet number, expressed as $P_t = V\rho/2a$, a the thermal diffusion coefficient. The values of the parameters used for the evaluation are given in Table 5.1. The average dendrite tip's radius is estimated from seven eutectic dendrite tips in Region B. Using an approximation relationship (Hürlimann et al., 1992), $\rho = h^2/2d$, in which h is the half width of dendrite trunk at a distance of d behind the tip, $\rho = 6.4 \pm 2.1$ µm. Substituting $\rho = 6.4$ µm into Eq. (5.1), using a graphic method to find the root, one obtains $V = 0.035$ m·s^{-1}. This growth rate is much slower than a

typical diffusive velocity V_D, which can be larger than a few meters per second (Boettinger & Coriell, 1986; Hoglund et al., 1991). Consequently, the effect of solute trapping is not considered, and nor is the dependence of the distribution coefficients and the liquidus slopes on the growth rate. Namely, the equilibrium values for the distribution coefficients and the liquidus slopes are used. Furthermore, the thermal undercooling in front of the eutectic dendrite tip is written as $\Delta T_t = \frac{L}{c_p} P_t \exp\,(P_t) E_1(P_t)$, where E_1 is the exponential integral function, and the product of the last three terms is, in fact, the Ivantsov function (Li & Zhou, 2005). Then, ΔT_t turns out to be 6.4 ºC for the eutectic dendrites. Additionally, the undercooling to maintain the eutectic dendrite tip's curvature is comparatively negligible (~0.06 ºC).

Next, before assessing the internal eutectic growth quantitatively, the sub-group of Al-Al_3Sc phase diagram needs to be clarified. This is because commonly seen analytic solutions for rapid eutectic growth, including the one used in the text, primarily deal with two sub-groups of phase diagrams (Kurz & Trivedi, 1991; Li & Zhou, 2005; Trivedi et al., 1987; Trivedi & Wang, 2012), one with parallel liquidus and solidus metastable extensions for each eutectic phase, the other with an equal distribution coefficient for both eutectic phases. It is suggested that the Al-Al_3Sc system can be categorized into the first sub-group, which is also known as the cigar model. From the general trends of the liquidus and solidus lines for α-Al, see figure 5.1b, it is not surprising that the "parallel liquidus and solidus metastable extensions" scenario is satisfied. However, on the Al_3Sc side, the use of cigar model needs some justification. As shown in figure 5.1a, although the liquidus line for Al_3Sc varies with the composition, it converges sharply to the pure Al end as the temperature reduces below the eutectic temperature, and nearly goes vertically. Thus, the metastable liquidus and solidus lines for Al_3Sc are also considered roughly parallel.

According to a conventional classification of eutectic types (Hunt & Jackson, 1966; Stefanescu, 2015), with both eutectic phases being non-faceted, the eutectic system falls into the category of regular eutectic. The regular eutectics include lamellar and rod eutectics. As to the Al-Al_3Sc eutectic system, the α-Al phase is well-known to be a non-faceted phase, and interestingly, the Al_3Sc phase also shows a non-faceted as well as rod-like morphology under both circumstances (fast and slow cooling). Therefore, the Al-Al_3Sc eutectic is classified as a regular eutectic. In essence, this classification not only distinguishes non-faceting from faceting, but also, more importantly, reflects different growth mechanisms between regular and irregular

eutectics. For regular eutectics, the operating growth point at the extremum condition is usually assumed, in which the sum of the constitutional undercooling, ΔT_c, and the curvature undercooling, ΔT_r, reaches its minimum (Jackson & Hunt, 1966; Kurz & Trivedi, 1991; Li & Zhou, 2005; Trivedi et al., 1987; Trivedi & Wang, 2012; Wei et al., 2015). The minimum sum is written as follows, when considering the effects of high growth rates (the growth rate is incorporated into the eutectic Peclet number, p_e) (Trivedi & Wang, 2012):

$$\Delta T_c + \Delta T_r = m_{eff} K_1 [p_e P(1 + F)] \tag{5.2}$$

where m_{eff} is the effective liquidus slope, expressed as $m_{eff} = m_\alpha m_\beta / (m_\alpha + m_\beta)$, m_α and m_β the liquidus slopes for the two eutectic phases (both defined positive), for simplicity, the subscripts α and β denoting the eutectic α-Al phase and the eutectic Al_3Sc phase, respectively, K_1 a material property constant, defined as $K_1 = 4(\Delta C_\alpha + \Delta C_\beta)/f_\alpha$, ΔC_α, ΔC_β the differences in liquid and solid compositions at the liquid/α-Al and the liquid/Al_3Sc interfaces, respectively, f_α the volume fraction of the α-Al matrix, p_e expressed as $p_e = \frac{V\lambda}{2D}$, D the impurity diffusion coefficient, and P, F defined as function P and function F, respectively, detailed in the reference (Trivedi & Wang, 2012). Due to the lack of available data for the diffusion coefficient of Sc in the liquid Al, the author estimates it based on the data for other metallic elements in the same period (Period 4). Most of them reside near 3×10^{-9} $m^2 \cdot s^{-1}$ (Pearce, 2016), and this value is considered a reasonable estimate for D used in this chapter. P and F are functions of p_e. The variations in P, F, and $(\Delta T_c + \Delta T_r)$ with p_e are plotted in figure 5.8a, 5.8b and 5.8c, respectively. The rod eutectic shares the same growth rate with the tip of eutectic dendrites, i.e., $V = 0.035$ $m \cdot s^{-1}$. Accordingly, $p_e = 1.73$, $P = 0.033$, $F = 0.821$, and $(\Delta T_c + \Delta T_r) = 47.7$ ºC.

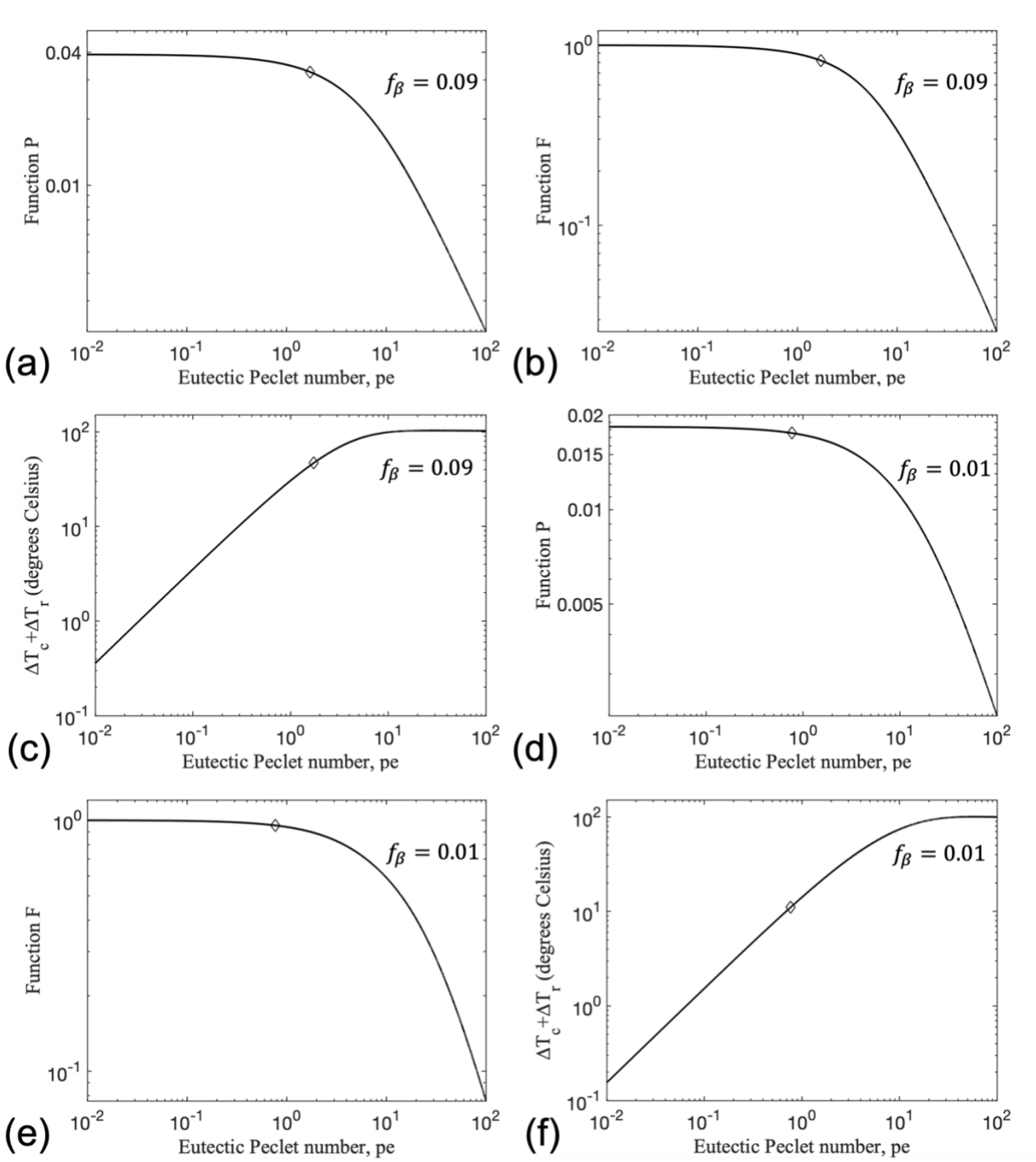

Figure 5.8 Variations in P, F, and $(\Delta T_c + \Delta T_r)$ with p_e. (a,b,c) The upper row for the eutectic dendrites produced by the fast cooling, where the volume fraction of the eutectic Al_3Sc fibers $f_\beta = 0.09$. (d,e,f) The lower row for the eutectic growth under the slow cooling condition, where $f_\beta = 0.01$.

Apart from the constitutional and curvature undercoolings, another major component in the interface undercooling is the kinetic undercooling, which would become notable when the

growth rate is fast, and/or the system contains intermetallic compound phase(s). For the eutectic system crystallizing with an isothermal S/L interface, the total kinetic undercooling is expressed as (Li & Zhou, 2005; Trivedi & Wang, 2012):

$$\Delta T_k = m_{eff}\left(\frac{\Delta T_k^{\alpha}}{m_{\alpha}} + \frac{\Delta T_k^{\beta}}{m_{\beta}}\right) \tag{5.3}$$

where ΔT_k^{α}, ΔT_k^{β} are the kinetic undercoolings for α-Al and Al_3Sc, respectively. For the metallic solid solution, α-Al, a linear kinetic law is conventionally assumed (Trivedi & Wang, 2012), giving $\Delta T_k^{\alpha} = V/\mu_{\alpha}$, μ_{α} the linear kinetic coefficient for α-Al, tentatively taking a typical value of 1.5 $s \cdot m^{-1} \cdot K^{-1}$ (Li & Kuribayashi, 2003). For the intermetallic compound, Al_3Sc, given the fact that Al_3Sc exposes non-faceted interfaces, the linear kinetic law is assumed too, i.e., $\Delta T_k^{\beta} = V/\mu_{\beta}$. Nonetheless, due to the complex superlattice structure, the linear kinetic coefficient μ_{β} tentatively takes a sluggish value of 0.0015 $m \cdot s^{-1} \cdot K^{-1}$, which is typical for intermetallic compounds (Li & Kuribayashi, 2003). Surprisingly, Eq. (5.3) yields a low kinetic undercooling of 0.5 ºC. Even allowing for an uncertainty range of an order of magnitude for both μ_{α} and μ_{β}, the kinetic undercooling will not change the interface undercooling by over 10 %.

Including the approximated kinetic undercooling of 0.5 ºC, the interface undercooling for the eutectic dendrites growing in the rapidly-solidified melt reaches 48.2 ºC. This sole data point, despite far from enough to plot the complete coupled zone, should be sufficient to indicate a general direction along which a narrow coupled zone might extend. The coupled zone being narrow at the composition of 2 wt. % Sc can be inferred from the stringent condition that allows for the formation of eutectic dendrites. That is, only within a narrow strip (Region B), ~1 mm in the width, can the eutectic dendrites form, and also, the span of the cooling rates across this region does not exceed an order of magnitude. The derived growth condition point is denoted by a cross symbol in figure 5.1b, which is encompassed by a hypothetical narrow coupled zone. Nonetheless, one should be cautious about the derivation of this interface undercooling and aware of the limits of the unconstrainted growth method. The situation was simplified by using the averaged variables (ρ and λ) and the variable derived from one of them (V). However, since the coupled zone should contain a range of conditions, these variables are barely fixed. Ideally, from the place near Region A to the place near Region C, i.e., with an increasing cooling rate, both the measurable variables ρ and λ decrease, while the derivable variable V increases.

Unfortunately, the solidification method used in the chapter, to some degree, permitted grain's movement during growing, and prevents convenient dimension measurements (the random orientation of grains).

Table 5.1 Relevant physical parameters for the eutectic dendrites

Parameters	Values or derivations	Refs.
Effective Gibbs-Thomson coefficient[a], Γ	2×10^{-7} K·m	(Li & Kuribayashi, 2003)
Stability constant, σ^*	0.0253	(Li & Zhou, 2005)
Latent heat[b], L	1.047×10^{9} J·m^{-3}	(Gale & Totemeier, 2004)
Specific heat[c], c_p	2.93×10^{6} J·m^{-3}·K^{-1}	(Gale & Totemeier, 2004)
Thermal conductivity for molten alloy[c], κ	95 W·m^{-1}·K^{-1}	(Gale & Totemeier, 2004)
Thermal diffusivity for molten alloy[c], a	$a = \kappa/c_p = 3.2 \times 10^{-5}$ m^2·s^{-1}	
Liquidus slope of eutectic α-Al phase, m_α	3 ºC·wt. %$^{-1}$	(Dorin et al., 2018)
Liquidus slope of eutectic Al_3Sc phase, m_β	140 ºC·wt. %$^{-1}$ in the vicinity of eutectic point	(Dorin et al., 2018)
Effective liquidus slope, m_{eff}	2.94 ºC·wt. %$^{-1}$	
Volume fraction of eutectic α-Al phase, f_α	91 vol. %	
Volume fraction of eutectic Al_3Sc phase, f_β	9 vol. %	
Composition difference at liquid/α-Al interface, ΔC_α	0.17 wt. %	(Dorin et al., 2018)
Composition difference at liquid/Al_3Sc interface, ΔC_β	35.2 wt. %	(Dorin et al., 2018)
Eutectic spacing, λ	0.3 μm	
Impurity diffusion coefficient, D	~3×10^{-9} m^2·s^{-1}	(Pearce, 2016)

[a] Γ takes a typical estimated value for a solid solution in melt (Li & Kuribayashi, 2003), considering the eutectic α-Al phase dominating the volume fraction in the eutectic dendrites.
[b] L takes the values for pure Al, for the same reasoning in note a.
[c] c_p, κ, a take the respective values for pure liquid Al, as the Al-based alloy is dilute.

5.4.2 Assessment of growth condition for the eutectic solidified by slow cooling

In the slow-cooled specimen, the proeutectic Al_3Sc phase formed prior to the eutectic. It is well-known that the proeutectic Al_3Sc is an effective grain refiner for Al alloys, and the refined grains have a globular form. However, unlike the dendritic form, the S/L interface advancing velocity can hardly be derived from the globular shape. But alternatively, the eutectic growth rate can be obtained by a scaling law that associates the growth rate and the eutectic spacing, as it is assumed that the a steady-state of eutectic growth was established under the slow cooling condition. The scaling law is written as (Trivedi & Wang, 2012)

$$V\lambda^2 = \frac{K_2}{K_1}\frac{2D}{PF} \tag{5.4}$$

where K_2 is another material property constant, involving some unknown parameters, such as the Gibbs-Thomson coefficient and the contact angle for each eutectic phase, detailed in the reference (Trivedi & Wang, 2012). Without the knowledge of the exact values of extra parameters in K_2,the author plugs other relevant constants and variables under the fast cooling condition into Eq. (5.4), and derives $K_2 = 2.22 \times 10^{-6}$ m·wt. %.

As mentioned in section 5.3.2, the volume fraction for the eutectic Al_3Sc phase in the slow-cooled eutectic structure is ~1 vol. %. With $f_\beta = 0.01$, the variations in P, F, and $(\Delta T_c + \Delta T_r)$ with p_e are plotted in figure 5.8d, 5.8e, and 5.8f, respectively. Solidified by slow cooling, the eutectic Peclet number is expected to be smaller than unity (Trivedi et al., 1987), and this will be verified shortly. As such, functions P and F approach their upper limits, 0.0184 and unity, respectively. Substituting functions P and F, and other known constants and variables into Eq. (5.4) yields $V = 4.2 \times 10^{-3}$ m·s^{-1}. Accordingly, $p_e = 0.77$ and $(\Delta T_c + \Delta T_r) = 11.1$ ºC. In addition, using Eq. (5.3), $\Delta T_k = 0.06$ ºC.

5.4.3 Non-faceting behavior of the faceted-natured Al_3Sc eutectic phase

The intermetallic compound, Al_3Sc, has long been recognized as being highly faceted in nature (Blake & Hopkins,1985; Hyde et al., 2001; Norman et al., 1998), which is also demonstrated by the cubic form of proeutectic Al_3Sc in the last and present chapters, see figure 4.3 and 5.7d. On the contrary, the eutectic Al_3Sc phase, under the same casting condition, fights against the faceted nature and exhibits non-faceted characteristics, figure 5.7f. Although the kinetic

roughening phenomenon may override a crystal's faceted nature (Glicksman, 2011), it generally demands a far-from-equilibrium condition for highly anisotropic intermetallic phases, which is not the case in the slow-cooled specimen. It is suggested that there must be another mechanism for the eutectic Al_3Sc phase to select a non-faceting behavior. The proposed mechanism is based on a so-called 'competitive growth' criterion, which has been widely applied to comparing dendritic and eutectic growth in the literature (Kurz & Fisher, 1979; Li et al., 2007; Pierantoni et al., 1992; Wang et al., 2011). In principle, the favored structure that will survive among multiple options is the one with the fastest growth rate at a given interface temperature, or equivalently, the one with the highest interface temperature at a given growth rate (Kurz & Fisher, 1979). The author translates the competitive growth criterion to the present section, that is, at a given growth rate, the regular eutectic involving non-faceted Al_3Sc has a higher interface temperature than the irregular eutectic containing faceted Al_3Sc. Expressing this criterion in terms of the interface undercooling, one has

$$(\Delta T_{c,n} + \Delta T_{r,n} + \Delta T_{k,n} + \Delta T_R)_V < (\Delta T_{c,f} + \Delta T_{r,f} + \Delta T_{k,f})_V$$

in which the subscripts before the comma, c, r, k have the same meanings as in the preceding, the subscripts after the comma, n, f denoting non-faceted and faceted growth of the eutectic Al_3Sc phase, respectively, V fixed at 4.2×10^{-3} m·s^{-1}, and the last term on the left-hand side, ΔT_R, an extra undercooling component, induced by the forced alteration of interface's roughness, see below.

First, ΔT_R is evaluated. Following Jackson's idea, the relative molar free energy of an S/L interface that maintains a certain roughness, represented by a parameter θ, is written as (Jackson, 2005):

$$\Delta G(\theta) = RT_m[\theta(1-\theta)\alpha + \theta \ln \theta + (1-\theta)\ln(1-\theta)] \tag{5.5}$$

where the parameter θ is the ratio of the number of occupied sites to the maximum number of growth sites for adding new atoms, R the gas constant, T_m the melting temperature, and α the Jackson alpha factor, expressed as $\alpha = \frac{\Delta S_f}{R}\frac{n_1}{Z}$, ΔS_f the molar entropy of fusion, n_1/Z as a whole being a geometrical factor, n_1 the number of nearest-neighbor bonds parallel to the growing crystalline plane, and Z the total number of nearest-neighbor bonds. When θ approaches zero or unity, the interface is considered smooth (faceted), whereas when θ is close to 0.5, the interface becomes rough (non-faceted). Using the face-centered cubic (FCC) structure as an analog to $L1_2$-

structured Al_3Sc, $n_1/Z = 0.5$ for the most closed packed planes {111} (Jackson, 2005). Then, given $\Delta S_f = 42.2$ J·K^{-1}·mol^{-1}, see the last chapter, an estimated α for Al_3Sc takes a value of 2.5. Substituting $\alpha = 2.5$ into Eq. (5.5) for Al_3Sc, the variation in $\Delta G(\theta)$ with θ is plotted in figure 5.9. As anticipated, Al_3Sc is predicted to have a faceted nature, since the relative free energy minima position near $\theta = 0$ and $\theta = 1$. However, the observed non-faceted characteristics for the eutectic Al_3Sc phase may indicate a roughness parameter near $\theta = 0.5$. For the ith phase, $\Delta G^i(\theta)$ deviates from the minimum, ΔG^i_{min}, when the interface roughness violates its nature, resulting in an energy cost of $[\Delta G^i(\theta) - \Delta G^i_{min}]$. This energy cost imposes an additional undercooling to the interface temperature of the ith phase, writing as $\Delta T^i_R \approx [\Delta G^i(\theta) - \Delta G^i_{min}]/\Delta S^i_f$, when the interface temperature is not too far from the equilibrium temperature. Furthermore, a growing regular eutectic is generally assumed to have an isothermal S/L interface, at least on the scale of the eutectic spacing (Li & Zhou, 2005), leading to the total undercooling for altering interfacial roughness sharing the same form as the total kinetic undercooling, cf. Eq. (5.3), namely

$$\Delta T_R = m_{eff}\left(\frac{\Delta T^\alpha_R}{m_\alpha} + \frac{\Delta T^\beta_R}{m_\beta}\right) \tag{5.6}$$

In Eq. (5.6), the α-Al phase presumably grew with a rough interface, as dictated by its non-faceted nature, then, $\Delta T^\alpha_R = [\Delta G^\alpha_{min} - \Delta G^\alpha_{min}]/\Delta S^\alpha_f = 0$. For the eutectic Al_3Sc, $[\Delta G^\beta(0.5) - \Delta G^\beta_{min}]$ gives an energy barrier of 474.6 J·mol^{-1}, see figure 5.9, and accordingly, $\Delta T^\beta_R = 11.2$ ºC. Plugging both terms into Eq. (5.6), $\Delta T_R = 0.24$ ºC is obtained.

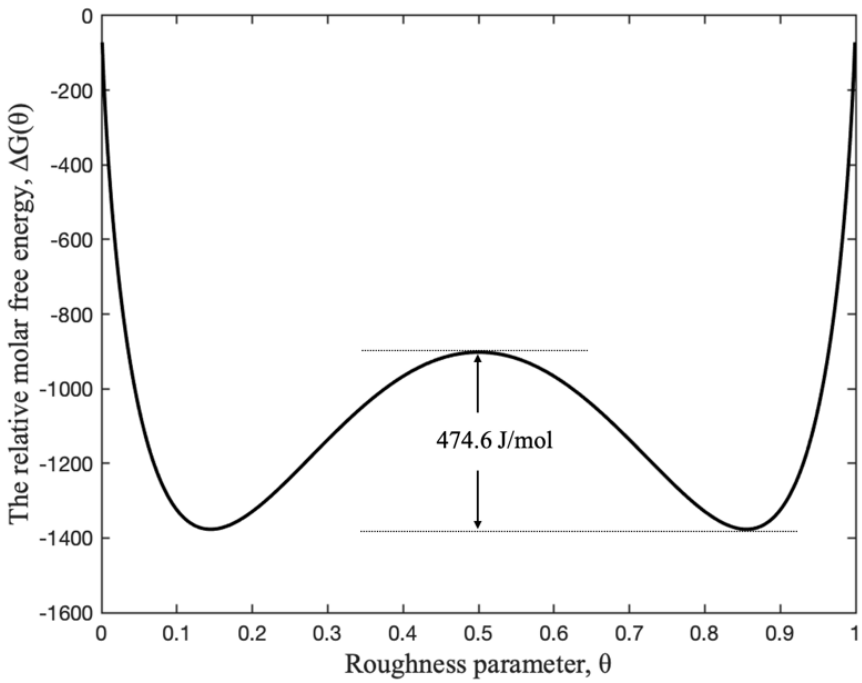

Figure 5.9 The relative molar free energy plotted against the interface roughness parameter for Al_3Sc with an Jackson alpha factor of 2.5.

Next, $\Delta T_{k,n}$ and $\Delta T_{k,f}$ are examined, to see how does the kinetic undercooling influence the eutectic Al_3Sc phase in selecting faceting/non-faceting behavior. In section 5.4.2, the total kinetic undercooling for Al-Al_3Sc eutectic growing with an isothermal rough interface has been assessed, and presented here, $\Delta T_{k,n} = 0.06$ ºC. However, if the eutectic Al_3Sc phase grew in a faceted manner, its individual kinetic undercooling may obey a square kinetics law (Trivedi et al, 1979; Wang et al., 2011), i.e., $\Delta T_{k,f}^{\beta} = \sqrt{\frac{V/V_D}{\mu_{\beta,f}}}$, where $V_D = D/a_0$, a_0 the interatomic distance, commonly 0.5 nm (Wang et al., 2011), and $\mu_{\beta,f}$ the kinetics coefficient for the square kinetics law for Al_3Sc. However, the latter parameter is not available neither in the present dissertation nor in the literature. As a compromise, the author uses an experimentally determined kinetics coefficient for another intermetallic compound $Al_{11}Sm_3$ to roughly estimate the magnitude of $\mu_{\beta,f}$, which is 6×10^{-4} ºC^{-2} (Wang et al., 2011). Accordingly, $\Delta T_{k,f}^{\beta} \approx 1.1$ ºC. The hypothetical faceted growth of eutectic Al_3Sc is likely to cause a non-isothermal S/L interface for the eutectic system, such that Eq. (5.3) does not hold for evaluating the total kinetic undercooling $\Delta T_{k,f}$ in this scenario. Instead, a weighted kinetic undercooling is tentatively considered, i.e., $\Delta T_{k,f} =$

$f_\alpha \Delta T_k^\alpha + f_\beta \Delta T_{k,f}^\beta \approx 0.014$ ºC. Apparently, both $\Delta T_{k,n}$ and $\Delta T_{k,f}$ are small relative to ΔT_R, and furthermore, $\Delta T_{k,n}$ is even larger than $\Delta T_{k,f}$. This is to say, the kinetic undercooling plays little or no role in facilitating the non-faceting behavior of eutectic Al_3Sc phase, if not hindering it.

Lastly, the comparison is made between $(\Delta T_{c,f} + \Delta T_{r,f})$ and $(\Delta T_{c,n} + \Delta T_{r,n})$. In fact, these two parentheses can be assessed under the same framework. Using Eq. (5.4) to eliminate F in Eq. (5.2), Eq. (5.2) is rewritten as

$$\Delta T_c + \Delta T_r = m_{eff}\left(\frac{K_1 VP}{2D}\lambda + \frac{K_2}{\lambda}\right) \tag{5.7}$$

At the given growth rate $V = 4.2 \times 10^{-3}$ m·s^{-1}, $(\Delta T_c + \Delta T_r)$ versus λ is plotted in figure 5.10. As stated in section 5.4.1, the regular eutectic growth is assumed to operate at the extremum condition, i.e., the undercooling minimum. Under this condition, as assessed in section 5.4.2, $(\Delta T_{c,n} + \Delta T_{r,n}) = 11.1$ ºC at $\lambda_{ex} = 1.1$ µm. On the other side, the irregular eutectic growth, in essence, is to shift the operating point along the right half curve to a new condition at a mean eutectic spacing of $\phi\lambda_{ex}$ (Kurz & Trivedi, 1991; Stefanescu, 2015). The rise in the eutectic spacing is owing to the strongly anisotropic growth and branching difficulties for the faceted phase (Kurz & Fisher, 1979). Some typical values of ϕ can be found in the Al-Si eutectic ($\phi = 3.2$) (Pierantoni et al., 1992) and the Fe-C eutectic ($\phi = 5.4$) (Stefanescu, 2015). Incidentally, ϕ is not a constant and it varies with the temperature gradient in the directional solidification (Elliott, 1988). Using Eq. (5.7) and figure 5.10, the undercooling difference $[(\Delta T_{c,f} + \Delta T_{r,f}) - (\Delta T_{c,n} + \Delta T_{r,n})]$ is evaluated at two conservative estimates of ϕ for the Al-Al_3Sc eutectic. At $\phi = 2$ and 3, the undercooling difference is 3.0 and 7.8 ºC, respectively. Both are far larger than ΔT_R. It is concluded that although the selection of non-faceted growth made the eutectic Al_3Sc phase violate the faceted nature and brought about an added undercooling, the resulting regular eutectic growth greatly reduced the coupled constitutional and curvature undercoolings compared to an otherwise irregular eutectic growth, and this undercooling reduction was more than enough to compensate for the added undercooling rise, in favor of the eutectic Al_3Sc phase growing in a non-faceted fashion.

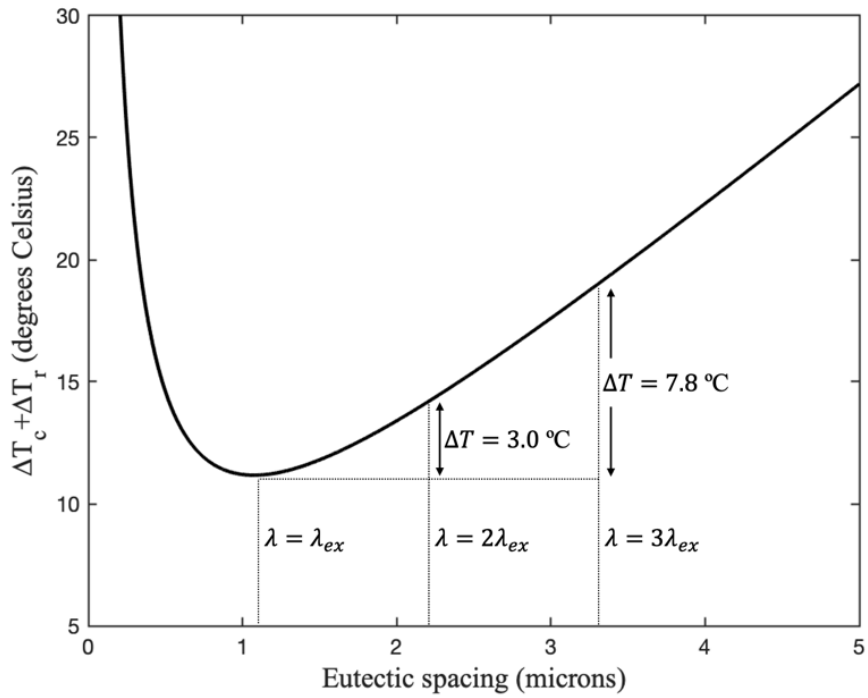

Figure 5.10 The sum of the constitutional undercooling and the curvature undercooling plotted against the eutectic spacing, at the growth rate of 4.2×10^{-3} m·s^{-1}. The extremum condition operates at $\lambda_{ex} = 1.1$ µm.

5.5 Conclusions

The present chapter reported a rod eutectic growth for the Al-Al_3Sc system with a hypereutectic composition (2 wt. % Sc) in both the air-cooled and the wedge-shaped copper mold castings. A series of microstructural transitions were found near the wedge ingot edge, which correspond to the solidification condition before, during, and after crossing the asymmetric coupled zone. Just above the coupled zone (or when $\dot{T} \leq 900$ ºC·s^{-1}), the final product is composed of the seaweed-structured proeutectic Al_3Sc and the Al-Al_3Sc rod eutectic, with the latter filling up the grain. This eutectic growth situation is not fundamentally different from that in the air-cooled specimen (with $\dot{T} \approx 1$ ºC·s^{-1}), except for a minority of eutectic Al_3Sc fibers epitaxially grown on the {100} facets of proeutectic Al_3Sc. The air-cooled specimen is also an above-the-coupled-zone case, but much closer to the equilibrium condition. Under this consideration, the Al-Al_3Sc eutectic should have a rod-like morphology in the wide range of cooling rates above the coupled zone. In the coupled zone (or when 900 ºC·s^{-1} $\leq \dot{T} \leq$ 3000 ºC·s^{-1}), the liquid Al-2 wt. % Sc alloy crystallized into an entire rod eutectic structure with an early-stage equiaxed dendritic envelope

(thus termed eutectic dendrites). Following Li and Zhou (2005), the present chapter treated the overall contour of eutectic dendrites as thermal dendrites, and assessed the internal structure using the growth model for rapidly solidified rod eutectic proposed by Trivedi and Wang (2012). An interface undercooling of 48.2 ºC was thus obtained, and serves as a guide, around which the conditions achieving an entire eutectic structure could be found. Beneath the coupled zone (or when $\dot{T} \geq 3000$ ºC·s^{-1}), the ultrafine grains were found to be comprised of a globular proeutectic α-Al core and a rod eutectic ring. Thus, the above results clarify that for the Al-2 wt. % Sc alloy at cooling rates up to ~3000 ºC·s^{-1}, α-Al and Al_3Sc could form a diffusion coupled eutectic that has a prevalent rod-like morphology.

Besides, the present chapter, based on the competitive growth criterion, justified the non-faceting behavior of the faceted-natured Al_3Sc when it composes a eutectic phase under a near-equilibrium condition, where the kinetic roughening is less persuasive in explaining the anomaly. In short, when Al_3Sc non-facets to form a regular eutectic with α-Al, the interface undercooling costs less than the situation when Al_3Sc facets to form an irregular eutectic with α-Al. Although the Al-Al_3Sc system was assigned to a specific type (cigar type), and has its unique material-related constants, this principle should be broadly valid to other similar class II eutectic systems in that the faceted-natured eutectic phase could also exhibit a non-faceted characteristic.

5.6 References

Blake, N., & Hopkins, M. A. (1985). Constitution and age hardening of Al-Sc alloys. *Journal of Materials Science, 20*(8), 2861-2867. https://doi.org/10.1007/BF00553049

Boettinger, W. J., & Coriell, S. R. (1986). MICROSTRUCTURE FORMATION IN RAPIDLY SOLIDIFIED ALLOYS. In: P. R. Sahm, H. Jones, & C. M. Adam (Eds.), *Science and Technology of the Undercooled Melt: Rapid Solidification Materials and Technologies* (pp. 81-109). Springer, Dordrecht. https://doi.org/10.1007/978-94-009-4456-5_5

Brodova, I. G., Bashlikov, D. V., & Polents, I. V. (1998). Influence of Heat Time Melt Treatment on the Structure and the Properties of Rapidly Solidified Aluminum Alloys with Transition Metals. *Materials Science Forum, 269-272*, 589-594. https://doi.org/10.4028/www.scientific.net/msf.269-272.589

Cantor, B., Kim, W. T., Bewlay, B. P., & Gillen, A. G. (1991). Microstructure — cooling rate correlations in melt-spun alloys. *Journal of Materials Science, 26*(5), 1266-1276. https://doi.org/10.1007/BF00544465

Dorin, T., Ramajayam, M., Vahid, A., & Langan, T. (2018). Aluminium scandium alloys. In: R. Lumley (Ed.), *Fundamentals of Aluminium Metallurgy: Recent Advances* (pp. 439-494). Woodhead Publishing. https://doi.org/10.1016/B978-0-08-102063-0.00012-6

Elliott, R. (1983). *Eutectic Solidification Processing: Crystalline and Glassy Alloys*. Butterworth-Heinemann, London. https://doi.org/10.1016/C2013-0-04144-8

Elliott, R. (1988). The Modification of Aluminium Silicon Casting Alloys. *Cast Metals, 1*(1), 29-33. https://doi.org/10.1080/09534962.1988.11818944

Eskin, D. G. (2018). Sc Applications in Aluminum Alloys: Overview of Russian Research in the 20th Century. In: O. Martin (Ed.), *Light Metals 2018. TMS 2018. The Minerals, Metals & Materials Series* (pp. 1565-1572). Springer, Cham. https://doi.org/10.1007/978-3-319-72284-9_204

Gale, W. F., & Totemeier, T. C. (Eds.). (2004). *Smithells Metals Reference Book* (8th ed.). Elsevier, New York.

Glicksman, M. E. (2011). *Principles of solidification: An introduction to modern casting and crystal growth concepts*. Springer, New York. https://doi.org/10.1007/978-1-4419-7344-3

Goetzinger, R., Barth, M., & Herlach, D. M. (1998). Growth of lamellar eutectic dendrites in undercooled melts. *Journal of Applied Physics, 84*(3), 1643-1649. https://doi.org/10.1063/1.368233

Hoglund, D. E., Aziz, M. J., Stiffler, S. R., Thompson, M. O., Tsao, J. Y., & Peercy, P. S. (1991). Effect of nonequilibrium interface kinetics on cellular breakdown of planar interfaces during rapid solidification of Si-Sn. *Journal of Crystal Growth, 109*(1-4), 107-112. https://doi.org/10.1016/0022-0248(91)90164-Z

Hunt, J. D., & Jackson, K. A. (1966). Binary eutectic solidification, *Transactions of the Metallurgical Society of AIME, 236*(6), 843-852.

Hürlimann, E., Trittibach, R., Bisang, U., & Bilgram, J. H. (1992). Integral parameters of xenon dendrites. *Physical Review A, 46*(10), 6579-6595. https://doi.org/10.1103/PhysRevA.46.6579

Hyde, K. B., Norman, A. F., & Prangnell, P. B. (2001). The effect of cooling rate on the morphology of primary Al3Sc intermetallic particles in Al-Sc alloys. *Acta Materialia, 49*(8), 1327-1337. https://doi.org/10.1016/S1359-6454(01)00050-7

Jackson, K. A. (2005). *Kinetic Processes: Crystal Growth, Diffusion, and Phase Transitions in Materials*. WILEY-VCH, Weinheim. http://doi.org/10.1002/3527603891

Jackson, K. A., & Hunt, J. D. (1966). Lamellar and rod eutectic growth. *Transactions of the Metallurgical Society of AIME, 236*(6), 1129-1142.

Jones, H. (1969). Observations on a structural transition in aluminium alloys hardened by rapid solidification. *Materials Science and Engineering, 5*(1), 1-18. https://doi.org/10.1016/0025-5416(69)90077-9

Kurz, W., & Fisher, D. J. (1979). Dendrite growth in eutectic alloys: The coupled zone. *International Metals Reviews, 24*(1), 177-204. https://doi.org/10.1179/imtr.1979.24.1.177

Kurz, W., & Fisher, D. (1998). *Fundamentals of Solidification* (4th rev. ed.). Trans Tech Publications, Uetikon-Zuerich.

Kurz, W., Fisher, D. J., & Trivedi, R. (2019). Progress in modelling solidification microstructures in metals and alloys: Dendrites and cells from 1700 to 2000. *International Materials Reviews, 64*(6), 311-354. https://doi.org/10.1080/09506608.2018.1537090

Kurz, W., & Trivedi, R. (1991). Eutectic growth under rapid solidification conditions. *Metallurgical Transactions A, 22*, 3051-3057. https://doi.org/10.1007/BF02650266

Li, M., & Kuribayashi, K. (2003). Nucleation-controlled microstructures and anomalous eutectic formation in undercooled Co-Sn and Ni-Si eutectic melts. *Metallurgical and Materials Transactions A, 34*(12), 2999-3008. https://doi.org/10.1007/s11661-003-0199-5

Li, J. F., Jie, W. Q., Zhao, S., & Zhou, Y. H. (2007). Structural Evidence for the Transition from Coupled to Decoupled Growth in the Solidification of Undercooled Ni-Sn Eutectic Melt. *Metallurgical and Materials Transactions A, 38*(8), 1806-1816. https://doi.org/10.1007/s11661-007-9198-2

Li, J. F., & Zhou, Y. H. (2005). Eutectic growth in bulk undercooled melts. *Acta Materialia, 53*(8), 2351-2359. https://doi.org/10.1016/j.actamat.2005.01.042

Liu, S., Lee, J. H, & Trivedi, R. (2011). Dynamic effects in the lamellar–rod eutectic transition. *Acta Materialia, 59*(8), 3102-3115. https://doi.org/10.1016/j.actamat.2011.01.050

Naumkin, O. P., Terekhova, V. T., & Savitskii, E. M. (1965). Phase equilibrium diagram and properties of aluminium-scandium alloys. *Russian Metallurgy,* (4), 128–136.

Norman, A. F., Prangnell, P. B., & McEwen, R. S. (1998). The solidification behaviour of dilute aluminium–scandium alloys. *Acta Materialia, 46*(16), 5715-5732. https://doi.org/10.1016/S1359-6454(98)00257-2

Norman, A. F., & Tsakiropoulos, P. (1991). Rapid solidification of Al-Hf alloys - solidification microstructures and decomposition of solid-solutions, *International Journal of Rapid Solidification, 6*(3-4), 185-213.

Pearce, J. V. (2016). Survey of Key Parameters of Impurities in Aluminum: Diffusion Coefficients, Solubility, and Liquidus Slopes. *International Journal of Thermophysics, 37*, 123. https://doi.org/10.1007/s10765-016-2128-z

Perepezko, J. H., & Hildal, K. (2006). Analysis of solidification microstructures during wedge-casting. *Philosophical Magazine, 86*(24), 3681-3701. https://doi.org/10.1080/14786430500404116

Pierantoni, M., Gremaud, M., Magnin, P., Stoll, D., & Kurz, W. (1992). The coupled zone of rapidly solidified Al-Si alloys in laser treatment. *Acta Metallurgica et Materialia, 40*(7), 1637-1644. https://doi.org/10.1016/0956-7151(92)90106-O

Røyset, J., & Ryum, N. (2005). Scandium in aluminium alloys. *International Materials Reviews, 50*(1), 19-44. https://doi.org/10.1179/174328005X14311

Stefanescu, D. M. (2015). *Science and engineering of casting solidification* (3rd ed.). Springer, Cham. https://doi.org/10.1007/978-3-319-15693-4

Teng, J., Liu, S., & Trivedi, R. (2008). Growth and morphology of rod eutectics. *Acta Materialia, 56*(12), 2819-2833. https://doi.org/10.1016/j.actamat.2008.02.011

Terzi, S., Taylor, J. A., Cho, Y. H., Salvo, L., Suéry, M., Boller, E., & Dahle, A. K. (2010). In situ study of nucleation and growth of the irregular α-Al/β-Al5FeSi eutectic by 3-D synchrotron X-ray microtomography. *Acta Materialia, 58*(16), 5370-5380. https://doi.org/10.1016/j.actamat.2010.06.012

Tomus, D., Qian, M., Brice, C. A., & Muddle, B. C. (2010). Electron beam processing of Al–2Sc alloy for enhanced precipitation hardening. *Scripta Materialia, 63*(2), 151-154. https://doi.org/10.1016/j.scriptamat.2010.03.039

Toropova, L. S., Eskin, D. G., Kharakterova, M. L., & Dobatkina, T. V. (1998). *Advanced aluminum alloys containing scandium: Structure and properties*. Routledge, London. https://doi.org/10.4324/9781315097541

Trivedi, R., Franke, H., & Lacmann, R. (1979). Effects of interface kinetics on the growth rate of dendrites. *Journal of Crystal Growth, 47*(3), 389-396. https://doi.org/10.1016/0022-0248(79)90204-5

Trivedi, R., Magnin, P., & Kurz, W. (1987). Theory of eutectic growth under rapid solidification conditions. *Acta Metallurgica, 35*(4), 971-980. https://doi.org/10.1016/0001-6160(87)90176-3

Trivedi, R., & Wang, N. (2012). Theory of rod eutectic growth under far-from-equilibrium conditions: Nanoscale spacing and transition to glass. *Acta Materialia, 60*(6-7), 3140-3152. https://doi.org/10.1016/j.actamat.2012.02.020

Wang, N., Kalay, Y. E., & Trivedi, R. (2011). Eutectic-to-metallic glass transition in the Al–Sm system. *Acta Materialia, 59*(17), 6604-6619. https://doi.org/10.1016/j.actamat.2011.07.015

Wei, X. X., Lin, X., Xu, W., Huang, Q. S., Ferry, M., Li, J. F., & Zhou, Y. H. (2015). Remelting-induced anomalous eutectic formation during solidification of deeply undercooled eutectic alloy melts. *Acta Materialia, 95*, 44-56. https://doi.org/10.1016/j.actamat.2015.05.014

CHAPTER 6. CONCLUSIONS AND FUTURE WORK

The dissertation is dedicated to constructing a full picture of the solidification behaviors of the proeutectic Al_3Sc phase and the Al-Al_3Sc eutectic in a hypereutectic Al-2 wt. % Sc alloy, in order to uncover mysteries of this poorly understood alloy system.

Chapter 4 is devoted to the study of the formation mechanism of the proeutectic Al_3Sc phase. It is found that at a slow cooling rate (~1 $^{o}C \cdot s^{-1}$), the faceted nature of the highly anisotropic intermetallic compound persists. As such, a cubic form bound with {100} facets is generated, which is believed to achieve the minimum of the total interface area times interface energy. At an intermediate cooling rate (~400 $^{o}C \cdot s^{-1}$), the faceted nature of Al_3Sc is overridden by kinetic roughening (non-faceted growth), due to the high driving force for the crystal growth imposed on the solid/liquid interface. As a result, the dendritic form prevails, and the forefront solid/liquid interface is in a form of a paraboloid of revolution. In a late growth stage, when the recalescence effect dominates, and the crystallization of Al_3Sc proceeds at a near-equilibrium condition, the faceted growth takes the place of non-faceted growth, and thus, the faceted macrosteps modify the otherwise wave-like side branches of the dendrite trunks. At a high cooling rate (~1000 $^{o}C \cdot s^{-1}$), the driving force for the crystallization imposed on the solid/liquid interface is further enhanced to such a degree that the anisotropy in Al_3Sc's interface energy is not strong enough to maintain a steady paraboloidal front. Consequently, a cascade of tip splitting of the solid/liquid interface constantly occurs, and the seaweed-structured Al_3Sc is formed. Specifically, in the early stage of the growth of seaweed-structured Al_3Sc, the crystallization driving force (the melt undercooling) is large enough to produce the compact seaweeds. Later on, the melt undercooling is somehow counterbalanced by the recalescence effect. The reduced melt undercooling subsequently produces the fractal seaweeds. This is the origin of the duplex-structured Al_3Sc seaweeds. In fact, the internal compact seaweed structure can be easily confused with a solid core under a low-magnification microscopic examination.

Chapter 5 focuses on the eutectic growth of Al-Al_3Sc. It is found that contrary to existing viewpoints, Al and Al_3Sc can form a diffusion coupled eutectic, and the eutectic Al_3Sc prevalently develops a non-faceted fibrous morphology under all studied cooling conditions. At a cooling rate higher than that required to generate the proeutectic seaweed-structured Al_3Sc, the hypereutectic Al-2 wt. % Sc molten alloy can transform into an entire eutectic, which has a

dendritic contour and an inner rod eutectic structure, thus termed “eutectic dendrites”. Quantitative assessments reveal that the interface undercooling needed to form the eutectic dendrites is roughly 48.2 ºC. An involved phenomenon of scientific significance is that when composing a eutectic phase at a slow cooling rate, Al_3Sc grows in a non-faceted manner, in sharp contrast to its highly faceted nature. Since in this scenario the kinetic roughening induced by a large driving force is less convincing to justify this anomaly, a novel hypothesis based on the competitive growth is put forward, and validated afterwards. Namely, the demanded interface undercooling for the Al-Al_3Sc eutectic growth is reduced, when the eutectic Al_3Sc phase selects a non-faceted morphology to form a regular eutectic with the eutectic α-Al phase, compared to when the eutectic Al_3Sc phase sticks to a faceted structure to form an irregular eutectic with the eutectic α-Al phase.

The understanding on the present topic would be further enhanced, if the following recommended future work could be done.

(1) The used investigation methods primarily rely on the ex-situ observations, which is easily accessible but could only reveal the last moment of a frozen sample. In contrast, in-situ observations may be able to provide a dynamic picture of how each form of the proeutectic Al_3Sc or the Al-Al_3Sc eutectic develops throughout the nucleation stage and the subsequent growth stage.

(2) The used solidification approaches did not allow precise measurements for some key variables, such as the interface undercooling and the growth rate of the advancing front. However, constrained growth methods, such as Bridgman solidification approach, could make accurate control/measurements of some key variables possible.

(3) Since the studied cooling rates are discrete, other possible morphologies of the proeutectic Al_3Sc may still remain uncovered. In addition, the transitional condition of one form to the other is unclear yet. For instance, it needs further investigations that at what cooling rate, faceted growth of single-phase Al_3Sc would transition to non-faceted growth; likewise, at what cooling rate, dendritic growth of single-phase Al_3Sc would transition to seaweed growth.

APPENDIX

This Appendix addresses the estimation of the cooling rate of the intermediate cooling method used in section 4.2. Assuming relatively large dimensions and excellent thermal conductivity for the copper plate, the temperature of copper plate did not change much during the solidification of 10 g alloy melt. In this scenario, the heat flow is likely limited by melt-plate thermal resistance (Biloni & Boettinger, 1996). Heat flux, q, is expressed as

$$q = h_0(T - T_0) \tag{A.1}$$

where h_0 is the heat transfer coefficient, roughly 4×10^3 W·m^{-2}·K^{-1} for liquid metal in contact with a polished metal surface (Biloni & Boettinger, 1996), and T and T_0 are the melt temperature and the plate temperature, respectively. The latter is assumed to constantly be room temperature, 298 K. Besides, q, before nucleation, can be interpreted as the reduction in the internal energy of the specimen per unit time per unit area of the surface that effectively dissipates the heat, i.e.,

$$q = \frac{N c_{p,m} \delta T}{A \delta t} \tag{A.2}$$

where N is mole number of specimen, N=0.37 moles, $c_{p,m}$ molar specific heat of the melt, for molten Al, $c_{p,m,Al(l)}$=29.3 J·mol^{-1}·K^{-1} (Gale, 2004), δT the decrement in melt temperature, A the area of the surface that effectively dissipates the heat, approximately equal to 1.3×10^{-3} m^2, and δt the time elapsed. When δt approaches zero, $\delta T / \delta t$ represents the cooling rate. Combining Eqs. (A.1) and (A.2), the cooling rate is expressed as

$$\dot{T} = \lim_{\delta t \to 0} \delta T / \delta t = \frac{h(T - T_0)A}{N c_{p,m}} \tag{A.3}$$

Plugging T=1283 K for the moment of pouring into Eq. (A.3), $\dot{T}$=470 K·s^{-1}; plugging T=1050 K for the liquidus temperature about to be reached into Eq. (A.3), $\dot{T}$=360 K·s^{-1}. Thus, the cooling rate for copper plate cooling is of the order of 400 K·s^{-1}.

References

Biloni, H., & Boettinger, W. J. (1996). Chapter 8 – Solidification. In: R.W. Cahn & P. Haasen (Eds.), *Physical Metallurgy* (4th ed., pp. 669-842). North Holland. https://doi.org/10.1016/B978-044489875-3/50013-2

Gale, W. F., & Totemeier, T. C. (Eds.). (2004). *Smithells Metals Reference Book* (8th ed.). Elsevier, New York.